

# Solution-Processable Zinc Oxide for Printed Photovoltaics: Progress, Challenges, and Prospect

Yunfei Han, Jingbo Guo, Qun Luo,\* and Chang-Qi Ma

Zinc oxide (ZnO) is a promising candidate as the electron-transporting layer of roll-to-roll printed organic and perovskite solar cells (OSCs and PVSCs) because it is low cost, nontoxic, earth-abundant, and has multiple solution-processable routes comparable. It has been widely used in both OSCs and PVSCs for many years. With the long-time development of the ZnO buffer layer, various synthesis, fabrication, and modification approaches have been developed. Meanwhile, several issues including light-soaking issues, defects issues, and agglomeration issues have emerged and have been solved. In this review, the synthesis approaches of solution-processed zinc oxide, the application in the OSCs and the PVSCs, and the typical challenges of the solution-processed ZnO for use in the OSCs and PVSCs have been summarized. Finally, an outlook on the development of solution-processed ZnO for the upscaling of OSCs and PVSCs is given.

## 1. Introduction

Energy crisis and environmental pollution are two major global problems in the 21st century. Fossil fuel energy consumption caused CO<sub>2</sub> emissions and environmental pollution. A challenge is to find green and renewable energy to reduce the extraction and combustion of fossil fuels. Photovoltaic electricity generation is the most promising renewable energy to solve the energy crisis. Solar cells can meet the rising energy demand by harvesting electrical energy from unlimited solar energy.

Conventional silicon solar cells are widely used because of their high efficiency and high reliability. However, the efficiency of silicon solar cells is hard to be improved. In addition, the fragility and high weight of the silicon solar cells limited their application in wearable electronics, etc. Compared to conventional

Y. Han, J. Guo, Q. Luo, C.-Q. Ma  
I-Lab & Printable Electronic Research Center, Suzhou Institute of  
Nano-Tech and Nano-Bionics  
Chinese Academy of Sciences  
215123, China  
E-mail: qluo2011@sinano.ac.cn

 The ORCID identification number(s) for the author(s) of this article can be found under <https://doi.org/10.1002/aesr.202200179>.

© 2023 The Authors. Advanced Energy and Sustainability Research published by Wiley-VCH GmbH. This is an open access article under the terms of the Creative Commons Attribution License, which permits use, distribution and reproduction in any medium, provided the original work is properly cited.

DOI: 10.1002/aesr.202200179

silicon solar cells, organic and organic–inorganic hybrid perovskite solar cells (OSCs and PVSCs) have the advantages of lightweight, flexibility, low cost, and roll-to-roll printing compatibility. In recent years, both the OSCs and PVSCs achieved great development; efficiency above 18%<sup>[1–3]</sup> and 25%<sup>[4]</sup> has been widely achieved.

The OSCs and PVSCs have similar sandwich device structures, including an anode, cathode, and photoactive layer inserted between the anode and cathode. Besides, electrode buffer layers were used to modify the anode and cathode. The electrode buffer layers for OSCs and PVSCs include organic and inorganic materials. Because the OSCs and PVSCs can be fabricated

through solution-processable methods. Thus, the solution-processed buffer layer is urgently needed.

## 2. Fundamentals ZnO as a Semiconductor

### 2.1. Crystal Structure/Band Structure

Zinc oxide (ZnO) is a promising candidate as the buffer layer for roll-to-roll printed OSCs and PVSCs because it is low cost, nontoxic, earth-abundant, and has multiple solution-processable routes comparable. ZnO has three kinds of crystal structures: 1) cubic rock salt, 2) cubic zinc blende, and 3) hexagonal wurtzite structure. The three crystal structures are shown in **Figure 1**, and the shaded gray and black spheres represent zinc and oxygen atoms, respectively. Among them, the wurtzite structure is the most common and stable structure at ambient conditions. The cubic zinc blende structure is stabilized by growing ZnO on substrates with a cubic lattice structure. The zinc and oxide centers are tetrahedral in both the zinc blended and wurtzite structures. The rocksalt structure is only observed at higher pressures at about 10 GPa. As the most stable structure, the hexagonal ZnO has a point group 6 mm or C<sub>6v</sub>, and the space group is P6<sub>3</sub>mc or C<sub>6v</sub>4. The lattice constants are  $a = 3.25 \text{ \AA}$  and  $c = 5.2 \text{ \AA}$ ; their ratio  $c/a$  of 1.6 is lost to the ideal value of the hexagonal cell (1.633).

### 2.2. Intrinsic Defects

These various defects are the origin of the photoluminescence of ZnO. The defect-related photoluminescence of ZnO includes blue, green, yellow, and red luminescence. According to

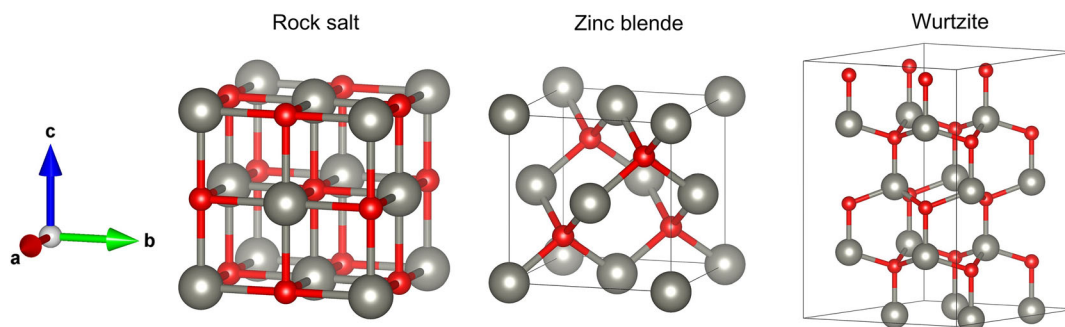


**Figure 1.** Crystal structure of ZnO: i) rock salt, ii) zinc blende, and iii) wurtzite.

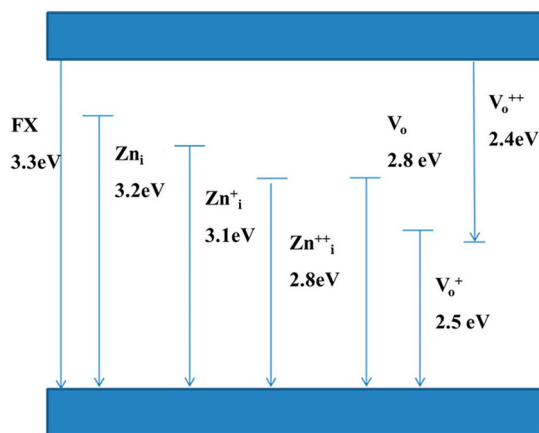


**Figure 2.** Possible optical transitions and their energies in ZnO nanostructures, where FX—free excitons,  $Zn_i$ —zinc interstitials,  $Zn^+_i$ —ionized zinc interstitials,  $V_o$ —oxygen vacancies, and  $V^{+}_o$ —ionized oxygen vacancies. Reproduced with permission.<sup>[5]</sup> Copyright 2020, CAS.

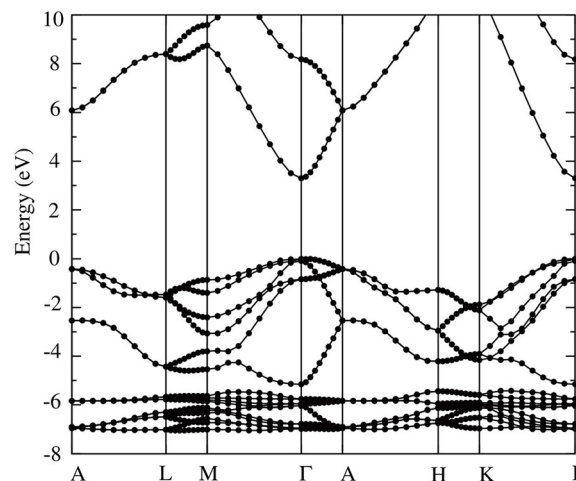


**Figure 3.** Band structure of ZnO. Reproduced with permission.<sup>[201]</sup> Copyright 2009, IOP.

Janotti et al.,<sup>[5]</sup> ZnO has several emission peaks centered at the following positions (**Figure 2**): 3.3–3.4 eV from free exciton emission, 3.24–3.27 eV from donor bound excitons/or defect, 3.1–3.22 from Zn interstitials, 3.03 eV from zinc vacancies, 2.76–2.95 eV from ionized Zn interstitials/oxygen vacancies, 2.45–2.6 eV from singly ionized O vacancy, and 2.29–2.37 eV from doubly ionized O vacancies.<sup>[5]</sup>

### 2.3. Energy Level and Conduction

ZnO is one kind of n-type direct wide semiconductor with a bandgap of 3.3 eV and electron mobility of about  $10^{-4}$ – $10^{-3}$   $\text{scm}^{-2}$ . The electronic property of the n-type semiconductor of ZnO is traditionally ascribed to the intrinsic defects of oxygen vacancy. ZnO has a large exciton binding energy of 60 meV, which indicates efficient excitonic emission in ZnO can persist at room temperature and higher temperatures. The large exciton binding energy makes ZnO a promising material for optical devices based on excitonic effects. **Figure 3** shows the calculated band structure of ZnO. The energy of the valence-band maximum (VBM) was set as zero.

## 3. The Solution-Processable Fabrication Methods of ZnO Films

The fabrication methods of the ZnO buffer layers include atomic layer deposition,<sup>[6]</sup> chemical vapor deposition, pulsed laser deposition, RF magnetron sputter,<sup>[7,8]</sup> sol-gel, solution-processed nanoparticles route, and other solution-processable approaches. This part will focus on the fundamental and synthesis method of ZnO films through solution-processable routes.

### 3.1. Sol-Gel Method

For the solution-processable route, the most widely used method to fabricate the ZnO buffer layer is the sol-gel route. In this process, the ZnO film is obtained through spin coating the zinc acetate dihydrate precursor on the substrates and followed by thermal annealing. During thermal annealing, the precursor solution of zinc salts will hydrolyze and transform into ZnO. The sol-gel ZnO layer was first used as the electron-transporting layer (ETL) in OSCs by White.<sup>[9]</sup> **Figure 4a** shows the mechanical of the sol-gel transformation process from precursor to ZnO crystals. Zinc acetate that dissolved in 2-methoxy ethanol was

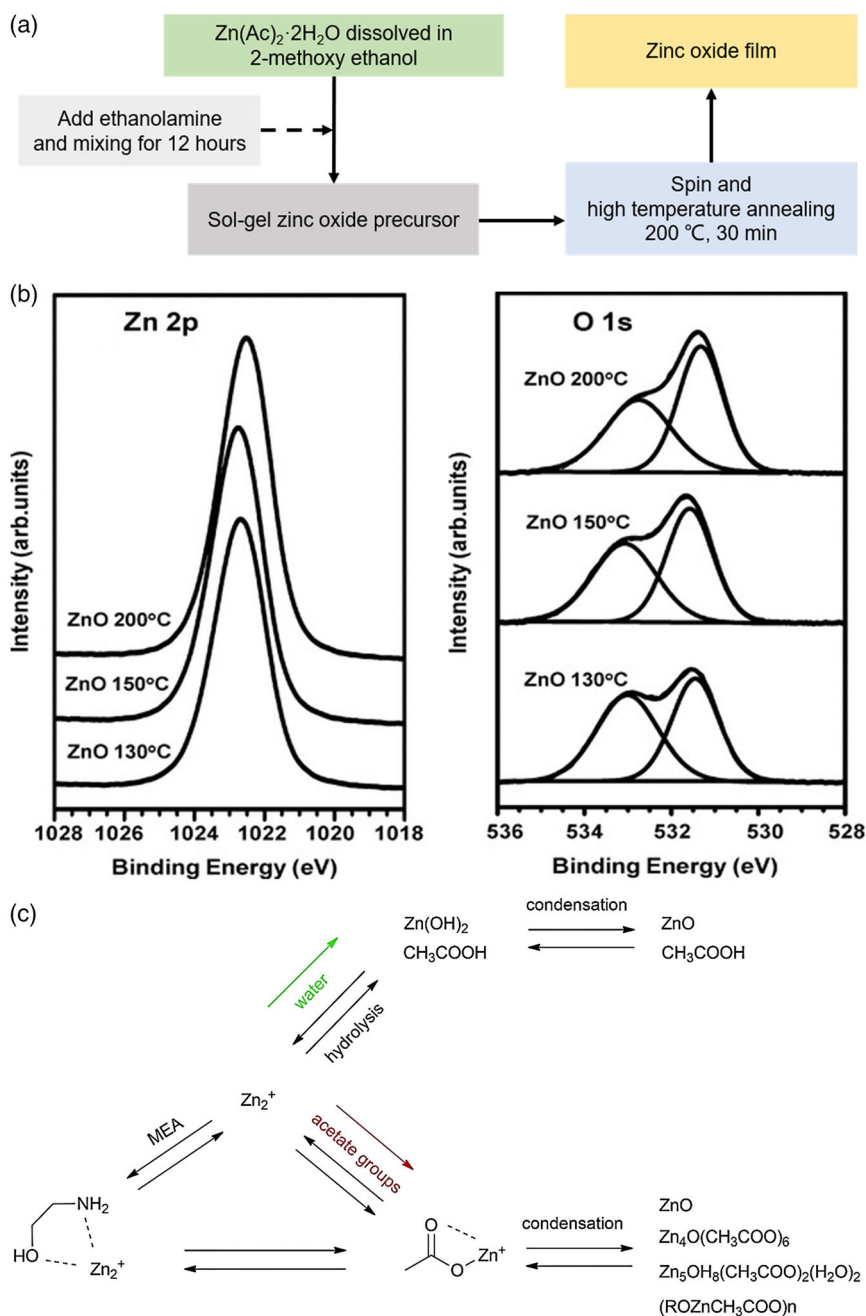


**Figure 4.** a) Schematic representation of the chemical equilibria for the ZnO sol-gel process. b) XPS spectra of the core level of Zn<sub>2p</sub> and O<sub>1s</sub> for the sol-gel ZnO films were annealed at different temperatures. Reproduced with permission.<sup>[11]</sup> Copyright 2011, Wiley-VCH GmbH. c) The influence of H<sub>2</sub>O on the hydrolysis process. Reproduced with permission.<sup>[12]</sup> Copyright 2011, IOP.

usually used as the precursor solution, and ethanolamine was usually utilized as the sol stabilizer. The solution was stirred at a low temperature to form a stable sol. But this route always requires high-temperature annealing at around 350 °C to convert ZnAc precursor to ZnO, and remove the residual organic compounds.<sup>[10]</sup> Later, Heeger et al.<sup>[11]</sup> investigated the influence of annealing temperature on the device performance and found ZnO films could be obtained at a relatively low annealing

temperature (<200 °C). But their result also indicated reducing the temperature to 130 or 150 °C, the ZnO precursor was not fully converted to ZnO films, and consequently, the ZnO films have low crystal quality. Figure 4b shows the X-ray photoelectron spectroscopy (XPS) spectra of Zn<sub>2p</sub> and O<sub>1s</sub> core levels of the sol-gel ZnO films obtained from annealing at different temperatures. The typical XPS spectra of Zn<sub>2p</sub> contained Zn 2p<sub>3/2</sub> peak at 1022.7 eV in the low temperature-annealed ZnO films.

Increasing the annealing temperature led to the peak shift toward lower binding energy due to more Zn atoms being bonded to O atoms. The  $O_{1s}$  peak contained two peaks at 531.4 and 533.0 eV, which correspond to oxygen atoms in lattice and oxygen-deficient. Increasing the annealing temperature led to a decrease in the relative ratio of oxygen defects. For the sol-gel-based ZnO films, the conversion from precursor to ZnO is highly sensitive to water content. As shown in Figure 4c, the lower  $H_2O/[Zn^{2+}]$  ratio may yield the formation of relatively complicated reaction precursors, like Zn-oxo-acetate or Zn-hydro-acetate species.<sup>[12]</sup>

The conversion temperature from the amine-containing precursor to ZnO films in the traditional sol-gel ZnO route is above 120 °C, which usually is incompatible with the substrate of flexible OSCs. Hence, Zhou et al. developed an amine-free recipe route consisting of zinc acetate dihydrate dissolved in methanol to prepare ZnO films. The conversion temperature is reduced to 90 °C due to the simpler precursor complex in this amine-free recipe. The flexible OSCs with the low-temperature ZnO ETL based on PET/ITO and PET/AgNWs electrodes achieved a power conversion efficiency (PCE) of 16.71% and 16.19%, respectively.<sup>[13]</sup>

Recently, Hou et al.<sup>[14]</sup> found the main precursor took an important role in the films-quality of slot-die-coated ZnO films. Three different kinds of amine precursors, ethanolamine (EA), n-propylamine (PA), and triethylamine (TEA), were used in the preparation of ZnO ETLs. The results showed the precursor significantly influenced the solution state, the fluidics, and the proportion of polar facets of the ZnO films. Among the three precursors, the PA-processed precursor solution is favored for the formation of uniform and smooth films. With these ZnO films, the flexible OSCs of 1 cm<sup>2</sup> area gave an outstanding PCE of 16.71%.

### 3.2. Nanoinks

Another kind of ZnO film widely used in OSCs is fabricated through a colloidal route, which means the ZnO nanoparticles were first synthesized and dispersed as inks, and finally deposited on the substrates to form films. Typically,  $ZnOAc_2$  and KOH were used as the raw materials to synthesize the ZnO nanoparticles for use in OSCs and PVSCs (as shown in Figure 5a–c). After 2 h of reaction, the ZnO precipitates could be collected after several times centrifugation. This synthesis route was first developed by Anderson et al.,<sup>[15]</sup> and modified by several groups later. Meulenkaamp et al. used LiOH to replace KOH as base.<sup>[16]</sup> Pacholski et al. found the shape of the ZnO particles was highly sensitive to the concentration of precursor. With a zinc precursor concentration below 0.01 M, the particles were quasispherical, with a zinc precursor concentration higher than 0.1 M, the particles were nanorods.<sup>[17]</sup> These ZnO nanoparticles synthesized through the above methods exhibited a similar size of about 5–8 nm, so can be well dispersed in various solvents, such as acetone, ethanol, and methanol, and kept relatively stable for a long time. The colloidal-based ZnO nanoparticle has been widely used as ETLs in the OSCs with an inverted structure.<sup>[18]</sup> In addition, due to the low-temperature-processable, these ZnO nanoinks have been already used in the roll-to-roll printed OSCs by Krebs et al.<sup>[19]</sup>

Qian et al. synthesized the ZnO nanoparticles using tetramethylammonium hydroxide (TMAH) and  $ZnOAc_2$  as the raw materials (as shown in Figure 5d–f). In this case, TMAH and  $ZnOAc_2$  were dissolved in DMSO and then reacted at room temperature for around 1 h in the air. The size of the obtained ZnO nanoparticles was around 3 nm with excellent monodispersity in ethanol solvent.<sup>[20,21]</sup> The size of the nanoparticles was dependent on the synthesis temperature and aging time. With increasing synthesis temperature from 18 to 90 °C, the diameter of ZnO nanoparticles increased from 3.2 to 6.0 nm. As the aging time gradually increased to 60 min, the size increased from about 3.6 to 6.0 nm.<sup>[22]</sup> But these kinds of ZnO nanoparticles were always used in the organic light-emitting diodes,<sup>[21,23]</sup> while rarely work reported its usage in organic photovoltaics.

Wang et al. prepared the ZnO nanoparticles by heating the zinc acetylacetonate in n-butanol through microwave heating route, and diethanolamine and water were used as additives (Figure 5g–i).<sup>[24]</sup> Using this method, the average diameter of ZnO nanoparticles could be regulated from  $\approx 120$  to 20 nm through regulating the concentration of ethylenediamine (EDA), and correspondingly the bandgap regulated from 3.31 to 3.55 eV. This work found the ZnO nanoparticles with higher bandgap could increase the open voltage ( $V_{OC}$ ) of the bilayer polymer solar cells but gave an identical  $V_{OC}$  in the bulk-heterojunction OSCs.

In addition, ZnO nanoparticles were synthesized in 2-aminoethanol as well (Figure 5j–p). In this synthesis system, zinc acetate was used as the raw material, and 2-aminoethanol acted both as a stabilizer and a solvent. Typically, zinc acetate was added to 2-aminoethanol and heated up to 160 °C in an oil bath, stirred and refluxed for 1 h under isothermal treatment. The obtained solution was centrifuged to remove the precipitates, and the supernatant could be dispersed in 2-aminoethanol, and deposited on the top of the ITO substrate without the need of any thermal annealing for use in OSCs.<sup>[25]</sup>

The ZnO film was also fabricated from the  $[Zn(NH_3)_x](OH)_2$  precursor solution, which was obtained through the reaction of  $Zn(NO_3)_2$  with NaOH, and followed by dissolving the  $Zn(OH)_2$  agglomerate in  $NH_3(aq)$ .<sup>[26]</sup> Similarly, the ZnO nanoinks could be prepared by simply dissolving ZnO powers in ammonia to form  $Zn(NH_3)_4^{2+}$  solution through ultrasonic and refrigerator. Using such ZnO nanoink, the ZnO films could be fabricated through a solution-processable deposition route and annealing at 150 °C for several minutes.<sup>[27]</sup> The commercialized ZnO powers could be mixed with solvents, and some surfactants, such as silane<sup>[28]</sup> and methoxyethoxyacetic acid (MEA),<sup>[29,30]</sup> and then treated by high-energy ball milling to form ZnO nanoinks as well. After grinding, the initially nonuniform particles with a size of about >250 nm would form stable ZnO nano inks with a size of  $\approx 25$  nm.<sup>[31]</sup> This method is simple, convenient, cheap, facile, and environmentally friendly. However, the device gave relatively low-performance using such kind of ZnO ETL, which might be because the commercialized ZnO powers have large size. So, this method was not frequently used in the field of organic photovoltaics.

For the synthesis of ZnO nanoparticles, the size and morphology were influenced by several factors. Searson et al.<sup>[32]</sup> synthesized ZnO nanoparticles using three different

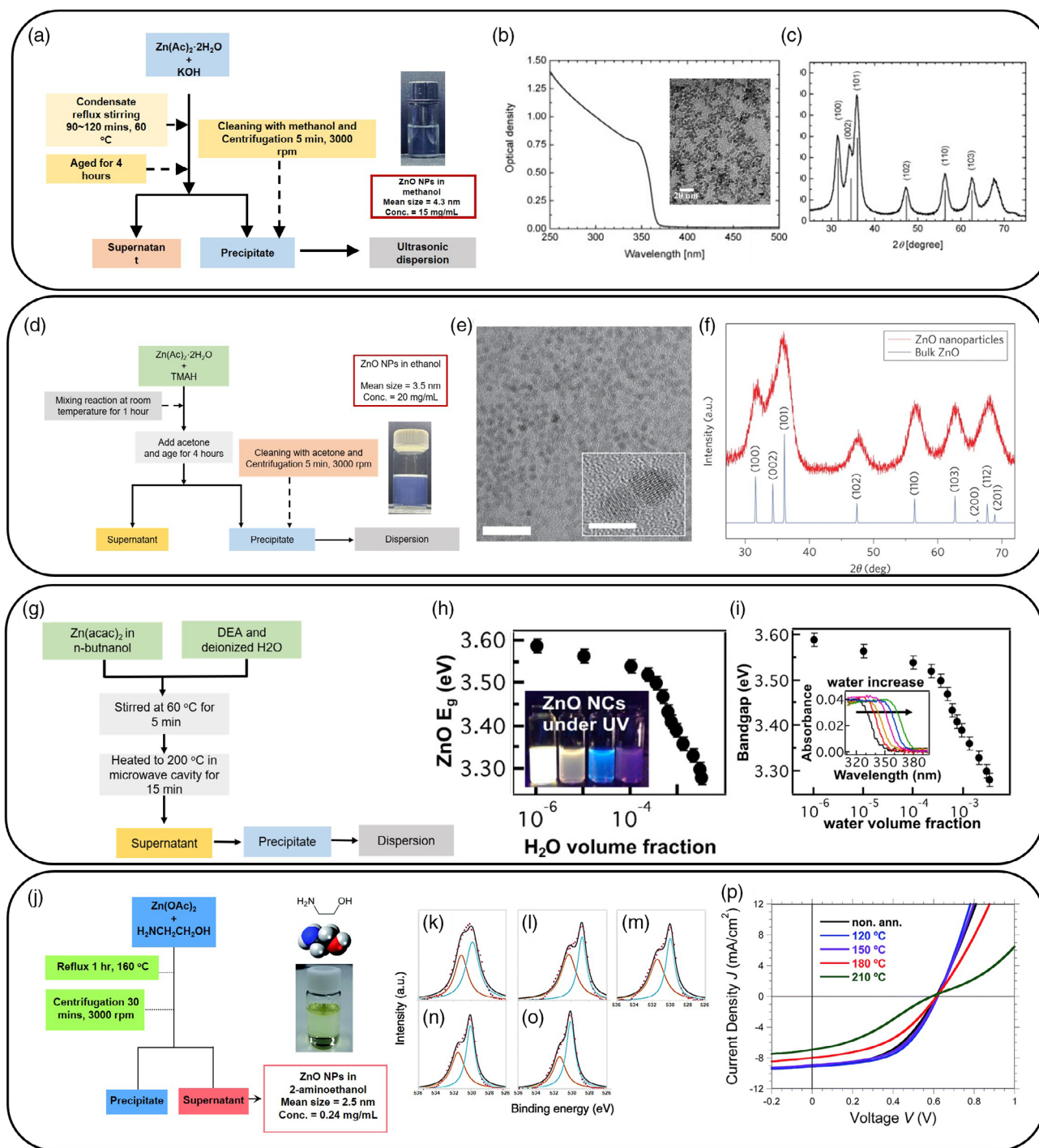


**Figure 5.** The schematic diagram of the synthesis process of ZnO nanoparticles inks using different routes. a) sol-gel reaction route with Zn(Ac)<sub>2</sub> and KOH as the precursors. b) UV-vis absorbance spectra of the ZnO nanoparticle inks, c) XRD patterns of the ZnO nanoparticles. Reproduced with permission.<sup>[16]</sup> Copyright 1998, ACS. d) Synthetic route of ZnO nanoparticles with Zn(Ac)<sub>2</sub> and TMAH as the raw materials. e) Transmission electron microscope (TEM) images and f) XRD patterns of the obtained ZnO nanoparticles. Reproduced with permission.<sup>[21]</sup> Copyright 2011, Springer Nature. g) ZnO nanoparticles were synthesized with Zn(acac)<sub>2</sub> and DEA as raw materials. h, i) Bandgap of the ZnO nanoparticles synthesized from different environments. Reproduced with permission.<sup>[24]</sup> Copyright 2014, ACS. Reproduced with permission. Copyright 2011, Springer Nature. j) Synthesis route of ZnO nanoparticles with Zn(OAc)<sub>2</sub> as raw materials in 2-aminoethanol. k-o) XPS spectra of O<sub>1s</sub> of ZnO from different temperatures, p) J-V characteristics of the OSCs with ZnO ETL annealed at different temperatures. Reproduced with permission.<sup>[25]</sup> Copyright 2014, RSC.

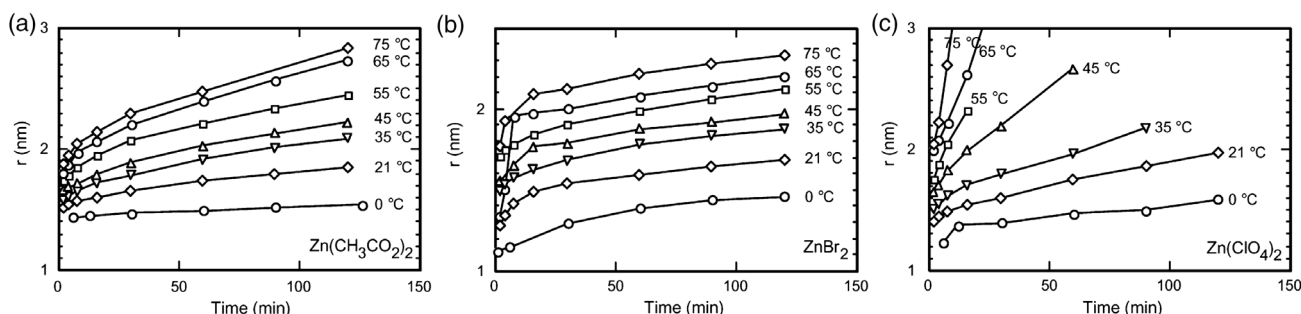


**Figure 6.** Time-dependent ZnO size with a)  $\text{Zn}(\text{CH}_3\text{CO}_2)_2$ , b)  $\text{ZnBr}_2$ , and c)  $\text{Zn}(\text{ClO}_4)_2$  as the zinc salts. Reproduced with permission.<sup>[32]</sup> Copyright 2003, ACS.

zinc salts, i.e., zinc acetate dihydrate, zinc bromide, and zinc perchlorate hexahydrate. For the synthesis with  $\text{Zn}(\text{CH}_3\text{CO}_2)_2$  (Figure 6a) and  $\text{ZnBr}_2$  precursors (Figure 6b), the nucleation and growth rate are fast and followed by diffusion-limited coarsening. For synthesis from  $\text{Zn}(\text{ClO}_4)_2$  (Figure 6c), diffusion-limited coarsening was observed within a shorter time whereas the particle size increased more rapidly during longer times. The time-dependent size of the ZnO NPs in these three cases proved such a process. In addition, Pelicano et al.<sup>[33]</sup> demonstrated that nanomorphology of the ZnO films was controlled by the pH value in the route of forming ZnO films through oxidation of Zn thin films (as shown in Figure 7).

Using these ZnO precursors or the nanoparticles inks, the ZnO films can be fabricated through various solution-processable methods, including spin coating, spray coating,<sup>[34]</sup> doctor-blade coating,<sup>[35]</sup> gravure printing,<sup>[36]</sup> and slot-die printing.<sup>[37]</sup>

## 4. The application of Solution-Processable ZnO in Printable Photovoltaic Cells

### 4.1. The Application of Solution-Processable ZnO in OSCs as the Electron Transporting Layer

ZnO has already been used in OSCs as the ETL since 1999 and in the PVSCs since 2003. From then on, a variety of research was carried out to solve the problem of ZnO in thin-film photovoltaics and improve the device performance, including developing new fabrication methods, the device optimization of OSCs and PVSCs with ZnO buffer layers, investigation of the influence of physics-chemical properties of ZnO buffer layer on the device performance, solving the main problems of ZnO buffer layer for use in OSCs and PVSCs, and the improving the photoelectrical properties through various methods.

As the ZnO colloidal-based films could be fabricated through spin coating or printing routes without the need for

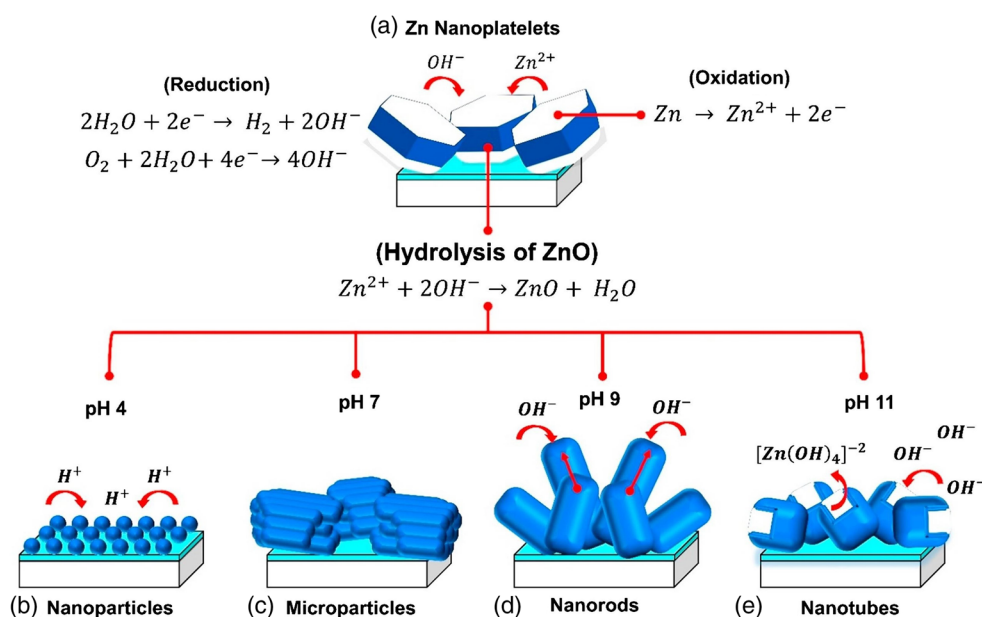


**Figure 7.** Growth mechanism of ZnO structures via pH-controlled  $\text{H}_2\text{O}$  oxidation from a) ZnO nanoplatelets to b) ZnO nanoparticles, c) microparticles, d) columnar nanorods, and e) nanotubes. Reproduced with permission.<sup>[33]</sup> Copyright 2019, Elsevier.

high-temperature annealing, this ZnO layer could be deposited on the top of the active layer as ETL in the conventional structure OSCs or as an intermediate layer of the tandem solar cells, or as ETL in the inverted OSCs to modify the bottom electrode (as shown in **Figure 8**).

The first work using ZnO in the bulk heterojunction OSCs was reported by White et al.<sup>[9]</sup> ZnO buffer layer was deposited on the top of ITO electrode through sol-gel route with precursor solution that contains zinc acetate, 2-methoxy ethanol, and ethanolamine, and followed by annealing the films at 300 °C for 5 min. On top of the ZnO ETL, the P3HT:PCBM blend films were fabricated through spin coating. Finally, the inverted OSCs with the structure of ITO/sol-gel ZnO/P3HT:PCBM/Al were fabricated. **Figure 9a,b** shows the atomic force microscope (AFM) images of the sol-gel ZnO films and the energy level of the inverted OSCs. The device showed the highest performance of 2.97%. More importantly, Jen et al. found the device with an inverted structure showed a great advantage in long-term stability. As shown in **Figure 10**, for the P3HT:PCBM device with a conventional structure, performance declined to less than 10% of the initial value within 5 days. However, the inverted solar cells with ZnO ETL kept 80% of the initial efficiency after 40 days of storage in the air.<sup>[18]</sup>

The ZnO layer on the top of the active layer could serve as the space optical layer to regulate the space light distribution,

enhance light intensity inside the active layer, and finally improve the device performance.<sup>[38]</sup> But the optical space effect is collaboratively influenced by the photonic parameters and the thickness of all the functional layers. Therefore, Vervich et al.<sup>[39]</sup> simulated the influence of the ZnO optical space layer on the photocurrent of the solar cells. With a 45 nm-thick active layer, the addition of a 40 nm-thick ZnO layer would cause a reduced  $J_{SC}$ . But in the case of an active layer with a thickness of 5–175 nm, the introduction of ZnO always has increased the  $J_{SC}$  whatever the thickness of the active layer.

In tandem or multijunction OSCs, the subcells should be collected together through an intermediate electrode. Such an intermediate electrode needs to collect electrons and holes from the different subcells separately, as well as form ohmic contact with the subcells. A conventional intermediate electrode in tandem OSCs is composed of ZnO/TiO<sub>2</sub> and PEDOT:PSS.<sup>[40–42]</sup> As both the ZnO and PEDOT:PSS are deposited on the top of the organic photoactive layer, the ZnO layer used in the tandem cells is always synthesized through the nanoparticles route rather than the sol-gel route. Because ZnO could be destroyed by the acidic PEDOT:PSS, thereby neutralized PEDOT:PSS (n-PEDOT:PSS) was used in the conventional structure tandem solar cells in which PEDOT:PSS is deposited on the top of ZnO as the interconnection layer. Usually, the intermediate layer combines a

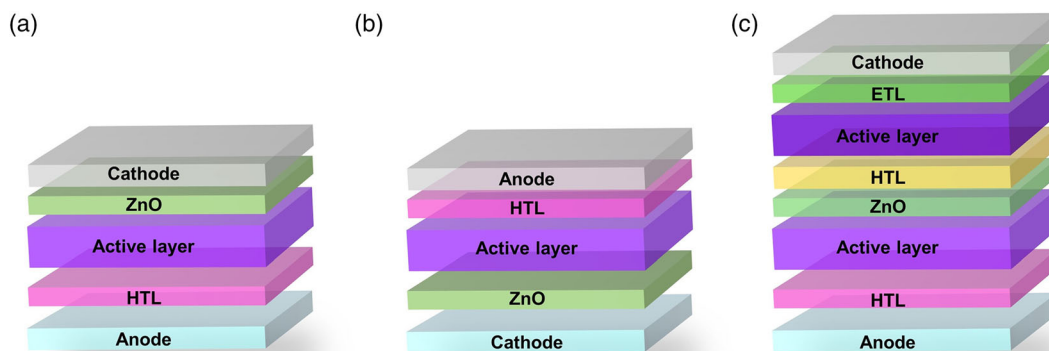


**Figure 8.** The device structure of ZnO in the heterojunction OSCs: a) conventional structure OSCs, b) inverted OSCs, and c) tandem OSCs.

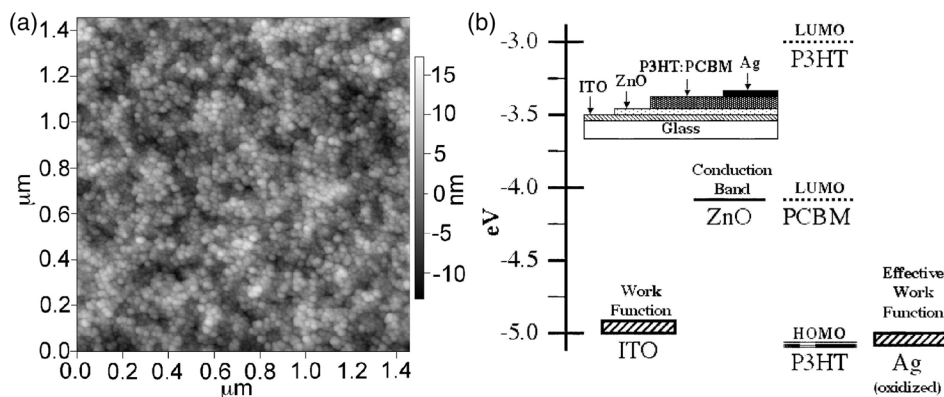


**Figure 9.** a) AFM images of the ZnO surface fabricate from the sol-gel method, b) estimated band diagram of the inverted OSCs. Reproduced with permission.<sup>[54]</sup> Copyright 2006, IOP.

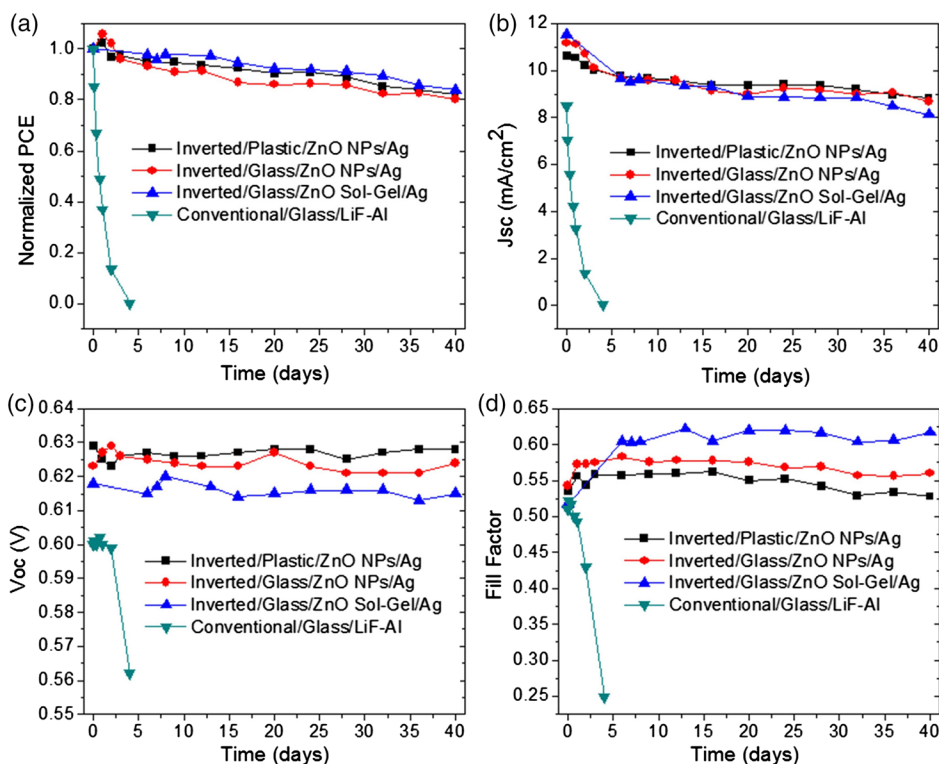


**Figure 10.** Device performance of the unencapsulated conventional and inverted solar cells stored for 40 days in air ambient conditions: a) normalized PCE, b) short-circuit density, c) open-circuit voltage, and d) fill factor. Reproduced with permission.<sup>[18]</sup> Copyright 2008, IOP.

30 nm-thick ZnO layer and a 20 nm-thick n-PEDOT:PSS layer.<sup>[43]</sup> Similar to the light-soaking effect of ZnO-based inverted OSCs, the tandem OSCs with ZnO/PEDOT:PSS intermediate layer showed a light-soaking phenomenon, suggesting the tandem cells needed to be irradiated under UV light for several minutes.<sup>[44]</sup> Two solution methods include using AZO as the substitution of ZnO or inserting an extra Ag NWs thin film between ZnO and PEDOT:PSS.<sup>[45]</sup> Due to the high conductivity of ZnO:Al, the thickness of the intermediate layer could be as high as 160 nm.<sup>[46]</sup> Because PEDOT:PSS has strong optical absorption, the insertion of a thick PEDOT:PSS layer in the tandem solar cells would reduce the short-circuit current. Therefore, Chou et al. developed the full metal oxide-involved intermediate layer that contains MoO<sub>3</sub>, Al, and ZnO.<sup>[47]</sup> Compared to PEDOT:PSS, the absorption of this intermediate layer was nearly negligible throughout the visible to NIR spectra range. In 2011, a PCE of 5.1% was achieved with P3HT:PCBM and PSBTBT:PCBM as the bottom and top cells, respectively.<sup>[48]</sup> In that work, a 3 nm-Al layer was used as the recombination center for the carrier.

As for use in the flexible OSCs, all the functional layers should be fabricated at low temperatures, therefore the ZnO buffer layers used for the flexible cells are mostly fabricated through the ZnO colloidal route rather than the sol-gel route.<sup>[49,50]</sup> In recent years, metal grids<sup>[51,52]</sup> and metal nanowire<sup>[53]</sup> were proven as the potential transparent electrodes for large-area flexible solar cells. With these flexible electrodes, ZnO NPs were deposited on the top of the high-conductive PEDOT:PSS layer in the inverted solar cells.<sup>[51,52]</sup>

Table 1, 2, and 3 list the efficiency development of the sol-gel ZnO, ZnO NP-based single and tandem OSCs. Figure 11 and 12 summarize the efficient development of ZnO-involved single-junction and tandem OSCs. Figure 13 shows the summary of the annual highest performance of the single junction and tandem OSCs. In 2006, White et al. first brought in sol-gel ZnO as the ETL in the inverted OSCs based on a blend of poly(3-hexylthiophene) and a fullerene, and a PCE of 2.91% was achieved.<sup>[54]</sup> In the next year, Gilot et al. fabricated multiple-junction OSCs through spin coating neutral pH PEDOT onto the ZnO NPs; the V<sub>OC</sub> of multiple junction cells is close to the sum of V<sub>OC</sub> of the individual cell with a PCE of 1.9%.<sup>[55]</sup> From 2007, the device performance sharply increased year by year. By comparing the single-junction OSCs with sol-gel and ZnO NP ETLs, one can find the highest performance of the single OSCs usually use the sol-gel ZnO as ETLs, which might be due to more difficulties in controlling the defects of the ZnO nanoparticles films. However, in the tandem solar cells, the ZnO NPs were more widely utilized than the sol-gel ZnO. In 2013, a novel polymer PDTP-DFBT was designed and synthesized by the Yang group. With the architecture of ITO/ZnO/P3HT:ICBA/PEDOT:PSS/ZnO/PDTP-DFBT:PCBM/MoO<sub>3</sub>/Ag, a PCE over 10% was certified in tandem OSCs.<sup>[56]</sup> In the same year, the PCE of single-junction cells is inferior to the tandem OSCs. Liao et al. proposed a low-bandgap polymer PTB7-Th and a PCE of 9.35% was achieved based on the ZnO:C<sub>60</sub> composite ETL.<sup>[57]</sup> In 2014, Liu et al. reported the high-performance tandem solar cells with PCE up to 10.8% by controlling the temperature-dependent aggregation behaviors of the donor polymers in

**Table 1.** Performance parameters summary of annual the highest efficiency of the sol-gel ZnO as the ETL in OSCs.

Year	Device structure	$V_{oc}$ [V]	$J_{sc}$ [ $\text{mA cm}^{-2}$ ]	FF [%]	PCE [%]	References
2006	ITO/ZnO/P3HT:PCBM/Ag	0.556	11.22	47.50	2.91	[54]
2008	FTO/ZnO/P3HT:PCBM/MoO <sub>3</sub> /Ag	0.616	8.858	57.00	3.09	[202]
2010	TO/ZnO/CPCBSD/P3HT:ICBA/PEDOT:PSS/Ag	0.84	12.40	60.00	6.22	[203]
2011	ITO/ZnO/ DTG-TPD:PC <sub>70</sub> BM/MoO <sub>3</sub> /Ag	0.85	12.600	68.00	7.30	[204]
2012	ITO/F <sub>16</sub> CuPc NWs/ZnO/PTB7:PC <sub>71</sub> BM/MoO <sub>3</sub> /Al	0.736	15.83	73.85	8.57	[205]
2013	ITO/ZnO-C <sub>60</sub> /PTB7-Th:PC <sub>71</sub> BM/MoO <sub>3</sub> /Ag	0.80	15.73	74.30	9.35	[206]
2014	ITO/ZnO/PfBT4T-2OD:TC <sub>71</sub> BM/MoO <sub>3</sub> /Al	0.77	18.80	75.00	10.80	[58]
2015	ITO/ZnO/PTB7-Th:PC <sub>71</sub> BM/MoO <sub>3</sub> /Al	0.775	19.47	66.90	10.10	[207]
2016	ITO/ZnO/PBDB-T:ITIC/MoO <sub>3</sub> /Al	0.899	16.81	74.20	11.21	[208]
2016	ITO/ZnO/PBDB-T:IT-M/MoO <sub>3</sub> /Al	0.94	17.44	73.50	12.05	[229]
2017	ITO/ZnO/PBDB-T-SF:IT-4 F/MoO <sub>3</sub> /Al	0.88	20.88	71.30	13.10	[209]
2018	ITO/ZnO/PM7:IT-4 F/MoO <sub>3</sub> /Al	0.86	21.80	77.00	14.40	[230]
2019	ITO/ZnO/PM6:Y6/MoO <sub>3</sub> /Ag	0.82	25.20	76.10	15.70	[60]
2021	ITO/ZnO:Zr/PM6:Y6:PC <sub>71</sub> BM/MoO <sub>x</sub> /Ag	0.86	25.80	77.40	17.2	[61]
2022	ITO/ZnO/BA/PBDB-TF:HDO-4Cl:BTP-eC9/MoO <sub>3</sub> /Ag	0.86	26.92	79.49	18.40	[62]

**Table 2.** Performance parameters summary of annual the highest efficiency of the ZnO NP as the ETL in OSCs.

Year	Structure	$V_{oc}$ [V]	$J_{sc}$ [ $\text{mA cm}^{-2}$ ]	FF [%]	PCE [%]	References
2007	ITO/PEDOT:PSS/MDMO-PPV:PCBM/ZnO/LiF/Al	0.820	4.90	57.00	2.3	[231]
2008	ITO/ZnO/C <sub>60</sub> -SAM/P3HT:PCBM/PEDOT:PSS/Ag	0.630	12.60	62.30	4.94	[219]
2012	ITO/ZnO/PDTG-TPD:PC <sub>71</sub> BM /MoO <sub>3</sub> /Ag	0.860	14.10	67.30	8.1	[220]
2013	ITO/PEDOT:PSS/p-DTS(FBTTh <sub>2</sub> ) <sub>2</sub> :PC <sub>70</sub> BM/ZnO/Al	0.799	15.5	72.40	8.9	[221]
2014	ITO/ZnO/PCBE-OH/PBDB-T:PC <sub>71</sub> BM/MoO <sub>3</sub> /Ag	0.920	15.40	66.00	9.4	[222]
2015	ITO/ZnO/PBDB-TS1:PC <sub>70</sub> BM/SWCNT/SAM/MoO <sub>3</sub> /Al	0.780	20.50	65.10	10.5	[223]
2018	ITO/ZnO/PM7:IT-4 F/MoO <sub>3</sub> /Al	0.880	20.90	71.10	13.1	[224]
2019	ITO/ZnO/T1:IT-4 F/MoO <sub>3</sub> /Al	0.899	21.50	78.00	15.1	[225]
2020	ITO/MoO <sub>x</sub> /PM6:Y6/ZnO/Al	0.845	27.43	73.80	17.1	[226]

**Table 3.** Performance parameters summary of annual the highest efficiency of the ZnO as the ETL in tandem OSCs.

Year	Structure	$V_{oc}$ [V]	$J_{sc}$ [ $\text{mA cm}^{-2}$ ]	FF [%]	PCE [%]	References
2007	ITO/PEDOT:PSS/MDMO-PPV:PCBM/ZnO/PEDOT:PSS/P3HT:PCBM/LiF/Al	1.530	3.00	42.00	1.9	[210]
2010	ITO/PEDOT:PSS/PFTBT:PCBM/ZnO/PEDOT/pBBTDPP2:PCBM/LiF/Al	1.580	6.00	52.00	4.9	[211]
2011	ITO/ZnO-d/P3HT:PC <sub>60</sub> BM/MoO <sub>3</sub> /Al/ZnO-d/PSBTBT:PC <sub>71</sub> BM/MoO <sub>3</sub> /Al	1.200	7.84	54.10	5.1	[212]
2012	ITO/ZnO/P3HT:ICBA/PEDOT:PSS/ZnO/PBDDT-DPP:PC <sub>71</sub> BM/MoO <sub>3</sub> /Ag	1.560	8.26	66.80	8.2	[213]
2013	ITO/ZnO/P3HT:ICBA/PEDOT:PSS/ZnO/PDTP-DFBT:PC <sub>71</sub> BM/MoO <sub>3</sub> /Ag	1.530	10.10	68.50	10.6	[214]
2014	ITO/ZnO/P3HT:ICBA/PEDOT:PSS/ZnO/PTB:PC <sub>71</sub> BM/WO <sub>3</sub> /PEDOT:PSS/ZnO/LBG:PC <sub>71</sub> BM/WO <sub>3</sub> /Ag	2.280	7.63	66.40	11.55	[215]
2015	ITO/PEDOT:PSS/PTB7-Th:PC <sub>71</sub> BM/ZnO/CPE-Ph-Na/PTB7-Th:PC <sub>71</sub> BM/Al	1.540	11.11	66.00	11.3	[216]
2016	ITO/CuSCN/DR3TSBDT:PC <sub>71</sub> BM/ZnO/n-PEDOT:PSS/DPPEZnP-TBO:PC <sub>61</sub> BM/PFN/Al	1.625	12.31	62.70	12.5	[217]
2017	ITO//PEDOT:PSS/PBDB-T:ITCC-M/ZnO/PCP-Na/PBDTTT-ET:IEICO/PFN-Br/Al	1.800	12.00	63.90	13.8	[218]
2018	ITO/ZnO/PFN-Br/PBDB-T:F-M/M-PEDOT:PSS/ZnO/PTB7-Th:O6T-4 F:PC <sub>71</sub> BM/MoO <sub>3</sub> /Al	1.642	14.35	73.70	17.36	[59]
2021	ITO/PEDOT:PSS/PM7:TfF-4Cl/ZnO NPs:PEI/PEI/PEDOT:PSS/PCE10:CO <sub>8</sub> DFIC:PC <sub>70</sub> BM/PNDIT-F3N/Ag	1.64	14.59	78.00	18.71	[232]
2022	ITO/ZnO/BA/PB2:GS-ISO/MoO <sub>3</sub> /Ag/ZnO-NPs:PFN-Br/PBDB-TF:HDO-4Cl:BTP-eC9/MoO <sub>3</sub> /Ag	2.03	12.98	74.16	19.56	[62]

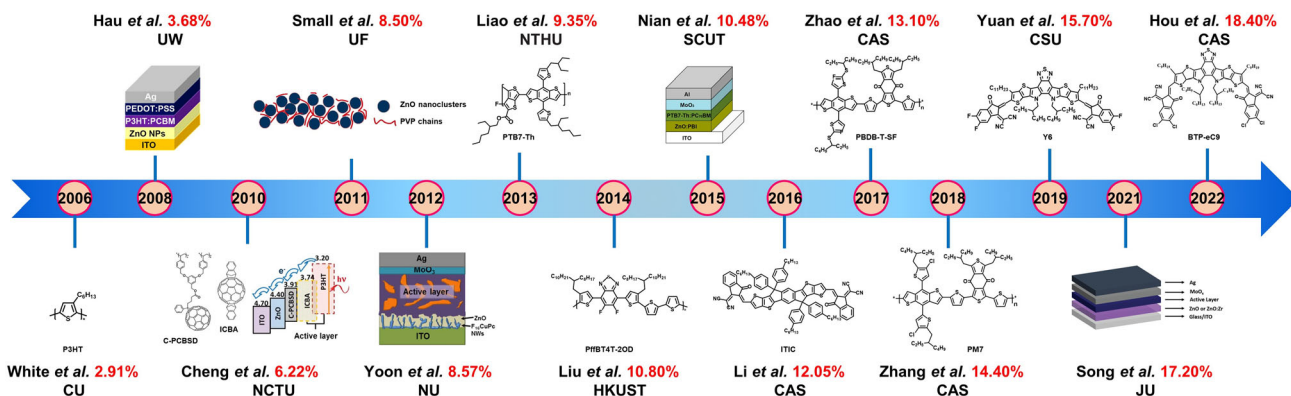


**Figure 11.** The development of ZnO buffer layer-based single-junction OSCs. Reproduced with permission. Copyright 2015, ACS,<sup>[54]</sup> Copyright 2006, AIP,<sup>[58]</sup> Copyright 2014, Springer Nature,<sup>[60]</sup> Copyright 2011<sup>[61]</sup> Cell, Copyright 2011, Wiley-VCH GmbH<sup>[202]</sup>, Copyright 2008, AIP,<sup>[203]</sup> Copyright 2010, ACS,<sup>[204]</sup> Copyright 2011, Springer Nature,<sup>[205]</sup> Copyright 2012, ACS,<sup>[206]</sup> Copyright 2013, Wiley-VCH GmbH,<sup>[207]</sup> Copyright 2015, ACS,<sup>[208]</sup> Copyright 2016, Wiley-VCH GmbH,<sup>[209]</sup> Copyright 2017, ACS Copyright 2008, AIP, Copyright 2010, ACS, Copyright 2011, Springer Nature, Copyright 2012, ACS.

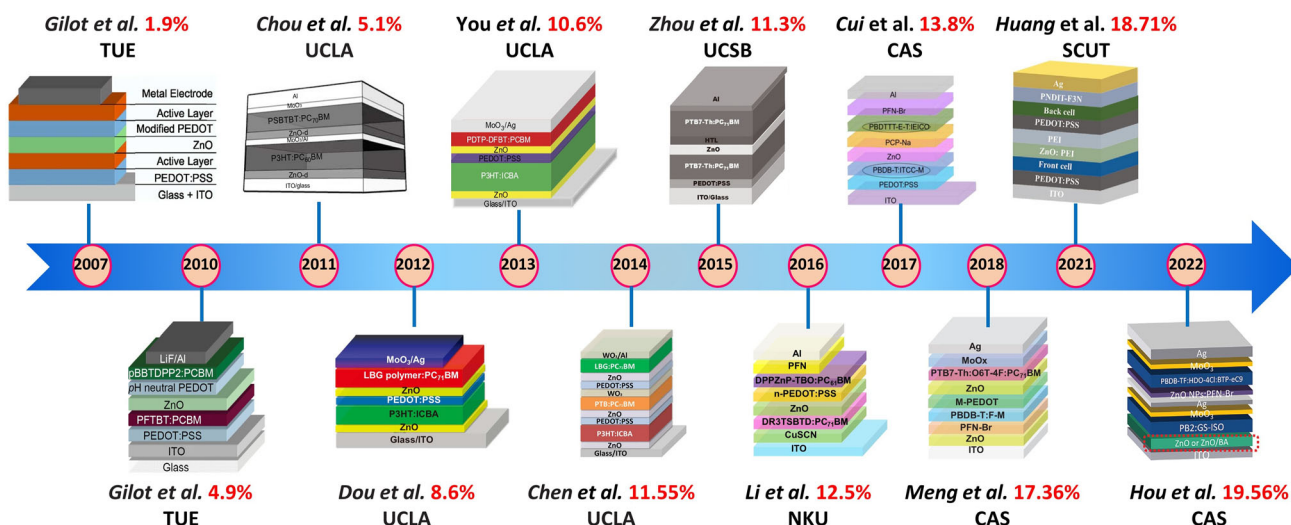


**Figure 12.** The development of ZnO buffer layer-involved tandem OSCs. Reproduced with permission.<sup>[59]</sup> Copyright 2018, Science,<sup>[62]</sup> Copyright 2022, Wiley-VCH GmbH,<sup>[210]</sup> Copyright 2007, AIP,<sup>[211]</sup> Copyright 2010 Wiley-VCH GmbH,<sup>[212]</sup> Copyright, 2011, Wiley-VCH GmbH,<sup>[213]</sup> Copyright, 2012 Springer Nature,<sup>[214]</sup> Copyright 2013, Springer Nature,<sup>[215]</sup> Copyright 2014, Wiley-VCH GmbH,<sup>[216]</sup> Copyright 2015, Wiley-VCH GmbH,<sup>[217]</sup> Copyright 2016, Springer Nature,<sup>[218]</sup> Copyright 2017, ACS,<sup>[232]</sup> Copyright 2021, Wiley-VCH GmbH. Copyright 2007, AIP, Copyright 2010, Wiley-VCH GmbH, Copyright 2010, Wiley-VCH GmbH, Copyright 2012, Springer Nature, Copyright 2013, Springer Nature, Copyright 2014, Wiley-VCH GmbH, Copyright 2015, Wiley-VCH GmbH, Copyright 2016, Springer Nature, Copyright 2017, ACS, Copyright 2018, Science, Copyright 2021, Wiley-VCH GmbH, Copyright 2022, Wiley-VCH GmbH.

inverted OSCs with ZnO as the ETL.<sup>[58]</sup> In 2018, Meng et al. reported the tandem solar cells with an inverted structure of ITO/ZnO/PFN-Br/PBDB-T:F-M/M-PEDOT:PSS/ZnO/PTb7-Th:O6T-4F:PC<sub>71</sub>BM/MoO<sub>3</sub>/Al with a PCE of 17.36%.<sup>[59]</sup> And just next year, Yuan et al. developed a new fullerene acceptor Y6, a PCE of 15.7% with the structure of ITO/ZnO/PM6:Y6/MoO<sub>3</sub>/Ag was reported.<sup>[60]</sup> In 2021, Song et al. brought in Zr doping ZnO ETL and a boosted PCE of 17.2% was exhibited based on a structure of Zr:ZnO/PM6:Y6:PC<sub>71</sub>/MoO<sub>x</sub>/Ag.<sup>[61]</sup> In 2022, Hou et al.<sup>[62]</sup> reported a single-junction OSC with PCE of 18.40% based on boric acid (BA)-treated ZnO as the ETL, and a tandem OSC with PCE of 19.56% employing ZnO NPs as the interface layer, which are the highest performances till today.

In all, the ZnO ETL used for OSCs should have good electron mobility to enable interface charge transfer and collection ability,

otherwise low short-circuit current ( $J_{sc}$ ) and fill factor (FF) would be observed. The electrical properties of ZnO ETL are greatly influenced by surface chemical defects, crystal quality, and film quality. Though a variety of approaches were used to prepare the ZnO ETL, the most widely used ZnO ETL for organic photovoltaics was fabricated through the sol-gel method, and the nanoparticles route through the chemical reaction of KOH and ZrOAc<sub>2</sub>.

#### 4.2. The Application of Solution-Processable ZnO in PVSCs as the Electron Transporting Layer

The ZnO-involved PVSCs have three kinds of device structures, i.e., the n-i-p-type (Figure 14a), p-i-n type planar PVSCs (Figure 14b), and the mesostructured PVSCs (Figure 14c).

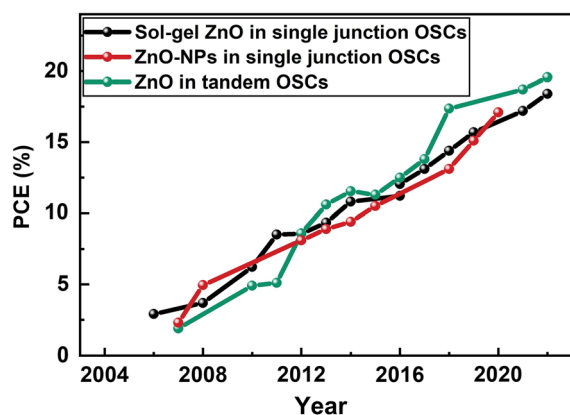


**Figure 13.** The efficiency development of the single-junction OSCs with sol-gel ZnO and ZnO NP ETLs, and the tandem OSCs employing ZnO NPs.<sup>[54,58–61,202–226]</sup>

The ZnO nanoparticles that have been widely used in the OSCs were also used in the n-i-p-type planar PVSCs. In this synthesis route, the ZnO nanoparticles were synthesized through the chemical reaction between KOH and ZnAcO<sub>2</sub> in methanol. On the top of this ZnO ETL, the perovskite (PVSK) films were fabricated using a two-step deposition route, in which the PbI<sub>2</sub> film was first spin-coated on the top of the ZnO layer, drying the film was dipped in the CH<sub>3</sub>NH<sub>3</sub>I solution for a while. The spiro-OMeTAD hole transporting layer was deposited on top of the perovskite layer. The obtained device presented an optimized performance of 15.7%.<sup>[63]</sup> In comparison with the TiO<sub>2</sub> that needs to be thermally annealed at high temperatures, the ZnO nanoparticle-based ETL is more suitable for low-temperature and flexible usage. Therefore, the ZnO nanoparticle ETLs were used to fabricate flexible PVSCs. Hwang et al. fabricated PVSCs through the fully slot-die coating. In the structure of ZnO/perovskite/PCBM/Al, the ZnO ETL, the perovskite layer, and the PCBM layer were fabricated using a 3D slot-die printer. In this work, the ZnO nanoparticles were first synthesized and formed into electronic inks.<sup>[64]</sup>

In the p-i-n structure solar cells, the ZnO nanoparticle-based ETL was deposited on the top of the PCBM ETLs to improve the device performance and stability. The ZnO nanoparticles were prepared through a general process with KOH and ZnOAc<sub>2</sub> as the raw materials.<sup>[65]</sup> The obtained ZnO nanoparticles were dispersed in a mixed solvent of n-butanol and methanol or ethanol.<sup>[66]</sup> It was reported that Al will be oxide by the perovskite

components in the air in the ITO/PEDOT:PSS/perovskite/PC<sub>61</sub>BM/Al devices. However, the insertion of ZnO between Al and PC<sub>61</sub>BM suppressed the chemical reaction between the metal electrode and perovskite components, thereby increasing the air stability of the devices.<sup>[67]</sup> Figure 15a shows the cross-sectional scanning electron microscope (SEM) image of the device. PC<sub>61</sub>BM showed inhomogeneous coverage on the top of the perovskite layer and very thin PC<sub>61</sub>BM capping layers in some places were observed. An additional homogenous ZnO layer on the top of PC<sub>61</sub>BM layer created a physical buffer between the metal and the perovskite layer. The best device gave an efficiency of 14.2% as shown by the J-V characteristics, external quantum efficiencies (EQE) spectra, and the histogram of PCE. The ZnO nanoparticles were also deposited on the top of the perovskite layer to replace the PCBM layer. In the research of You et al.<sup>[68]</sup> both NiO<sub>x</sub> and ZnO were used in the PVSCs as the hole extraction and electron extraction layer, respectively. Because the ZnO layer is deposited directly on the top of PVSK films, the ZnO nanoparticles were dispersed in chlorobenzene instead of the mixed solution of methanol and butanol. The device performance reached 16.1%, which was better than the regular device with PEDOT:PSS and PCBM buffer layer. Moreover, this device showed significantly improved stability, with 90% performance remaining after 60 days of testing in ambient air with 30%–50% humidity. Figure 15d–i shows the device structure, energy level, photoluminescence spectra of the films, and the evolution of the device performance during long-term aging in air.

In the mesostructured PVSCs, various nanostructured ZnO, such as ZnO nanorod,<sup>[69–71]</sup> nanowire arrays, nanowalls,<sup>[72]</sup> and Al-doped ZnO nanorods,<sup>[73]</sup> were used as the ETLs. The ZnO nanostructures layers were fabricated by hydrothermal or chemical bath process. For the hydrothermal method of nanostructured ZnO, Zn salt and alkali were dissolved in the solvent and reacted with each other to form Zn(OH)<sub>2</sub> precipitates. With the increase of temperature and pressure, the PH value of the solution increase, while the concentration of Zn<sup>2+</sup> decreases. As a consequence, the Zn(OH)<sub>2</sub> precipitates converted to ZnO. The morphology of the nanorods was regulated by changing the composition and concentration of the precursors, as well as the reaction temperature and time.<sup>[74]</sup> Table 4 lists the application of ZnO nanowire and nanorods collection in the PVSCs. The ZnO nanorod usually is fabricated based on a two-step method. First, ZnO seed layer was prepared by spin coating the Zn(CH<sub>3</sub>COO)<sub>2</sub>·2H<sub>2</sub>O solution,<sup>[75]</sup> or electrodeposition, electro-spraying,<sup>[70]</sup> sputtering methods. Then ZnO nanorod is grown

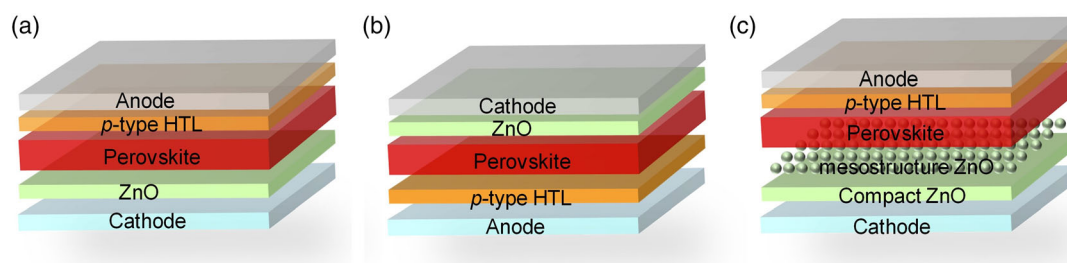


**Figure 14.** The device structure of ZnO employed PVSCs: a) electron extraction layer in the n-i-p structured PVSCs, b) electron extraction layer in the p-i-n type planar PVSCs, c) electron extraction layer in the mesostructured type PVSCs.

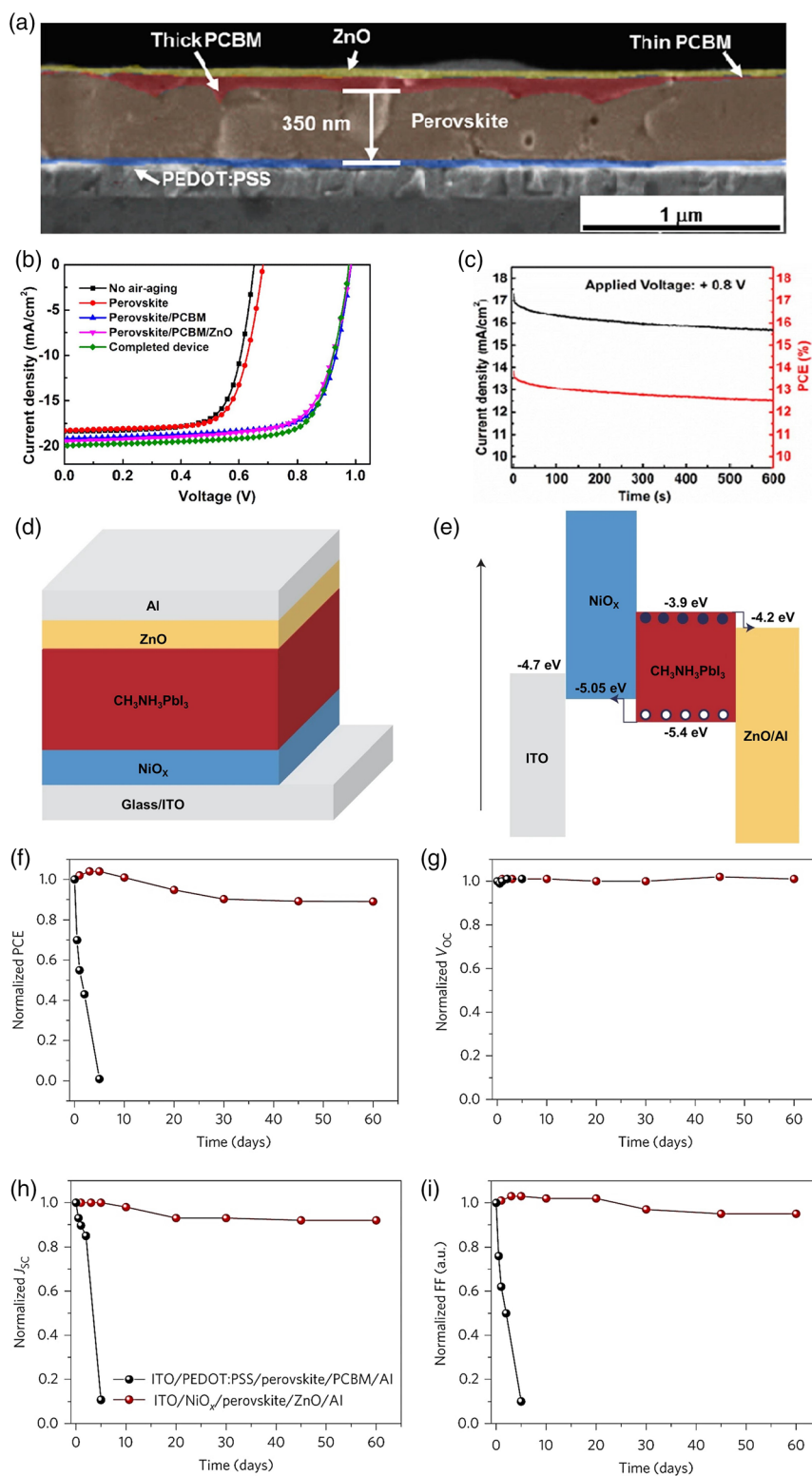


**Figure 15.** a) Cross-sectional SEM images of the PVSCs with PCBM/ZnO ETL, b)  $J$ - $V$  characteristics and EQE spectra of the device. c) Evolution of current density. Reproduced with permission.<sup>[67]</sup> Copyright 2015, Elsevier. d,e) Device structure and energy level of PVSCs containing low-temperature ZnO ETL and  $\text{NiO}_x$  HTL. f-i) The evolution of the device performance of ITO/PEDOT:PSS/perovskite/PCBM/Al, and ITO/ $\text{NiO}_x$ /perovskite/ZnO/Al cells. Reproduced with permission.<sup>[68]</sup> Copyright 2016, Springer Nature.

**Table 4.** Summary of the PVSCs based on ZnO nanorods and nanowire electron collection layer.

Device structure	$V_{OC}$ [V]	$J_{SC}$ [ $\text{mA cm}^{-2}$ ]	FF [%]	PCE [%]	References
FTO/ZnO seed layer/ZnO nanorods+MAPbI <sub>3</sub> /spiro-MeOTAD/Au	0.991	20.08	56.00	11.13%	[75]
FTO/ZnO seed layer/ZnO nanorods/MAPbI <sub>3</sub> /spiro-oMeTAD/Ag	0.965	21.50	70.00	16.12%	[70]
FTO/ZnO dense layer/ZnO 0.9nanorods+MAPbI <sub>3</sub> /spiro-oMeTAD/Au	0.900	19.77	60.00	10.07%	[233]
FTO/ZnO seed layer/ZnO nanorods+MAPbI <sub>3</sub> /spiro-oMeTAD/Au	1.023	22.42	71.43	16.08%	[234]
ITO/ZnO seed layer/ZnO:I nanorods/MAPbI <sub>3</sub> /spiro-OMeTAD/Ag	1.130	22.42	71.99	18.24%	[235]
ZnO/TiO <sub>2</sub> core-shell+MAPbI <sub>3</sub> /	0.960	19.85	66.00	15.33%	[71]
Fiber shape: ZnO seed/ZnO nanorods/MAPbI <sub>3</sub> /spiro-oMeTAD/CNT sheet	0.800	7.520	43.00	3.80%	[236]
ITO/ZnO nanowall/MAPbI <sub>3</sub> /spiro-oMeTAD/Ag	1.000	18.90	72.10	13.60%	[72]

on the ZnO seed layer from the chemical bath or hydrothermal method, where the ZnO seed layer is immersed in the solution of  $\text{Zn}(\text{CH}_3\text{COO})_2 \cdot 2\text{H}_2\text{O}$  and hexamethylenetetramine.<sup>[72]</sup> The diameter and length of ZnO nanorod are varied by changing the solution concentration and the immersion reaction time, respectively. Finally, the ZnO nanorod films are attained by high-temperature annealing. Further, the conduction of ZnO nanorod was improved through nitrogen doping.<sup>[70]</sup> In addition,

polyelectrolyte polyethyleneimine (PEI) was relied on to reduce the diameter and promote the aspect ratio of ZnO nanorod arrays during the hydrothermal growth process (Figure 16a,b).<sup>[70]</sup> The introduction of PEI formed a PEI-capped ZnO layer, leading to higher aspect ratio of ZnO arrays. Compared to the pure N:ZnO array, the PEI-capped N:ZnO arrays formed the buffer layer and the perovskite layer (Figure 16c–f). A low aspect ratio and dense ZnO:I nanopillar

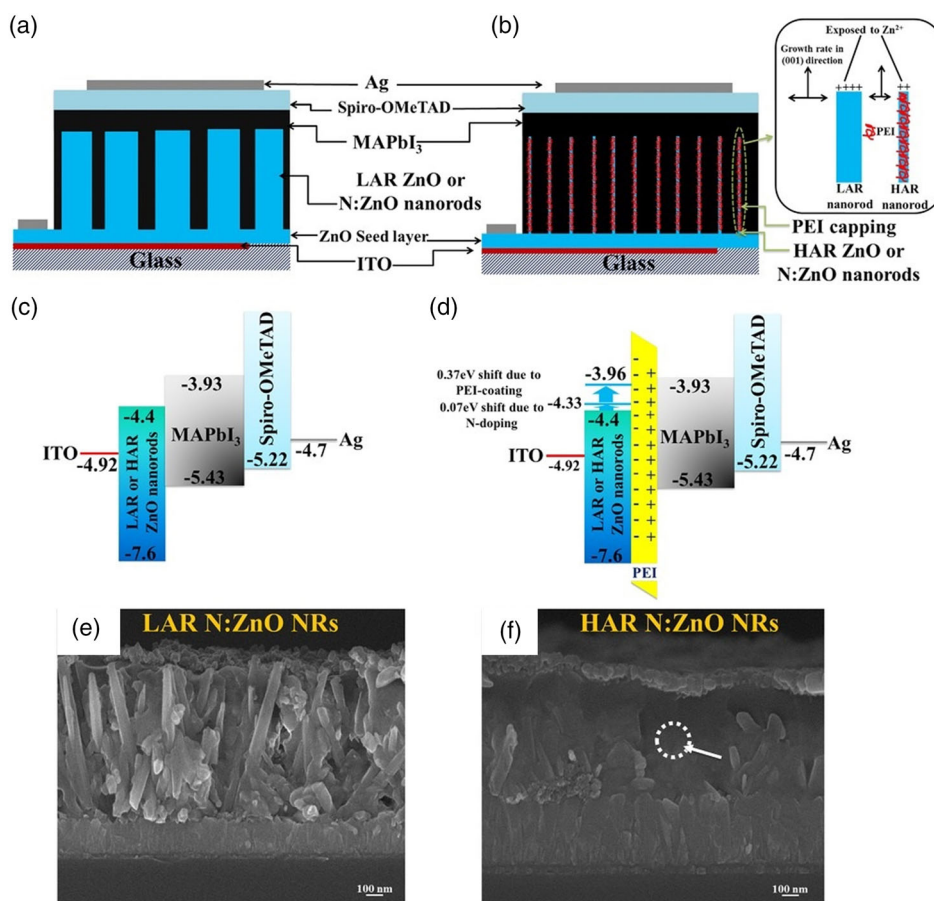


**Figure 16.** Schematics of device structure based on a) conventional LAR NR arrays and b) HAR NR arrays with additional PEI coating in the inset shows the schematic representation of PEI as a capping agent to control nanorod growth). Energetic diagram of the devices based on c) LAR or HAR NRs without PEI coating and d) LAR or HAR NRs with PEI coating. The conduction band energy of ZnO was lowered by 0.07 eV due to nitrogen doping and by 0.37 eV due to dipole formation by the PEI layer. e) Cross-sectional SEM images of complete cells based on 1070 nm LAR N: ZnO NRs without PEI coating, and f) HAR N ZnO NRs. Note: LAR, low aspect ratio; HAR, high aspect ratio. Reproduced with permission.<sup>[70]</sup> Copyright 2015, Wiley-VCH GmbH.

array was reported due to the suppression of crystal growth of hexagonal single crystal ZnO along the [0001] direction by doping iodine during the ZnO nanorod growth process, which promoted the PCE of PVSCs to 18.24%.<sup>[76]</sup> Regarding the growth of ZnO nanowalls, the ZnO nanowalls usually grew with thin Al as seed layer through a chemical bath method with a precursor solution at 80 °C for 6 h. Due to the better interfacial contact and reduced recombination with the ZnO nanowalls ETL, the PCE of the PVSK solar cell was improved from 11.3% to 13.6%.

These solution-processable nanostructured ZnO were used as a replacement of TiO<sub>2</sub> in the PVSCs, but fabricating high-quality and uniform perovskite films on the top of this nanostructured ZnO is more difficult.

#### 4.3. The Application of Solution-Processed ZnO in CIGS/CZTS Solar Cells

Chalcopyrite-based thin films (In,Ga)(Se,S)<sub>2</sub> (CIGS, GIGSe) solar cell is regarded as promising alternatives to crystalline silicon solar cells due to the high absorption coefficient, tunable bandgap, and flexibility. CIGS and CIGSe solar cells have reached the highest efficiency up to 23.07%<sup>[77]</sup> and 22.9%.<sup>[78]</sup> In the structure of CIGS and CIGSe solar cells, CdS is a frequently used buffer layer. ZnO is used as the window layer to reduce the charge recombination between the top electrode and the active layer. In addition, ZnO, ZnS, and ZnSe are important Cd-free alternatives for buffer layers.

In addition, Cu<sub>2</sub>ZnSnS<sub>4</sub> (CZTS) also has drawn worldwide attention due to its earth-abundant, nontoxic element constitution, and remarkable photovoltaic performance. CZTS is a direct bandgap energy material that could be tuned from 1.5 eV for CZTS to 1.0 eV for CZTSe, In CZTS, the CIGS ternary chalcopyrite structure is derived by replacing Zn<sup>2+</sup> with Cu<sup>+</sup> and In<sup>3+</sup>/Ga<sup>3+</sup>, while the CZTS quaternary structure is derived by replacing In<sup>3+</sup>/Ga<sup>3+</sup> with Zn<sup>2+</sup> and Sn<sup>4+</sup>. The state-of-the-art PCE of CZTS solar cells has reached above 13%.<sup>[79]</sup> CZTS solar cell is typically a composite of Mo back-contact layer, CZTS light absorber, CdS buffer layer, ZnO/AZO/In<sub>2</sub>O<sub>3</sub>/ZnSnO/ITO window layer, and metal grid top electrode. **Figure 17** shows the schematic of the structure of CZTS solar cells. In such a structure, the use of a window layer would reduce charge

recombination and improve V<sub>OC</sub> of the device. It is a challenge to prepare a highly crystallized ZnO interlayer using low-temperature solution processes because the low-temperature deposited ZnO layer has a relatively low charge transport property. Even so, an all-solution-processed CZTS solar cell is a great research object, Hao et al. reported full-solution-processed CZTS with ZnO buffer layer and Ag NWs top electrode.<sup>[80]</sup> The ZnO/AgNWs window layer acted as both the window layer and top electrode. In addition, AZO is also inserted between the Mo back electrode and CZTS absorber to suppress the MoS<sub>2</sub> formation. With such a layer on top of Mo, the device efficiency was improved from 7.13% to 8.44%.<sup>[81]</sup>

#### 4.4. The Application of Solution-Processed ZnO in Quantum Dot Solar Cells

Quantum dot solar cell is also a kind of full-solution-processable thin film solar cell. Lead chalcogenides, which have uniquely large dielectric constants and large exciton Bohr radii, were the photoactive materials in the quantum dot solar cells. The performance of quantum dot solar cells has developed rapidly since 2005, and the highest performance of quantum dot solar cells has reached higher than 15%.<sup>[82]</sup> The ZnO nanocrystals on the top of PbS/PbSe quantum dot helped to increase the voltage relative to the Schottky-junction quantum dot solar cell due to the creation of a pseudo-p-n junction between the quantum dot and ZnO. Leschkie et al. first reported the p-n junction structure of PbS and ZnO.<sup>[83]</sup> Similar to the OSCs with an inverted structure, ZnO was deposited underneath the PbS/PbSe films when a high-work function metal was deposited on the top of the quantum dot layer. **Figure 18** is the typical device structure of PbS/PbSe solar cells with ZnO layers.

#### 4.5. Applications of ZnO and Doped ZnO as Composite Electrode and Encapsulation Layer

Besides the use of ZnO as ETL in the OSCs and PVs, the ZnO nanoparticles also have been used to modify the Ag nanowires electrodes to form a composite electrode. Han et al. spray-coated the ZnO nanoparticles on the top of the spray-coated Ag

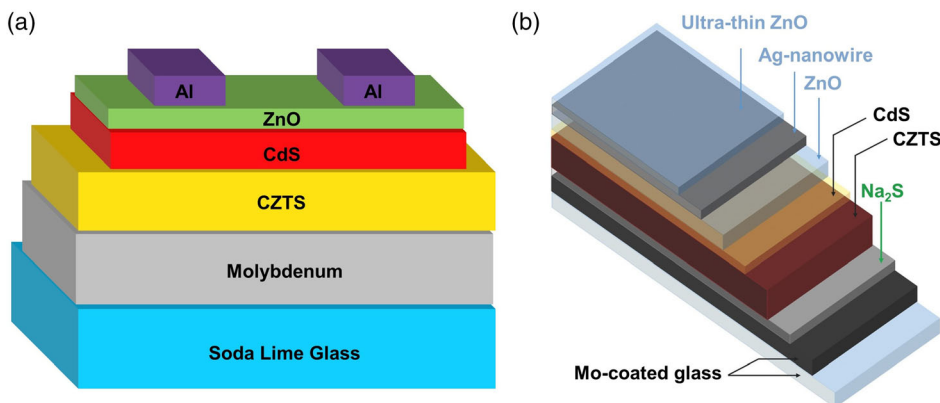


**Figure 17.** a) Schematic structure of the common CIGS, CZTS solar cells. b) ZnO/AgNWs as the window layer and top electrode. Reproduced with permission.<sup>[80]</sup> Copyright 2018, Wiley-VCH GmbH.

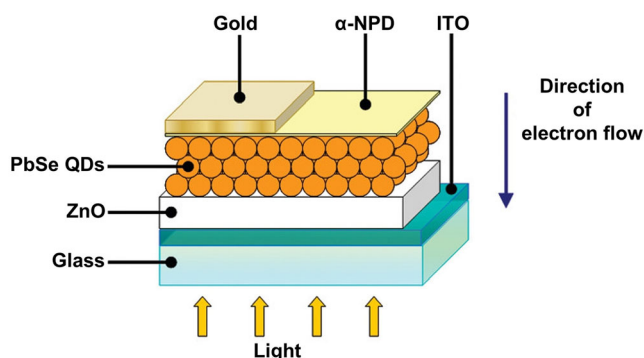


**Figure 18.** The device structure of quantum dots with inverted and conventional structures. Reproduced with permission.<sup>[83]</sup> Copyright 2009, ACS.

nanowire for the semitransparent PVSCs (as shown in **Figure 19**).<sup>[84]</sup> To ensure good transmission of the semiconductor electrode, the thickness of the Ag NWs should be controlled

within 50 nm, which formed a relatively high sheet resistance of the electrode. With a thin ZnO layer on the top of the Ag NWs, the sheet resistance of the Ag NWs/ZnO composite decreased from 78 to 30  $\Omega \square^{-1}$ . In addition, because of the light scattering effect of ZnO nanoparticles, the light transparency in the visible light range slightly increased. These improved conduction and light transmittance proportions made the performance of the semitransparent PVSCs improved from 7.3% to 11.13%, and the performance of 1 cm<sup>2</sup> semitransparent cells also reached 8.18%.

In comparison with the Ag NWs transparent bottom electrode, the combination of Ag NWs and ZnO also gave several improved performances. Li et al. welded the Ag nanowire networks and improved the conductivity of the Ag nanowire electrodes through the capillary force and secondary growth of AZO. With this, the performance of the flexible OSCs improved from 12.19% to 15.21%, and the PCE of 1 cm<sup>2</sup> cell also increased to 12.28%.<sup>[85]</sup> Similarly, Chen et al.<sup>[86]</sup> found the tight fill of ZnO NPs in the Ag NWs networks, together with the strong

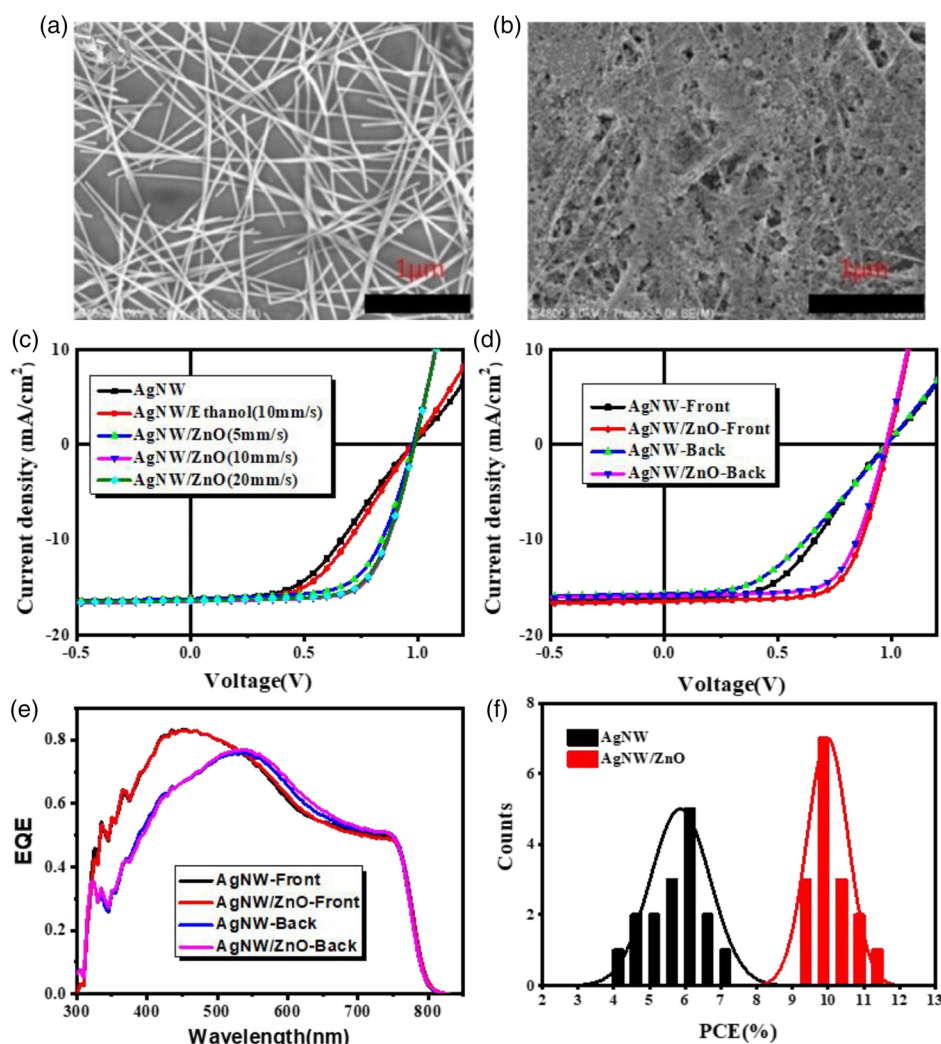


**Figure 19.** a) SEM images of the Ag NWs and b) Ag NWs/ZnO composite electrode. c)  $J$ - $V$  curves of the PVSCs with Ag NW and AgNW/ZnO electrodes. d)  $J$ - $V$  curves of the best device fabricated illuminated from the ITO side and Ag NW electrode, respectively. e) Corresponding EQE characteristics of the device. f) Histogram of PCE of 16 individual cells with AgNW and AgNW/ZnO composite electrode. Reproduced with permission.<sup>[84]</sup> Copyright 2018, Elsevier.

binding of the substrate and PSSNa, and the capillary force of the crossed silver nanowire enabled super mechanical stability of the flexible OSCs. The energy-dispersive spectroscopy (EDS) of the Ag NWs/ZnO proved the uniform existence/distribution of zinc (Zn) element (from ZnO) around AgNWs, which might be due to the strong interaction and bonding between ZnO and FlexAgNE layers in the combined FlexAgNE/ZnO structure (as shown in **Figure 20**). Similarly, Tang et al. (**Figure 21**) used the sol-gel ZnO to parlay the nanostructured Ag NWs electrode. Due to the broadband light trapping and suppressed charge recombination loss, the device showed a significant increase in short-circuit current and efficiency improvement in comparison with the reference devices.<sup>[87]</sup> For the PM6:IT-4F device, the device with such a trapped light structure presented a  $J_{SC}$  of  $22.26 \text{ mA cm}^{-2}$ , much higher than the ITO-electrode-based device ( $19.86 \text{ mA cm}^{-2}$ ). Kang et al. reported a sol-gel ZnO layer on the top of the Ag nanowires electrode could passivate the ion migration and the corrosion of the Ag electrode, leading to the enhancement of performance and long-term stability.<sup>[88]</sup> Time-of-flight secondary ion mass spectrometry (ToF-SIMS) results proved the migration of iodine ions was largely suppressed by the compact sol-gel ZnO layer. The chemical stability is another main problem of the transparent electrode based on Ag NWs. They found the pure Ag NWs showed an increase of sheet resistance from  $27.2$  to  $44.2 \Omega \text{ sq}^{-1}$  when stored in air for 8 months. With a sol-gel ZnO layer, the sheet resistance only increased from  $28.3$  to  $31.3 \Omega \text{ sq}^{-1}$ . We can see such kind of composite electrode containing Ag NWs and ZnO NPs shows several advantages: 1) improved conduction of the flexible electrode due to the welding effect, 2) improved chemical stability because of the moisture and oxygen resistance, 3) suppression of chemical reaction between Ag and iodine ions, and 4) good mechanical bending resistance. These feature the

composite electrode as a good choice both as the bottom and top electrode for the organic and PVSCs.

In addition, ZnO could also act as an encapsulation layer of the organic and PVSCs. Jiang et al. used UV resin ( $400 \mu\text{m}$ ) encapsulation with a ZnO buffer layer to enhance the stability of the device. In this encapsulation structure, ZnO buffer layer is used to minimize the damage from acetone in UV resin film and the thermosetting property of UV resin. With such an encapsulation structure, the PCE degrades by 20.5% after 672 h storage in air for the inverted OSCs.

## 5. Optimization of Device Performance and Stability in the ZnO-Involved Photovoltaic Cells

### 5.1. Defects in Solution-Processed ZnO and the Impact

Though ZnO is the most widely used metal oxide buffer layer in OSCs, there are still several issues with the solution-processable ZnO. For example, because of surface defects, the ZnO-involved inverted solar cells always suffer from light-soaking problems. Meanwhile, the surface defects of ZnO always caused inferior charge transfer and poor device performance. Besides, the ZnO nanoparticles are not stable as suspension and tend to agglomerate due to the polymerization reaction of particles. Encouragingly, several approaches have shown great potential to solve these problems.

#### 5.1.1. Defects of ZnO Interface Layers and the Influence on the Device Performance

As the ETL, the photoelectric properties of the ZnO layer largely affected the device performance of the OSCs and PVSCs. ZnO is

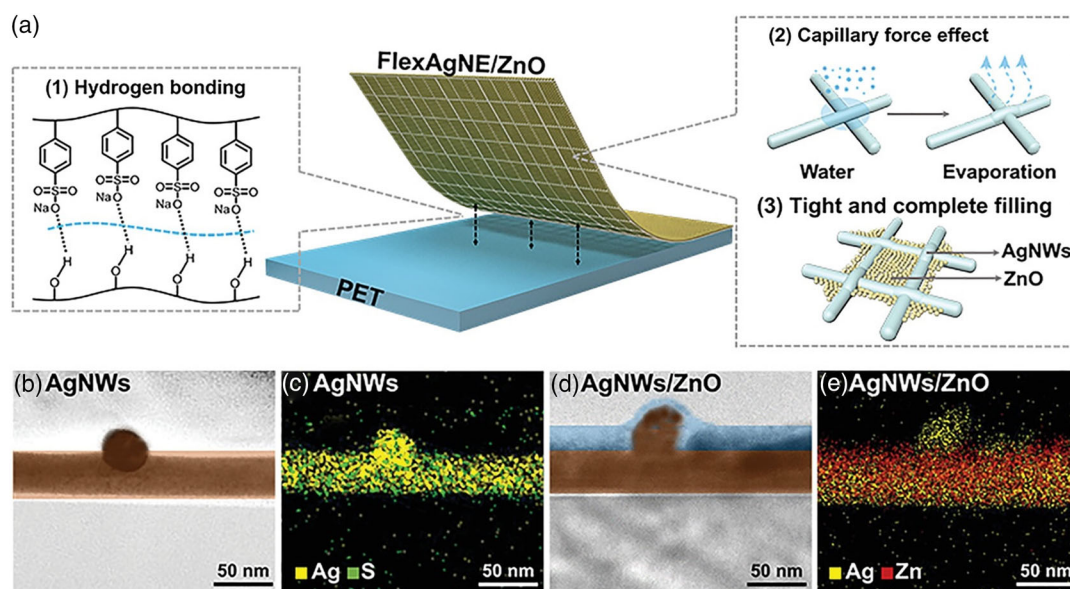


**Figure 20.** a) Schematic diagram of the mechanism: 1) the hydrogen bond effect between the PET substrate and the hydrophilic polyelectrolyte (PSSNa); 2) the capillary force effect of crossed AgNWs junction, and 3) tight and complete filling of ZnO in grid-like AgNWs network. b) TEM images for the crossed AgNWs junction, which is cut from FlexAgNE using a FIB. c) EDS mapping of the sample in Figure 20b. d) TEM images for the crossed AgNWs junction coated with ZnO (AgNWs/ZnO), which is cut from the FlexAgNE/ZnO stacks using a FIB. e) EDS mapping of the sample. Reproduced with permission.<sup>[86]</sup> Copyright 2021, Wiley-VCH GmbH.

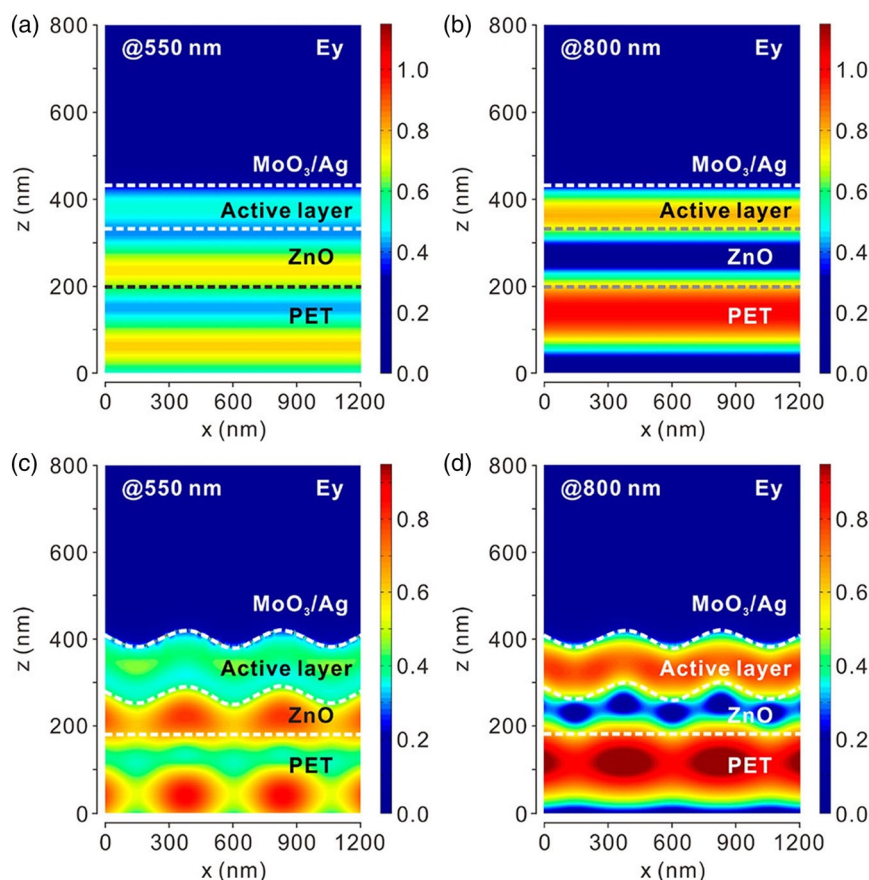


**Figure 21.** Simulated cross-sectional near-field profiles in a flat device structure for TE polarized light at a) 550 nm and b) 800 nm. Near-field profiles in moth-eye nanopatterned device for TE polarized light at c) 550 nm and d) 800 nm. Reproduced with permission.<sup>[87]</sup> Copyright 2019, ACS.

a wide bandgap semiconductor with a bandgap of about 3.3 eV. Under the excitation of UV light, the ZnO would emit a UV-blue emission, which was ascribed to the band-shift emission. However, there are several kinds of defects in the solution-processable fabricated ZnO films, and various defect emissions would be observed as well. The emission peaks due to the electron transfer from the defect energy levels to the exciting level of ZnO include red, yellow, green,<sup>[89,90]</sup> and blue,<sup>[91]</sup> which were related to the Li<sup>+</sup> doping, oxygen interstitial, oxygen vacancy, and zinc interstitial defects, respectively.<sup>[92]</sup> However, as the ZnO nanoparticles containing different defects were used in the inverted OSCs, nearly the same performance was obtained, suggesting the intrinsic defect type does not affect the charge extraction properties from ZnO to the active layer. For the P3HT:PC<sub>61</sub>BM, PTB7-Th:PC<sub>71</sub>BM, and PBDB-T-SF:IT-4F, the PCE was researched to 4%, 8%, and 10% respectively.<sup>[93]</sup>

### 5.1.2. Defects-Related Light-Soaking Issues and Solutions in the ZnO-Involved OSCs

Although the ZnO ETL has the advantages of being low cost, less toxic, and easy to synthesize, this kind of buffer layer also suffers the problems of low electron mobility and ease of absorbing oxygen due to the surface ligands. A typical problem of ZnO ETL is

the well-known “light soaking” issue, which means the ZnO ETL employed inverted solar cells need to be illuminated under white or UV light for several minutes to obtain normal *J*-*V* characteristics (as shown in Figure 22a–d). Red, green, or blue light illumination doesn’t take a positive effect on eliminating the “S”-shaped *J*-*V* curves (as shown in Figure 22b).<sup>[94]</sup> In fact, light soaking is also observed in the TiO<sub>2</sub> ETL-involved inverted solar cells. However, SnO<sub>2</sub> is considered a universal “light-soaking” free electron extraction material for OSCs.<sup>[95]</sup> The “S”-shaped *J*-*V* curves were always ascribed to the low electron transport efficiency of ZnO or TiO<sub>2</sub> because of surface absorbed negatively charged oxygen. The surface-absorbed oxygen would cause a hole reservoir to accumulate at the interface of the metal oxide and organic layer. Therefore, UV or white illumination of ZnO or TiO<sub>2</sub> film before depositing the organic active layer could partly solve this problem.<sup>[96]</sup> The detailed mechanism could be described in Figure 22e. Under the illumination of UV or white light, positive charge carriers would form in ZnO or TiO<sub>2</sub>, leading to the desorption of the absorbed oxygen from the ZnO surface, and then increasing the electron mobility.<sup>[97]</sup> In addition, as shown by Figure 22f,g, the removal of the surface absorbed the negatively charged oxygen would cause the rearrangement of the Fermi levels and lower the barrier width. Therefore, the electron accumulation would be eliminated,

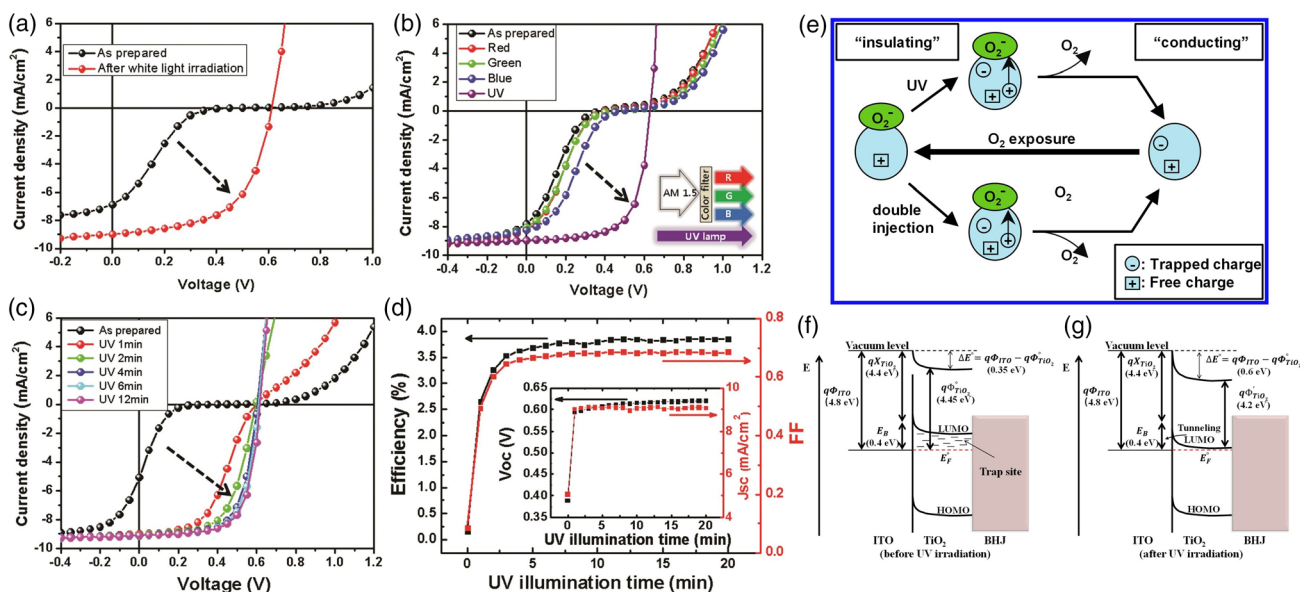


**Figure 22.** a, b)  $J$ - $V$  characteristics of the inverted OSCs under the illumination of different irradiations. c) The evolution of the  $J$ - $V$  characteristics of the ZnO/TiO<sub>2</sub> employed inverted inorganic solar cells after UV soaking for different time. d) The evolution of the device performance. Reproduced with permission.<sup>[94]</sup> Copyright 2012, IOP. e) Schematic illustration of the induction of free charge carrier in ZnO nanoparticles by either UV illumination or injection through electrical contacts and their removal by O<sub>2</sub>. Reproduced with permission.<sup>[97]</sup> Copyright 2010, RSC. Energy levels of the inverted OSCs f) before and g) after UV irradiation. Reproduced with permission.<sup>[94]</sup> Copyright 2012, IOP.

and the device performance improved as well.<sup>[94]</sup> The charge accumulation in the inverted OSCs during light soaking was proved by electron paramagnetic resonance (ESR) measurement both in the TiO<sub>x</sub><sup>[98]</sup> and TiO<sub>2</sub> employed cases.<sup>[99]</sup> Further observation considered the surface hydroxy group can capture an electron, strongly suggesting the passivation of the residual -OH groups is necessary to avoid the light-soaking phenomenon.

Because the light-soaking issue is surface-absorbed oxygen related, it should be reversible in air, which means the device after light soaking would recover to an abnormal device performance as exposing the device to the air again. Wilken et al.<sup>[100]</sup> and Lin et al.<sup>[101]</sup> have found such a reversible phenomenon in the ZnO and TiO<sub>2</sub> involved in inverted organics solar cells. A popular method to eliminate or reduce this problem is generally using chemical-doped ZnO or TiO<sub>2</sub>, i.e., Al:ZnO,<sup>[102]</sup> F:TiO<sub>2</sub>,<sup>[103]</sup> and

Sn:TiO<sub>2</sub>.<sup>[104]</sup> In addition, Riedl et al.<sup>[102]</sup> found the “light soaking issue” is an interface dominant effect between the buffer layer and the organic photoactive layer. Thus, an extra layer of AZO on top of TiO<sub>2</sub> could eliminate the soaking issue. Recently, some researchers found the surface modification of ZnO or TiO<sub>2</sub> nanoparticles through organic compounds could also solve the light-soaking problem. As investigated by Kuwabara et al.,<sup>[99]</sup> the surface -OH group of metal oxides can capture electron. Therefore, the removing the surface -OH groups would be a possible strategy to solve the light-soaking problem. Wei et al. (as showed by **Figure 23**) used the 3-aminopropyltrimethoxysilane (APTMS)-capped ZnO as the ETL of the OSCs. Because most of the surrounding -OH groups have been replaced by the -Si-O- groups, and the absorption of surface oxygen would be suppressed (Figure 23a), thus the device presented light-soaking-free  $J$ - $V$  characteristics (as shown in

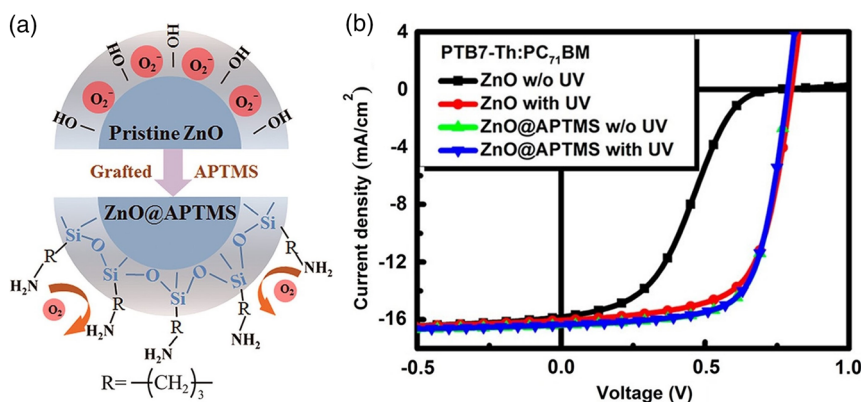


**Figure 23.** a) Schematic diagram of the ZnO and ZnO@APTMS nanoparticles. b)  $J$ - $V$  characteristics of the inverted OSCs with pristine ZnO and ZnO@APTMS buffer layers. Reproduced with permission.<sup>[105]</sup> Copyright 2018, ACS.

Figure 23b).<sup>[105]</sup> For the PTB7:PC<sub>71</sub>BM inverted devices with pristine ZnO ETL, typical “S”-shaped *J*–*V* curves were observed. After 5 mins soaking under UV light, the *J*–*V* characteristics changed to be normal. In contrast, with ZnO@APTMS ETL, similar *J*–*V* characteristics were observed both in case of w/o and with UV light soaking. As a consequence, they achieved 9.07% and 7.97% efficiency for the PTB7-Th:PC<sub>71</sub>BM and PffBT4T-2OD:PC<sub>61</sub>BM inverted OSCs without soaking treatment. Wang et al. used UV pretreatment and bis(2,4-pentanedionate) (TOPD) doping to eliminate the light soaking issue for the TiO<sub>2</sub>-based inverted OSCs and achieved PCE of 10.5% for the PTB7-Th:PC<sub>71</sub>BM cells.<sup>[106]</sup> Ma et al.<sup>[107]</sup> found that the use of the doping ZnO nanoparticles with N, S-doped carbon quantum dot also could eliminate the light-soaking effect.

### 5.1.3. The Stability Issue of OSCs in the ZnO-Involved Devices

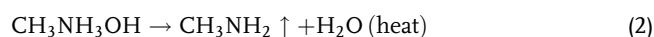
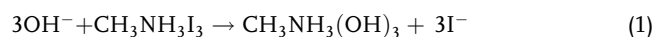
Recently, some works found the ZnO ETL affected the stability of OSCs, especially the nonfullerene solar cells. Jin et al.<sup>[66]</sup> found the air stability of the inverted solar cells significantly improved by treating the ZnO ETL with ethanedithiol (EDT). Typically, the unencapsulated P3HT:PC<sub>61</sub>BM devices remained 60% of the initial PCE after 30 days of storage in the air. However, after treating ZnO with EDT, the device performance could maintain at 70% of the initial value.

The high sensitivity of the nonfullerene OSCs solar cell to the ZnO ETL was ascribed to the photochemical reaction between ZnO and the nonfullerene acceptor. Due to the reaction, a new absorption band from 400 to 500 nm in the absorption spectra of IT-4 F was found when ZnO was deposited underneath the IT-4 F acceptor (shown in Figure 24a,c). It was ascribed to the destruction of intramolecular charge transfer between IDTT moiety and the EG-2 F moiety in IT-4 F. Similar photodegradation was also found in other similar nonfullerene acceptors, like ITIC and IEICO-4 F molecular. According to the mass spectrometry (MS) results, a possible disruption of the C=C linkage that links the donor (IDIT) and acceptor (EG-2 F) moieties was posed. Zhou et al. found that such a reaction was a typical photocatalytic effect of ZnO under UV spectra.<sup>[108]</sup> In contrast, as shown in Figure 24c,d, they did not find a reaction between SnO<sub>2</sub> and nonfullerene acceptor. Therefore, the nonfullerene OSCs with SnO<sub>2</sub> ETL showed improved stability. Liu et al.<sup>[109]</sup> further found that photodegradation by ZnO still occurred under the irradiation of white light. In addition, the UV–vis absorption showed these ZnO films contained different defect absorption bands, which would be the origin of the different degradation results (Figure 24e–h). The intensities of -OH groups outside the ZnO nanoparticles have resulted in the degradation of the IT-4 F acceptor. They ascribed this process as the following steps (as shown in Figure 24i): 1) light absorption of ZnO creates holes in the valence band and electrons in the conductive band; 2) the dangling OH is oxidized by the holes and generating reactive hydroxyl radicals; 3) decomposition of IT-4F molecular by hydroxyl radicals through decoupling reaction. Further, Han et al. (Figure 24j) solved this problem by surface-treating the ZnO films with acid solutions of 2-phenylethylmercaptan (PET). After acid solutions treatment, the amount of defect oxygen to the lattice oxygen decreased, which was ascribed to the

removal of surface -OH groups. And consequently, the operational stability of the PM6:Y6 inverted solar cells significantly improved to T<sub>80</sub> of 4000 h.<sup>[110]</sup> Li et al. found small molecule self-assembled monolayers could passivate the photocatalytic activities and improve stability.<sup>[111]</sup> Besides, Yip et al. used C<sub>60</sub> self-assembled layer to modify the ZnO buffer layer and achieved a lifetime of over 20 years for the nonfullerene acceptor-based OSCs.<sup>[112]</sup>

### 5.1.4. Stability Issue of the PVSCs in the ZnO-Involved Devices

The utilization of ZnO as a replacement for TiO<sub>2</sub> as low-temperature ETL has been sustainably studied, and the application has been expanded to flexible devices and roll-to-roll compatible fabrication without the limitation of high-temperature treatment. But there are still some intrinsic issues with the application of ZnO in PVSCs, especially the MAI-employed cells. First, chemical instability is a big problem as ZnO was used in the MAI-based PVSCs. In the ZnO-employed PVSCs, decomposition of the perovskite film to PbI<sub>2</sub> was found when heating the films at about 100 °C for a while, while such a phenomenon is not found between TiO<sub>2</sub> and the perovskite layer.<sup>[113]</sup> This could be mainly attributed to the different surface properties of ZnO and TiO<sub>2</sub>. The surface of TiO<sub>2</sub> is slightly acidic while the surface of ZnO exhibits basic behavior.<sup>[114]</sup> Once perovskite contacts with ZnO directly, a deprotonation reaction against methylammonium cation happens. Besides, the instability of the ZnO involved in PVSCs also originated from the chemical residues during the synthesis process. The residual hydroxyl groups and acetate would accelerate the decomposition of the perovskite layer. It was caused by the photon-transfer reactions of the ZnO/CH<sub>3</sub>NH<sub>3</sub>PbI<sub>3</sub> interface because of the basic nature of the ZnO surface.<sup>[114]</sup> Obviously, the reaction between hydroxide and MAI would cause decompose of the perovskite under annealing. Therefore, the thermal instability of the PVSCs with a ZnO ETL is a major challenge limiting the device performance. The process could be described as follows



ZnO would decompose the perovskite materials because of the photocatalysis activity of ZnO and the photochemical reaction between the surface hydroxyl groups and perovskite.<sup>[115]</sup> Qin et al.<sup>[116]</sup> replaced the conventional sol–gel precursor, ethanolamine with polyethyleneimine (Figure 25a). The XPS spectra showed the films derived from PEI precursor have fewer hydroxyl groups than the conventional films. In detail, the conventional ZnO films showed the ratio of lattice oxygen to O in hydroxide of 1:1, while the ratio of lattice O to hydroxide O increased to 2:1 for the PEI-based ZnO films. As a consequence, the MAPbI<sub>3</sub> on the conventional ZnO films quickly decomposed to yellow PbI<sub>2</sub>. In contrast, the PVSK films were more stable on top of ZnO films derived from PEI precursors (Figure 25b). Besides the solution method through precursor regulation, Yang et al.<sup>[117]</sup> also demonstrated a dynamic spin coating strategy could solve this problem. Different from the conventional route, the dynamic spin coating strategy meant dripping the perovskite

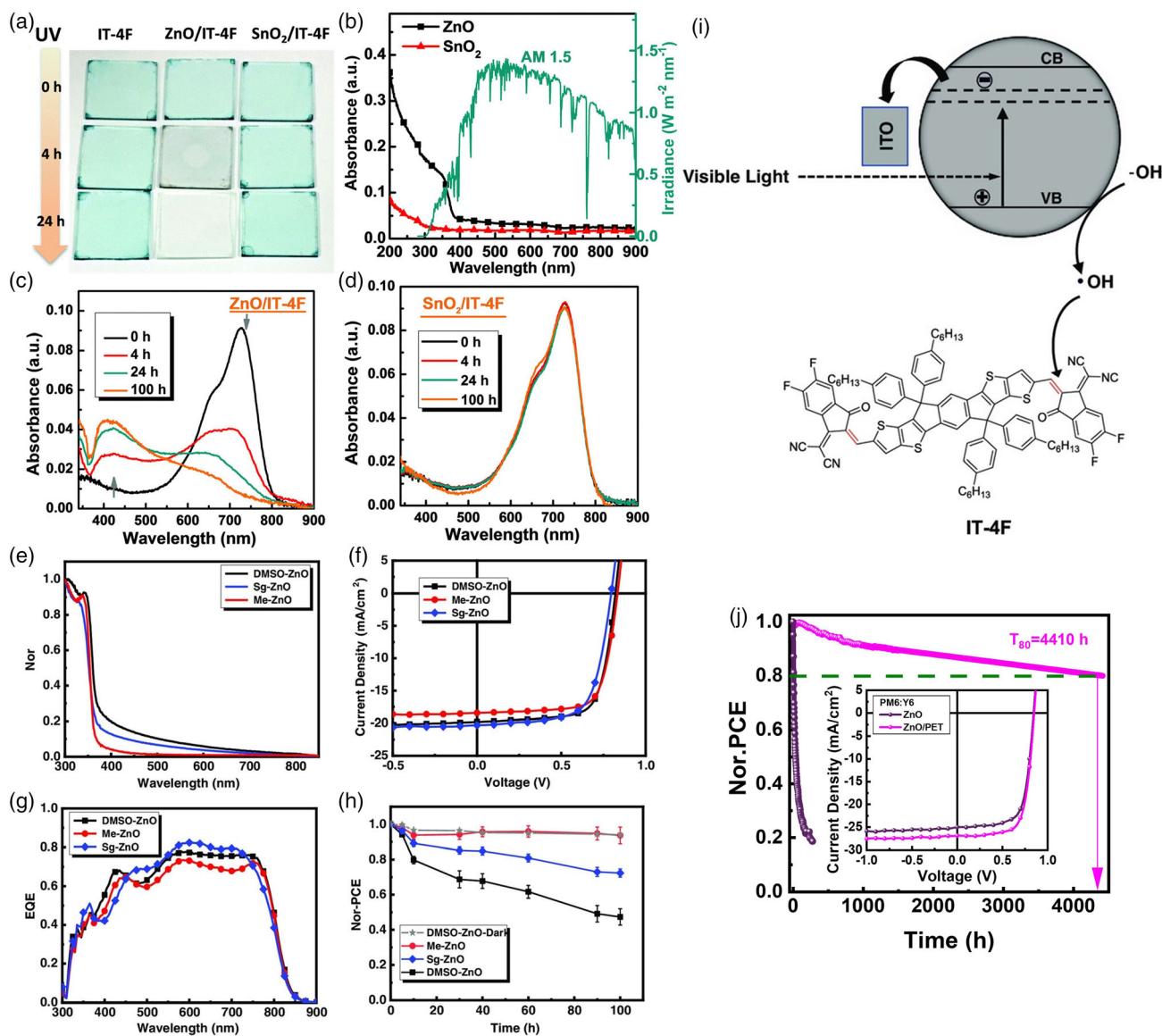


**Figure 24.** a) Photographs of the IT-4 F thin film on glass, glass/ZnO, and glass/SnO<sub>2</sub> substrates under UV illumination. b) The UV-vis absorption spectra of ZnO and SnO<sub>2</sub> films, and the AM1.5 spectra. c,d) Evolution of the absorption spectra of the c) ZnO/IT-4 F and d) SnO<sub>2</sub>/IT-4 F films at the AM1.5 solar irradiation. Reproduced with permission.<sup>[108]</sup> Copyright 2019, RSC. e) UV-vis absorption spectra of three different ZnO films. Reproduced with permission.<sup>[109]</sup> Copyright 2021, Wiley-VCH GmbH. f,g) J-V and (h) EQE spectra of PM6:IT-4 F with different ZnO layers. i) PCE decay curves of PM6:IT-4 F cells with different ZnO layers under white light illumination. j) PCE decay curves of PM6:IT-4 F cells with ZnO and ZnO/PET ETL. Reproduced with permission.<sup>[110]</sup> Copyright 2021, ACS.

precursor solution on ZnO during the spin coating process, followed by an antisolvent washing treatment.

Similarly, Facchetti et al.<sup>[118]</sup> developed a novel method to prepare ZnO ETL with less organic ligand and hydroxy group remaining through a low-temperature solution-processable route. The combustion synthesis process of ZnO (C-ZnO) involved mixing the Zn(NO<sub>3</sub>)<sub>2</sub>·6H<sub>2</sub>O, acetylacetone, and 2-methoxyethanol as the precursor, spin coating, and final thermal annealing. Compared with the acetate-derived sol-gel ZnO (asg-ZnO) and nitrate-derived sol-gel ZnO (nsg-ZnO) films, the C-ZnO films have higher crystallinity (X-ray diffraction (XRD) patterns of the films as shown in

**Figure 26).** The XPS spectra of these films showed film O 1s spectra have individual two components: M-O-M lattice species and surface metal hydroxide (M-OH) species. The C-ZnO films showed a highest M-O-M lattice content of 85.5% than that of the nsg-ZnO (80.0%) and asg-ZnO films (71.4%), suggesting the C-ZnO films would have greater chemical purity, reduced charge traps, and superior electrical properties. Defecting from the improved crystallinity, the C-ZnO ETL exhibited higher conductivity ( $3.03 \times 10^{-4} \text{ S cm}^{-1}$ ) than the asg-ZnO ( $0.97 \times 10^{-4} \text{ S cm}^{-1}$ ) and nsg-ZnO films ( $1.39 \times 10^{-4} \text{ S cm}^{-1}$ ). They fabricated perovskite films of different compositions, i.e.,

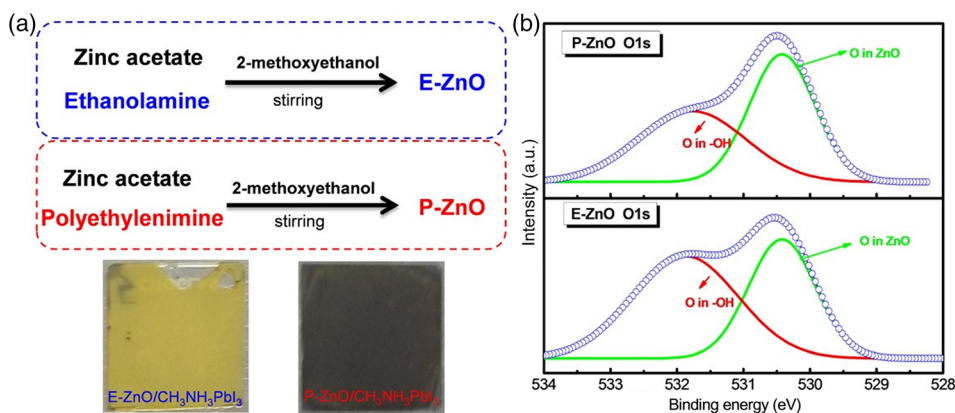


**Figure 25.** a) The photographs of the PVSK films on different ZnO films. b) The XPS spectra of the ZnO films derived from different precursors, E-ZnO and P-ZnO stood films from ethanolamine and polyethylenimine. Reproduced with permission.<sup>[116]</sup> Copyright 2017, ACS.

P1 (MAPbI<sub>3</sub>), P2 (Cs<sub>0.05</sub>FA<sub>0.81</sub>MA<sub>0.14</sub>PbI<sub>2.55</sub>Br<sub>0.45</sub>), and P3 (Cs<sub>0.1</sub>FA<sub>0.9</sub>PbI<sub>3</sub>) on the top of these ZnO films. Though the perovskite films on these different ZnO films exhibited typical crystalline perovskite morphologies, on top of the C-ZnO films, the grain sizes significantly increased for these three kinds of perovskite films. In addition, for the MAPbI<sub>3</sub> films on the top of nsg-ZnO and asg-ZnO films, a typical yellow phase ascribed to PbI<sub>2</sub> was observed from the XRD patterns, which led to a poor device efficiency with PCE of 1.98% and 7.23%. With the C-ZnO ETL, the MAPbI<sub>3</sub> devices performed an efficiency of 17.14% with a  $V_{OC} = 1.00$  V and  $J_{SC} = 23.03$  mA cm<sup>-2</sup>. That was because the elimination of surface hydroxyl groups and oxygen vacancies in C-ZnO films suppressed the degradation of the MAPbI<sub>3</sub> films and improved the quality of the film. The Cs<sub>0.05</sub>FA<sub>0.81</sub>MA<sub>0.14</sub>PbI<sub>2.55</sub>Br<sub>0.45</sub> and Cs<sub>0.1</sub>FA<sub>0.9</sub>PbI<sub>3</sub> cells showed an optimized performance of 18.82% and 19.84%, respectively. Besides, the C-ZnO ETLs involved in PVSCs also showed significantly promising performance. The use of C-ZnO ETL improved the air stability of the PVSCs. During thermal annealing at 85 °C with a controlled humidity of 25%, the Cs<sub>0.1</sub>FA<sub>0.9</sub>PbI<sub>3</sub> cells could retain 95% of the initial PCE after 100 h operation, while the nsg-ZnO and asg-ZnO cells remained about 70% and 30% of the initial PCE.

Overall, the instability was proved to be from the reaction between ZnO and MAI ions by several groups. For example, Snaith et al.<sup>[119]</sup> proved the degradation mechanisms at the perovskite-ZnO interface utilizing an amine indicator, and they found the instability could be ascribed to the deprotonation of the methylammonium cation. Thus, by substituting MAI with formamidine (FAI) and cesium (Cs), the device stability of ZnO-perovskite interface was comparable to the SnO<sub>2</sub>-based devices after high-intensity UV irradiation and 85 °C thermal stressing. Although there was a stability issue for the utilization of ZnO in the PVSCs, Bai et al.<sup>[120]</sup> found an interesting advantage of room temperature crystallization as the perovskite layer is deposited on the top of ZnO ETLs. TiO<sub>x</sub>, SnO<sub>2</sub> ETLs were used for comparison. The absorption spectra showed no absorption from the crystallized perovskite was detected without annealing. However, in the case of ZnO films, two obvious emission peaks at 718 and 780 nm from the intermediate phase and crystallized MAPbI<sub>3</sub> perovskite were observed. The different crystallization process for the ZnO-involved films has been attributed to the

decrease of activation energy due to the residual acetate ligands of ZnO.

## 5.2. Influence of Films Quality of ZnO on the Photovoltaic Performance

### 5.2.1. Influence of Morphology of ZnO on Device Performance

Generally speaking, the thickness, surface roughness, surface composite, and morphology of ZnO ETL all have a great impact on the inverted and conventional structure OSCs. As we know, the morphology of the ZnO ETL was decided by the precursor solution or the nanoinks, and the posttreatment methods. Ma et al.<sup>[121]</sup> found that the surface roughness of the sol-gel ZnO layer greatly influenced the device FF and the overall performance. The PCE of the TQ1:PC<sub>71</sub>BM solar cells increased from 2.7% to 3.9% when the root-mean-square roughness of the ZnO buffer layer decreased from 4.9 to 1.9 nm. For a rough ZnO layer, high interface trap density should be the main reason for the poor device performance. Similarly, the roughness of the ZnO ETL fabricated from ZnO colloidal route also greatly influenced the device performance because of inferior interface contact between ZnO and the photoactive layer.<sup>[122]</sup> On this basis, the ZnO nanoparticles should have a small size and be well dispersed in the solvent. Otherwise, the large size or agglomeration would cause a rough surface of the ZnO ETLs, and lead to poor interface contact. Cao et al. showed the ZnO nanoparticle films from different concentrations have different surface quality (Figure 27a-f). The device performance was more sensitive to the surface quality of ZnO and less dependent on the thickness. The use of thin, dense, and homogenous ZnO films would lead to enhancement of FF and short-circuit current (Figure 27g,h). Furthermore, Ji et al. found the surface roughness of the ZnO ETL impacted the device performance and stability of the OSCs more greatly for the doctor-blade device than the spin coating devices, even using the same ZnO ETL. A smoother ZnO ETL would enable higher device performance and much longer lifetime for the doctor-blade-coated OSCs.<sup>[123]</sup> As shown in Figure 27i, two kinds of ZnO ETLs, a rough (A-ZnO) and a smooth film (M-ZnO), were used in the spin-coated and doctor-bladed solar cells. Figure 27j shows the spin-coated solar

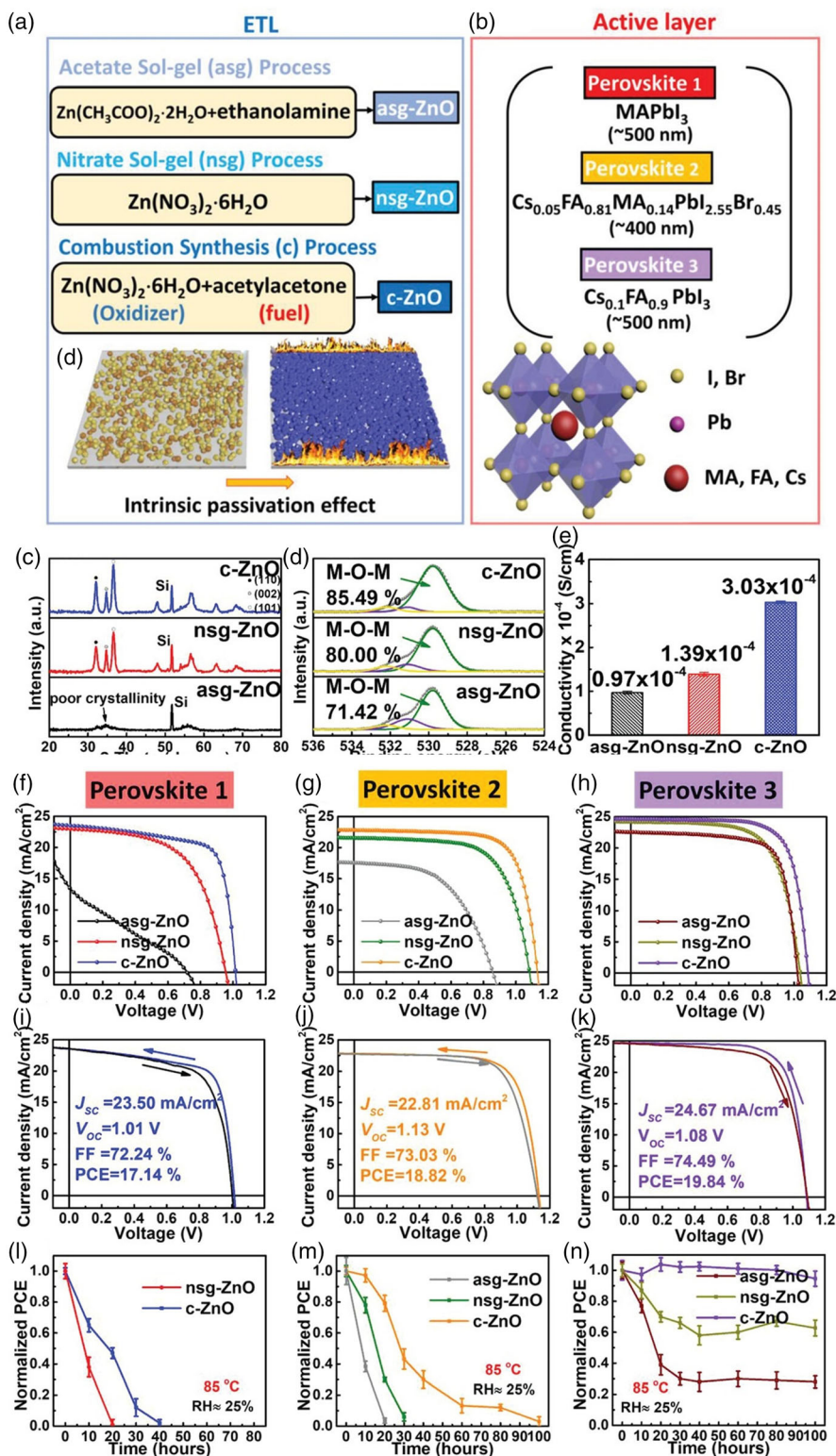


**Figure 26.** a) The synthesis process of the solution-processed ZnO ETL and b) composition of the perovskite layers. c–e) XRD, XPS, the conductivity of these ZnO films. f–h)  $J$ – $V$  characteristics of PVSCs with different ZnO ETLs. i–k)  $J$ – $V$  characteristics of the PVSCs through forward and afterward scan. l–n) Normalized PCE of PVSCs during annealing at 85 °C and 25% humidity. Reproduced with permission.<sup>[118]</sup> Copyright 2019, Wiley-VCH GmbH.

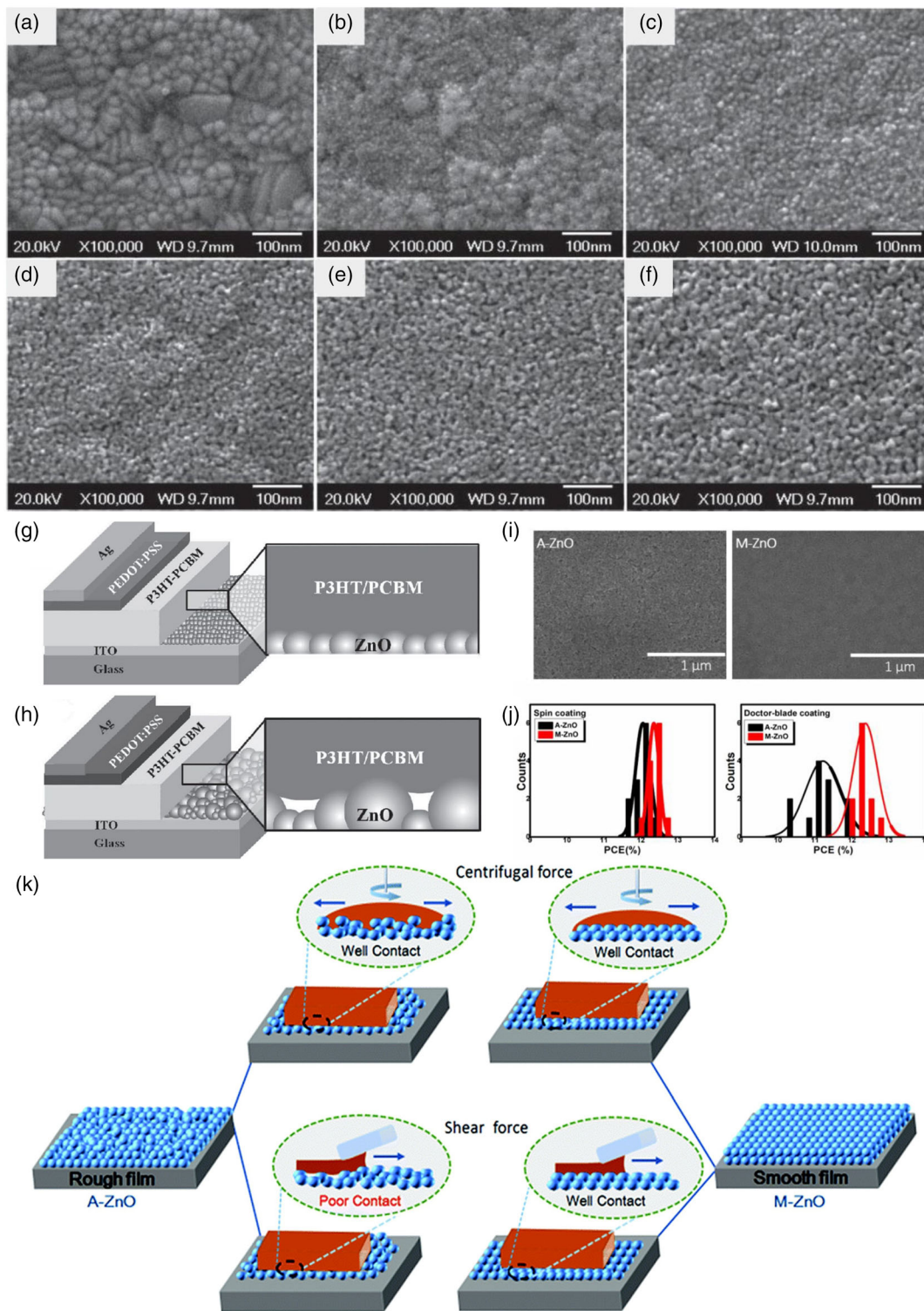


**Figure 27.** SEM images of the ZnO films derived from different sol concentrations: a) 0.02, b) 0.05, c) 0.1, d) 0.3, e) 0.6, and f) 1 M. g,h) Device structure of the P3HT:PCBM/ZnO interface conditions with ZnO layer derived from 0.1 M and 1 M sol. i) The SEM image of the ZnO films fabricated from methanol and acetone-based ZnO inks. j) The performance histogram of the spin-coated and doctor-blade-coated solar cells with different methanol and acetone-based ZnO buffer layers. k) The schematic diagram of spin-coated and doctor-blade-coated solar cells with methanol and acetone-based ZnO buffer layer. Reproduced with permission.<sup>[123,227]</sup> Copyright 2012, Wiley-VCH GmbH, and 2019, RSC.

cells gave better performance than the doctor-bladed solar cells. In addition, the doctor-bladed solar cells with rough ZnO ETL showed a much larger performance deviation than the devices with the smooth buffer layer. This result has been ascribed to the worse surface contact between the ZnO ETL and the active layer in the case of doctor-blade coating because of the much weaker spread force during doctor-blade. The detailed mechanism is shown in Figure 27k.

### 5.2.2. The Thickness-Related Optical Effect in OSCs

ZnO could be used as ETL in conventional and inverted OSCs, and the influence of ZnO thickness on the performance is caused by both electrical and optical factors. On the side of the electrical factor, most of the attention was paid to the electron mobility or conductivity properties of the ZnO layer. Although the pristine ZnO generally has a high electron mobility of about  $10^{-3} \text{ cm}^2 \text{ V}^{-1} \text{ S}^{-1}$ , such conductivity of the pristine ZnO is not high enough to satisfy long-distance charge transporting. Therefore, as a thick ZnO layer was used in the inverted organic solar cell, the device performance, both  $J_{SC}$  and FF, would dramatically decrease relative to the thin ZnO devices. For the pristine sol-gel ZnO buffer layer, the thickness should be controlled below or around 30 nm. Otherwise, the device performance decreased gradually with the increase of ZnO thicknesses.<sup>[124]</sup> The ZnO nanoparticle-based ETL seems to have a higher working thickness than the sol-gel ZnO layer. However, the thickness of the ZnO nanoparticles ETL also should be strictly controlled. Generally, in the P3HT:PC<sub>61</sub>BM solar cells, the thickness should be restricted to 100 nm. But for most of the active layer systems,

the thickness of the ZnO nanoparticles layer was controlled at around 30 nm. The low working thickness of the ZnO ETLs mainly originated from a variety of defects. In particular, the solution-processed ZnO layer contains more defects than the films fabricated from the vacuum deposition route. Several works reported increasing the working thickness of ZnO in thin film photovoltaics through ion doping or organic molecular modification. Ion doping can increase the carrier concentration and improve charge mobility. Organic molecular modifying the ZnO layer can effectively decrease defects concentration and increase charge mobility.

The influence of the ZnO ETLs on the photovoltaic performance from the optical factor means the thickness of the ZnO layer would impact the space optical distribution in the devices, and consequently influence the device performance. Such an effect mainly occurred in the OSCs with the conventional structure, where the ZnO layer was deposited on top of the organic active layer. It was also reported that the insertion of a ZnO layer would act as an optical spacer to enhance the light absorption of the device in the conventional structured OSCs compared with the device with ZnO ETL.<sup>[38]</sup> Heeger et al. inserted a ZnO nanoparticle optical space layer on the top of a small molecular active layer in conventional OSCs. The use of ZnO improved the light harvesting and also served as a hole-blocking layer, which led to the increase of  $J_{SC}$  and FF, respectively.<sup>[38]</sup> Figure 28a shows the AFM images of the ZnO NPs on the top of the small-molecular photoactive layer and the device structure. Figure 28b shows the insertion of ZnO NPs improved the performance. In that work, the optimized thickness of the ZnO optical space layer is around 25 nm. But the space optical effect of ZnO is highly related to the

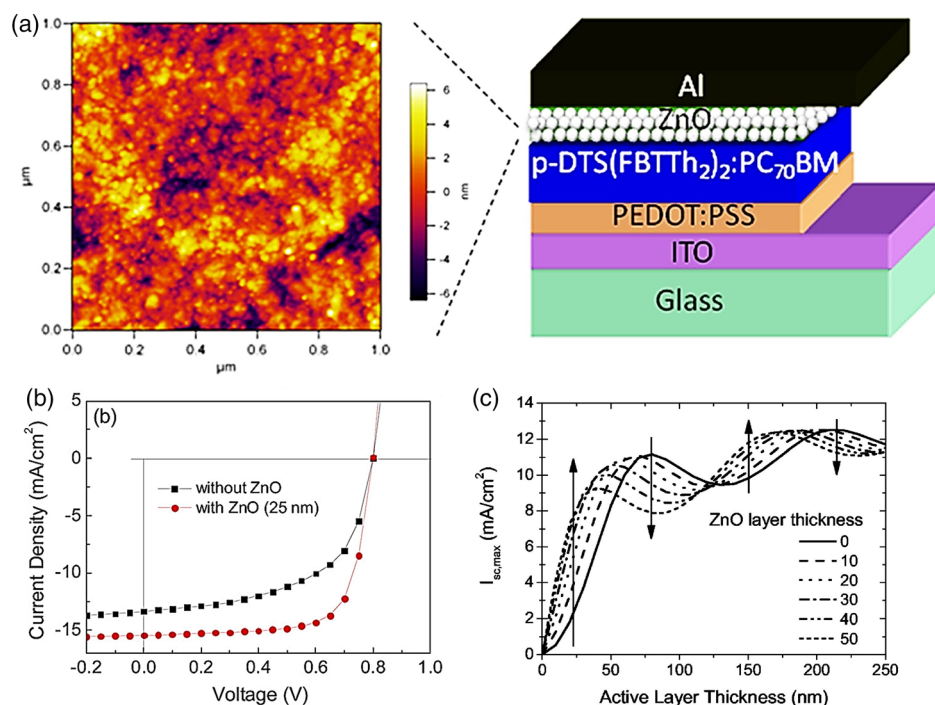


**Figure 28.** a) AFM image of the ZnO nanoparticles, and the device structure of the conventional structure OSCs with the ZnO optical space layer, b)  $J$ - $V$  characteristics of the OSCs with and w/o the ZnO optical space layer. c) The active layer thicknesses-dependent short circuit current for the OSCs with different thicknesses of the ZnO layer. Reproduced with permission.<sup>[55]</sup> Copyright 2007, IOP.

thicknesses of other functional layers in the cells. For the P3TH:PCBM devices with a thin active layer, the photocurrent would increase by using the ZnO space light layer (Figure 28c). But for the cells with a thick photoactive layer, the effect of the optical spacer is less pronounced.<sup>[55]</sup> On the side of the inverted OSCs, the thickness of the ZnO layer still influenced the device performance because the introduction of ZnO would change the optical transmission of the transparent electrode.<sup>[125]</sup>

## 6. The Modification of ZnO ETLs for OSCs and PVSCs

The modification of ZnO ETL is an important research project in OSCs with the aiming to improve the charge transport properties, lower the performance-thicknesses dependence, and improve the water and oxygen sensitivity of the devices. The modification approach could be divided into the following three factors: 1) using the stack structured electron buffer layer, 2) using a ZnO-based hybrid electron buffer layer, and 3) using solvent surface treatment.

### 6.1. Surface Modification of Solution-Processed ZnO Buffer Layer for OSCs and PVSCs

A stack-structured ETL composites a ZnO layer and a polymer or small molecular extra layer. For instance, Polyethylenimine (PEI), polyethylenimine ethoxylated (PEIE),<sup>[126]</sup> alt-(2,7)-(9,9-dioctyl)-" with "alt-2,7-(9,9-dioctyl)-"9 (PFN),<sup>[127]</sup> phosphoric acids self-assembling monolayer (SAM) layer,<sup>[128]</sup> and atomic layer-deposited ZnO layer<sup>[129]</sup> have been developed. By inserting an extra organic layer on top of the ZnO layer, the interface charge selectivity was enhanced, and thus the device FF increased a lot in all these cases. Besides, treating the ZnO layer with self-assembled small organic molecule (e.g., C<sub>60</sub> derivatives<sup>[130,131]</sup> and silane)<sup>[132]</sup> is another successful way, which can passivate the surface defects of ZnO or improve the interface contact between the buffer layer and the active layer. Bai et al. used ethanedithiol (EDT)-treated ZnO layer to improve the surface defects by forming zinc ethanedithiol. It is noteworthy that by using the hydrophobic EDT treatment of ZnO, the influence of moisture was lessened, thereby leading to significantly improved the long-term stability in air (Figure 29a).<sup>[66]</sup> Similarly, Fu et al.<sup>[132]</sup> covered an APTMS layer on the top of ZnO. APTMS passivated the ZnO surface defects and decreased the surface work function of ZnO. In addition, APTMS can bond to the fullerene derivative, thereby reducing the interface contact resistance (as shown in Figure 29b) and improving the PCE from 8.47% and 9.46% for the PTB7-Th:PCBM heterojunction solar cells. In addition, self-assembly molecular layers (SAMs) were used to treat the ZnO films. As shown in Figure 29c, Kim et al.<sup>[133]</sup> used a series of benzoic acid derivatives, 4-fluorobenzoic acid (FBA), 4-tert-butylbenzoic acid (BBA), and 4-methoxybenzoic acid (MBA) to modify the ZnO ETL. The work function of ZnO depended on the orientation of the dipole moment of the SAM molecules. Among MBA, BBA, and FBA, the dipole orientation of FBA and BBA was in exactly opposite directions. In contrast, the dipole orientation of FB is directed toward ZnO. For the MBA and BBA, the work function of ZnO/FBA increased from

4.17 ± 0.01 eV of the pristine ZnO ETL to 4.31 ± 0.04 eV. The work function of ZnO/BBA and ZnO/MBA dreading to 3.97 ± 0.01 and 3.94 ± 0.04 eV. Thus, the PCE of the P3HT:PCBM solar cells using MBA and BBA treated ZnO reached 3.34% and 2.94%. But FBA-treated ZnO ETL gave a relative lower device performance of 1.81%. Similarly, the work function of the ZnO ETL was well regulated by phosphonic acid interlayer. Olson et al.<sup>[134]</sup> reported the work function of ZnO was not entirely orientation dependent; the dipole strength and molecules direction would impact as well. For instance, for the phosphonic acid molecules, Pcf3BPA and pFBPA, the orientation of polarizing fluorine molecule on the benzene ring influenced the molecular dipole (Figure 29d).

As mentioned above, there is a serious thermal instability issue in the ZnO-based PVSCs. It has been mainly attributed to the proton transfer reaction between the perovskite layer and ZnO, so surface modification of the ZnO ETL is significantly important. The modification methods include doping of metal oxides and surface modification with an interlayer. As a typical example of the former method, Chen et al. used the SAM to modify the sol-gel ZnO surface with the 3-aminopropanoic acid SAM layer. The introduction of this layer induced the improvement of morphology and crystallization of the perovskite layer,<sup>[135]</sup> and improved the device performance from 11.96% to 15.67% (Figure 30a). Recently, a thin layer of MgO and a submonolayer of protonated ethanolamine (EA) were deposited on the ZnO layer to enhance the electron transfer and stability of the ZnO/PVSK interface. Finally, hysteresis-free and stable PVSCs were achieved.<sup>[136]</sup> As shown in Figure 30b, the interface of ZnO and perovskite was mediated by a thin layer of MgO-EA<sup>+</sup> (EA<sup>+</sup> = OCH<sub>3</sub>CH<sub>2</sub>NH<sup>3+</sup>), which played several roles: 1) inhibited the interface charge recombination and enhanced cell performance because of the introduction of MgO; 2) enhanced electron transport from perovskite to ZnO and helped to eliminate hysteresis because of the protonate EA; 3) improved the device stability. The EDS images, XRD patterns, and Fourier-transform infrared spectroscopy spectra of the ZnO-MgO-EA<sup>+</sup> samples proved its formation. With the Mg-EA<sup>+</sup>-modified ZnO ETL, the performance of the PVSCs improved from 15.1% to 18.3%, and no hysteresis was observed. For the average efficiency of 30 cells, the ZnO-MgO-EA<sup>+</sup> device gave average efficiency of 17.2% ± 1.2% for the reverse scan (RS) and 17.1% ± 1.3% for the forward scan (FS). However, the ZnO-based device showed a 13.8% ± 1.2% average efficiency for RS and 12.9 ± 1.3% for FS. The modification of ZnO by MgO-EA<sup>+</sup> also improved the stability of the devices, which retained over 60% of their original efficiency after 4 h. Similarly, An et al. modified the ZnO layer by a combination of doping and surface modification, where Li and Cs were used to doping the ZnO, and the PCBA was deposited on the surface of the ZnO layer.<sup>[137]</sup> The Al-doped ZnO (ZnO:Al) showed big potential in improving the device stability relative to the pristine ZnO-based cells. That was because the use of ZnO:Al could eliminate the Lewis acid-based chemical reaction between perovskite and ZnO.<sup>[138]</sup> The doping of ZnO could weaken the basic property, diminish the chemical reaction of perovskite and ZnO, and consequently improve the thermal stability of devices. Yao et al. grafted the fullerenes onto ZnO nanoparticles by binding catechol on ZnO. Through modifying with fullerene, ZnO could penetrate the perovskite film to form

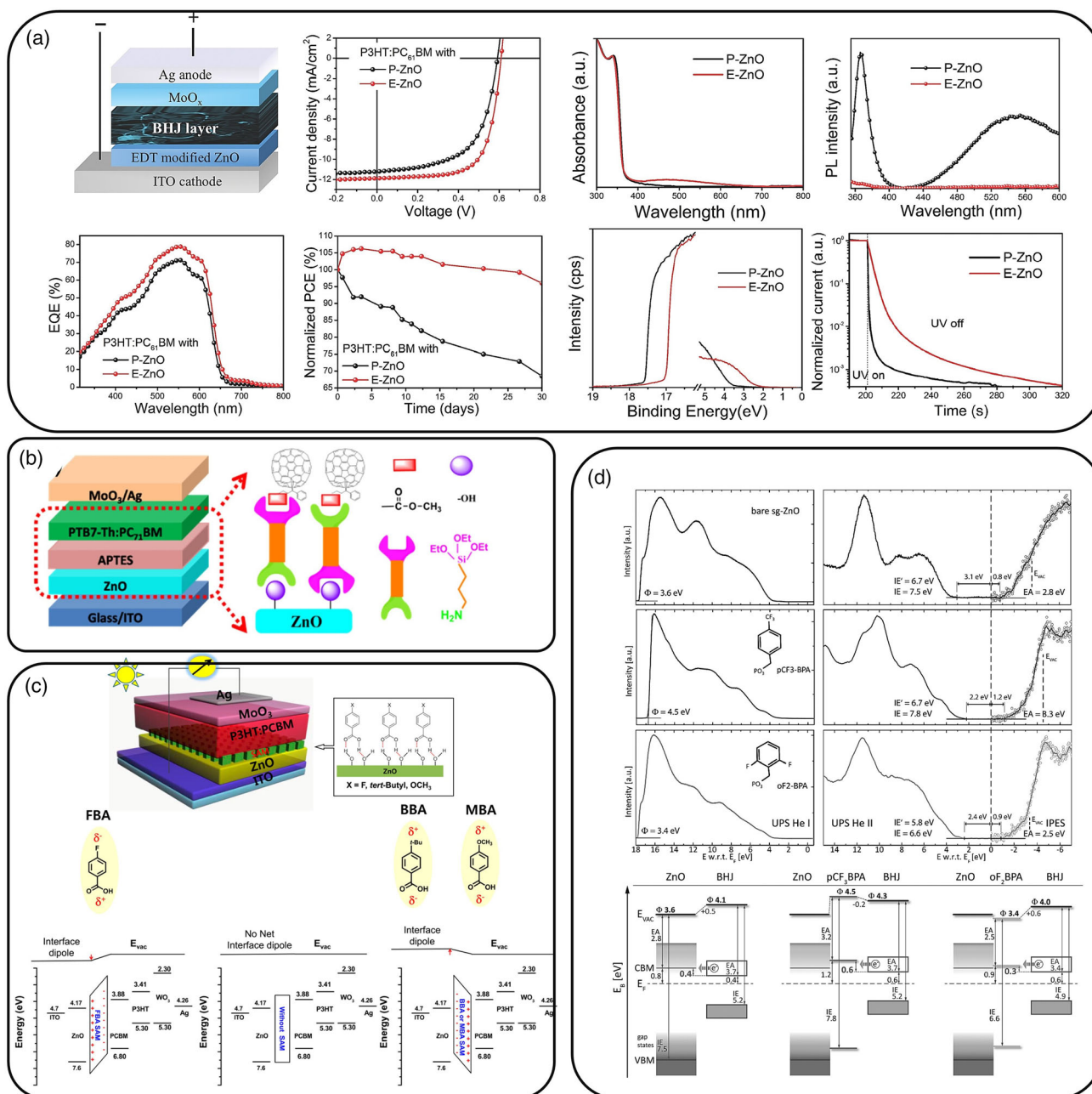


**Figure 29.** a) EDT-modified ZnO layer for use in OSCs: device structure,  $J$ - $V$  characteristics of the  $P$ -ZnO- and  $E$ -ZnO-based solar cells, EQE spectra of the devices, the evolution of PCE of the device with  $P$ -ZnO and  $E$ -ZnO ETLs. Reproduced with permission.<sup>[66]</sup> Copyright 2015, Wiley-VCH GmbH. b) APTMS-modified ZnO for use in OSCs: the device structure and the schematic of bonding between ZnO and PCBM. Reproduced with permission.<sup>[132]</sup> Copyright 2017, ACS. c) FBA, BBA, and MBA SAM-modified ZnO ETL for the inverted OSCs. Reproduced with permission.<sup>[133]</sup> Copyright 2013, ACS. (d) UPS and inverse photoemission spectra (IPES) of the bare ZnO films, and the  $p$ CF<sub>3</sub>-BPA,  $o$ F<sub>2</sub>-BPA modified ZnO films. Reproduced with permission.<sup>[134]</sup> Copyright 2014, Wiley-VCH GmbH.

heterojunction cells.<sup>[139]</sup> Obviously, no chemical reaction existed between the fullerene-capped ZnO and perovskite. These works demonstrated that doping or surface modification played an effective role in improving the stability of the cell.

Ismail et al.<sup>[140]</sup> developed a kind of 2,3,4,5,6-pentafluorobenzoyl chloride (PFBC)-capped ZnO nanoparticles (ZnO@PFBC) through

two-step synthesis as shown in **Figure 31**. ZnO@PFBC was used in the  $p$ - $i$ - $n$  planar PVSCs as a modifier of PCBM by spin coating it on the top of the PCBM layer. A good energy level aligns and good deposition was found as shown by the energy level and the SEM image. The device performance improved from 15.33% to 16.93%. Because of the physical protection of ZnO@PFBC, both the

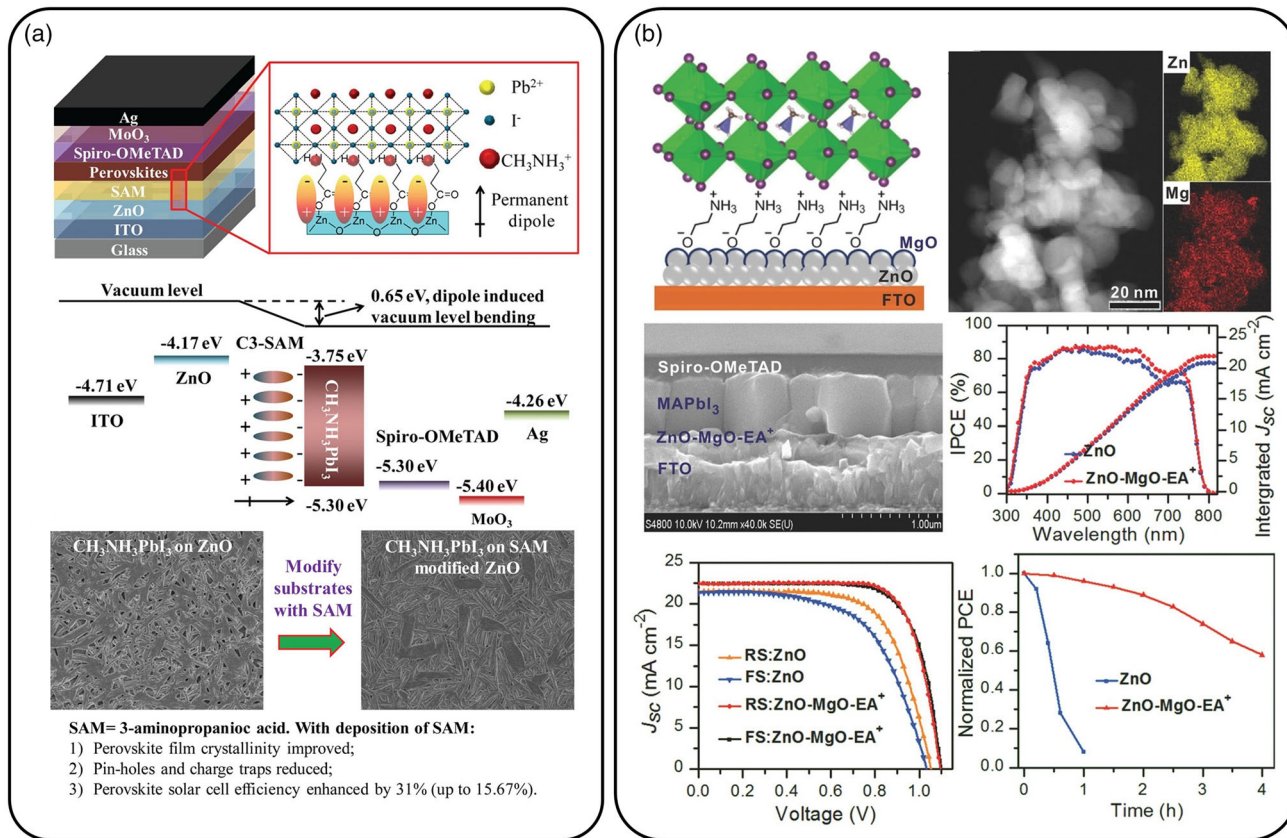


**Figure 30.** a) C3-SAM-modified ZnO for use in the PVSC. Reproduced with permission.<sup>[228]</sup> Copyright 2017, ACS. b) Schematic of the PVSCs with ZnO-MgO-EA<sup>+</sup>, high angle angular dark field-scanning transmission electron microscopy image and elemental mapping of the ZnO-MgO-EA<sup>+</sup> samples, XRD patterns of the precursor sample annealed under different temperature. TPD-MS and IR spectra of the ZnO-MgO-EA<sup>+</sup> annealed at 450 °C for 39 min. Reproduced with permission.<sup>[136]</sup> Copyright 2019, Wiley-VCH GmbH.

migration of halogen and zinc was suppressed, leading to improved long-term stability under continuous illumination and thermal annealing. Meanwhile, the surface hydroxyl groups of ZnO NPs were capped by PFBC, and the chemical reaction between ZnO and PVS was successfully suppressed. The device remained at 75% of the original efficiency after thermal annealing at 85 °C for 200 h, while both the device w/o the modifier layer and the one with a ZnO modifying layer degraded quickly and nearly could not work after 30 h annealing. During long-term continuous illumination, the ZnO@PFBC-involved device kept 60% of the initial efficiency after 1100 h degradation.

## 6.2. Hybrid Modification of the ZnO Buffer Layer for OSCs and PVSCs

ZnO-based hybrid ETL was reported as an effective ETL in OSCs, which possessed the advantages of easy fabrication, good film-forming ability, and fewer thin film defects. First, several polymers could be composited with ZnO to improve the film morphology. Barth et al. reported the use of ZnO:PVP composite in OSCs. By using this ZnO-PVP nanocomposite ETL, high device performance was achieved without post-UV illumination, whereas such a post-UV treatment was necessary for the device using bare ZnO as the ETL to remove the “S-shape” kink.

Another example is ZnO–poly(ethylene oxide) (PEO) composite. By using ZnO–PEO nanocomposite, the charge carrier recombination rate was decreased in solar cells, and the short-circuit current ( $J_{SC}$ ) and FF were considerably improved consequently.<sup>[141]</sup> Xie et al. reported an excellent ZnO-based nanocomposite incorporating phosphonate-functionalized polyfluorene (PFEP) for use as the ETL in OSCs. High device performance and less layer thickness sensitivity were found for ZnO–PFEP-based solar cells.<sup>[142]</sup> Wu et al. found the use of a ZnO:PFN composite electron buffer layer could improve device performance and stability, and lower the thickness sensitivity. No obvious thickness-dependent performance was found, even when the thickness of this layer increases to 125 nm.<sup>[65]</sup> ZnO:PEI composite electron buffer layer was used for roll-to-roll printed OSCs due to its low thickness sensitivity, and the low cost of PEI in comparison to other conjugated polymer molecules.<sup>[143]</sup> Xie et al. developed several photoconductive small molecular compounds to modify the ZnO electron buffer layers.<sup>[124,144–147]</sup> These compounds could be mixed with ZnO sol–gel precursor and formed a composite buffer layer. Within the composite films, charge transport from these photoconductive molecules to ZnO has significantly improved the conductivity and electron mobility and led to the improvement of device performance.<sup>[145]</sup> In addition, the working thickness of modified ZnO could increase largely.

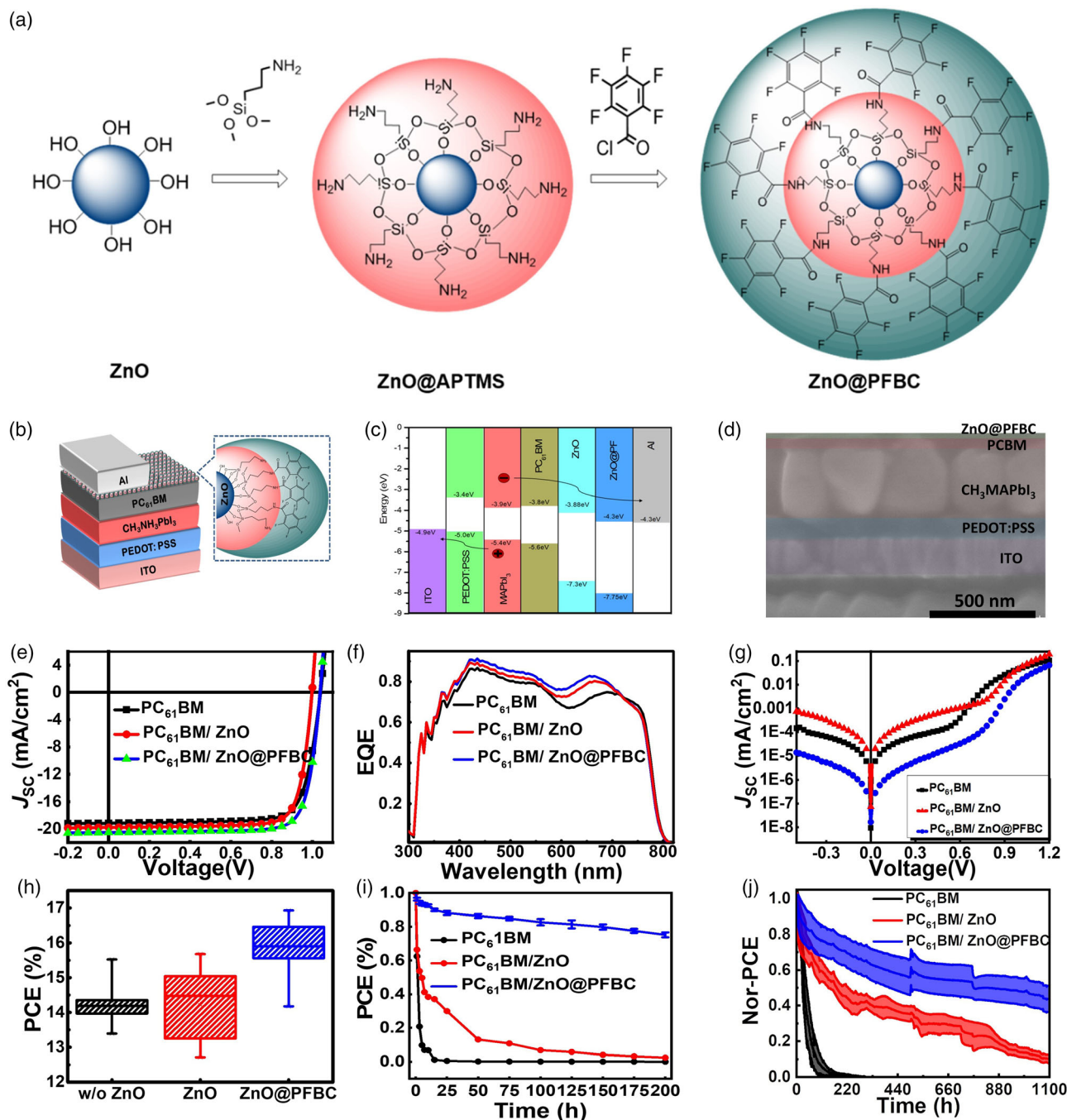


**Figure 31.** a) The schematic diagram of the PFBC-capped ZnO nanoparticles, b) the device structure of the PVSCs, c) the energy level, and d) the cross-sectional SEM image of the devices. e)  $J$ - $V$  characteristics and f) EQE spectra of the device, g) dark  $J$ - $V$  curves. h) Histogram of the performance with different ETLs. i) Evolution of PCE of the PVSCs with different ETLs during annealing at 85 °C for 200 h in the N<sub>2</sub>-filled glove box, j) and the evolution of PCE during continuous illumination in the N<sub>2</sub>-filled glove box at around 40 °C. Reproduced with permission.<sup>[140]</sup> Copyright 2020, Wiley-VCH GmbH.

As an example, as the thickness of PBI-Py-modified ZnO (ZnO@PBI-Py) increased to 300 nm, the device performance was nearly the same as the device with 30 nm ZnO:PBI-Py, while the working thickness of pristine ZnO was only around 30 nm.<sup>[124]</sup> Figure 32a shows the molecular structure of PBI-Py, the charge transport mechanism between PBI-Py and

ZnO,  $J$ - $V$  and EQE curves of the solar cells with the pristine ZnO and ZnO:PBI-Py ETLs. As shown in Figure 32b, the excited electrons of PBI-Py transferred to the excited state of ZnO upon being excited by UV light, resulting in increased conductivity and mobility. With FBT-Th<sub>4</sub>:PC<sub>71</sub>BM as the active layer, the device performance with ZnO:PBI-Py ETLs was higher than the device

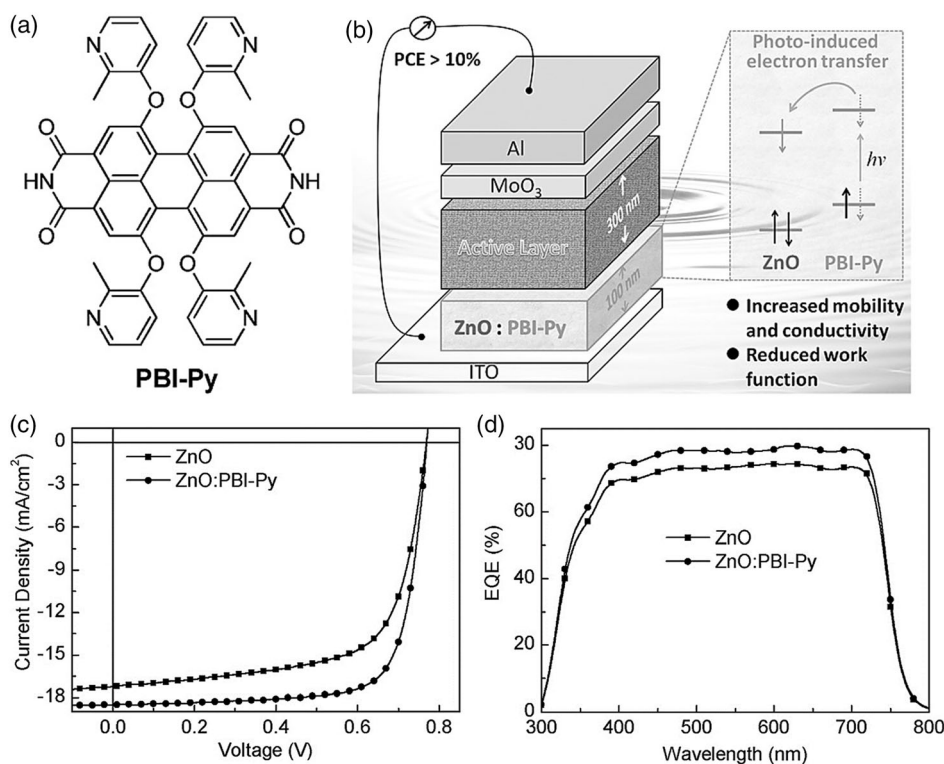


**Figure 32.** a) Chemical structure of PBI-Py. b) Device configuration, schematic illustration of the working mechanism for the photoconductive cathode interlayer. c)  $J$ - $V$  characteristics of OSCs and d) EQE spectra with ZnO and ZnO:PBI-Py buffer layer. Reproduced with permission.<sup>[124]</sup> Copyright 2016, Wiley-VCH GmbH.

with ZnO ETLs. Besides, some small molecules could be used to replace the surface ligands thereby lessening surface defects. 1,2-Ethanedithiol (EDT)-doped ZnO composite was prepared by a facile sol-gel method, and the strong interaction between ZnO and -SH group enables the formation of more homogenous composite films. Because of the strong surface interaction, the surface defects of ZnO were passivated and the electron mobility of ZnO increased, which lead to enhanced device performance.<sup>[148]</sup> For the inverted OSCs, the performance and device stability were improved by modifying the sol-gel ZnO using cetyltrimethylammonium-bromide (CTAB). It was reported that the oxygen vacancies of the ZnO layer could be occupied by bromide ions ( $\text{Br}^-$ ), thereby the incorporation of CTAB regulated the work function of the ZnO ETL, and dramatically influenced the optical, electrical, and morphologies properties of the ZnO films.<sup>[149]</sup> Chen et al. synthesized polydopamine-modified Al-doped ZnO buffer layer to reduce the thickness-insensitive of performance. Results showed the 80 nm-thick buffer layers could yield a PCE of 12.7% for the nonfullerene OSCs.<sup>[150]</sup> Zhou et al. found the PEI-Zn composite films fabricated through the sol-gel route have improved mechanical robustness and suppressed the chemical reaction between PEI and the nonfullerene active layer. The PEI-Zn worked efficiently as the interfacial layer in the flexible OSCs, giving an efficiency of 12.3% and 15% PCE with PEDOT:PSS and Ag nanowire as the electrode. In addition, the use of the PEI-Zn interfacial layer made the flexible OSCs giving excellent mechanical durability.<sup>[151]</sup>

In the inverted OSCs, the electron and hole are collected by the cathode and anode, respectively. So, enrichment of the acceptor and donor at the cathode and anode interface in the D:A phase separation would greatly enable charge collection. To achieve this, the ZnO buffer layer was modified by some electron acceptors, such as fullerene. One effective method is depositing fullerene on the top of the ZnO cathode buffer layer, and another method is doping ZnO ETL with a fullerene derivative. Fullerene derivative (PCBE-OH),<sup>[57]</sup> bis  $\text{C}_{60}$ , and  $\text{C}_{60}$ -nanofilms were incorporated into ZnO to enhance the electron collection by improving the contacts with the fullerene acceptor on the active layer surface.<sup>[152]</sup> Besides, fullerene, graphene, and carbon quantum dots<sup>[153]</sup> were introduced to modify the ZnO buffer layer through doping.

In addition, some composite materials based on two kinds of metal oxides were developed for the organic and PVSCs. Li et al. designed core-shell ZnO@SnO<sub>2</sub> nanoparticles through the solvothermal method. The synthesis diagram of the core-shell ZnO@SnO<sub>2</sub> nanoparticle is shown in Figure 33a. These hybrid materials showed 8.1 nm ZnO and a 3.4 nm-thick SnO<sub>2</sub>. This material has combined the advantages of a good energy match of SnO<sub>2</sub> with the perovskite layer, and the high electron mobility of the core ZnO nanoparticles. The perovskite ( $\text{CsPbI}_2\text{Br}$ ) solar cells with the structure of FTO/ZnO@SnO<sub>2</sub>/perovskite/spiro-OMeTAD/MoO<sub>3</sub>/Ag (Figure 33b) showed the highest PCE of 14.35% with  $J_{\text{SC}}$  of 16.45  $\text{mA cm}^{-2}$ ,  $V_{\text{OC}}$  of 1.11 V, and FF of 79%. As a comparison, the device with

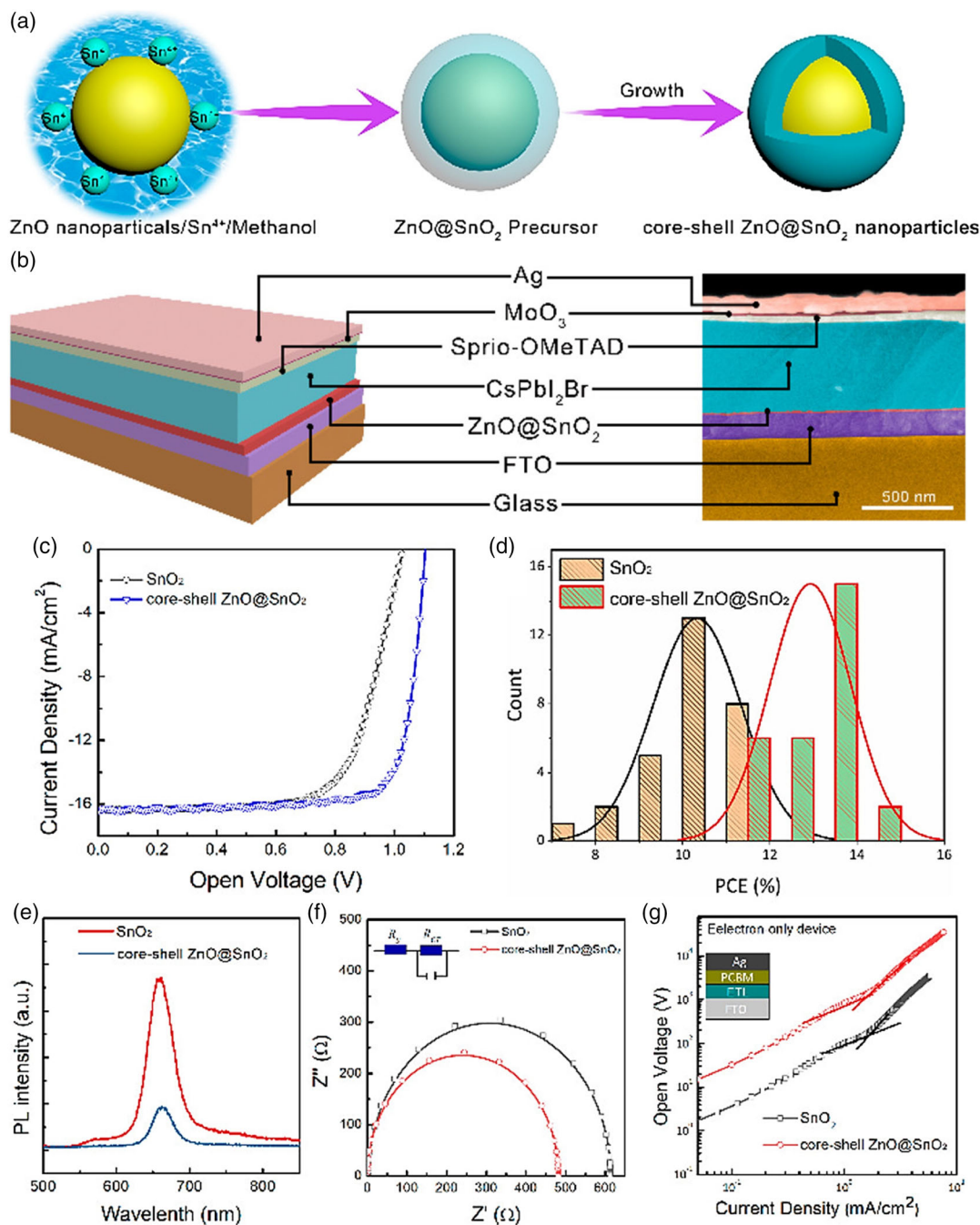


**Figure 33.** a) Synthetic diagram of the core-shell ZnO@SnO<sub>2</sub> nanoparticles, b) schematic of the device structure of the inorganic PVSCs, c) *J*-*V* characteristics of the inorganic PVSCs based on different electron transporting layers, d) PCE distribution e) PL spectra of the CsPbI<sub>2</sub>Br films based on different electron transporting layer, f) Nyquist plots of the core-shell ZnO@SnO<sub>2</sub> nanoparticles and SnO<sub>2</sub> nanoparticles. g) *V*-*I* curves of the electron-only device with a structure of FTO/ETL/PCBM/Ag. Reproduced with permission.<sup>[154]</sup> Copyright 2020, ACS.

SnO<sub>2</sub> ETL only gave a PCE of 11.66% (Figure 33c,d). Most importantly, the *V*<sub>OC</sub> of the SnO<sub>2</sub> ETL-based solar cells was 0.08 V, lower than the ZnO@SnO<sub>2</sub> ETL-based one. Better charge transfer properties between the perovskite layer and ZnO@SnO<sub>2</sub> were found, which was proved by the PL spectra (Figure 33e) and the EIS spectra (Figure 33f). The good electron mobility of ZnO than SnO<sub>2</sub> pushed the improvement of

the electron mobility from 0.0279 of the pure SnO<sub>2</sub> to 0.197 cm<sup>2</sup> V<sup>-1</sup> s<sup>-1</sup> (Figure 33g).<sup>[154]</sup>

### 6.3. Ions Doping of the ZnO Buffer Layer for OSCs and PVSCs

As mentioned above, the mobility of ZnO is not desired, which was one of the most important reasons for light-soaking.

Therefore, several routes have been developed to improve the electron mobility of ZnO through ion doping. Table 5 and 6 are the summary of the ion-doped ZnO for the organic and PVSCs. As summarized by these two tables, several kinds of ion-doped ZnO, including Al<sup>3+</sup>,<sup>[130]</sup> Li<sup>+</sup>,<sup>[155]</sup> Mg<sup>2+</sup>,<sup>[156]</sup>

Ga<sup>2+</sup>,<sup>[157]</sup> Sn<sup>4+</sup>,<sup>[158]</sup> and Cs<sup>2+</sup>,<sup>[159]</sup> have been developed to dope ZnO and used in OSCs and PVSCs. Among them, ion-doped ZnO films were fabricated through the sol-gel route and nanoparticles methods by adding the metal salts as the raw materials during the ZnO reaction process.

**Table 5.** Summary of the ion-doped ZnO as buffer layer of the OSCs.

Doping ions	Precursor or nanoparticles	Device structures	V <sub>OC</sub> [V]	J <sub>SC</sub> [mA cm <sup>-2</sup> ]	FF [%]	PCE [%]	References
Al:ZnO	Precursor	ITO/AZO/P3HT:PCBM/MoO <sub>3</sub> /Ag	0.590	11.02	58.40	3.78	[237]
Al:ZnO	Nanoparticles	ITO/AZO/P3HT:PCBM/PEDOT:PSS/Ag	0.569	8.36	50.80	2.42	[238]
Al:ZnO	Precursor	ITO/AZO/P3HT:PCBM/PEDOT:PSS/Ag	0.580	11.8	35.00	2.36	[239]
Al:ZnO	Precursor	ITO/AZO/P3HT:PC <sub>61</sub> BM/MoO <sub>3</sub> /Ag	0.628	7.21	68.21	3.09	[240]
Al:ZnO	–	ITO/AZO/PTB7:PC <sub>71</sub> BM/MoO <sub>3</sub> /Ag	0.732	15.13	70.98	7.86	[240]
Al:ZnO	–	ITO/AZO/P3HT:PC <sub>60</sub> BM/MoO <sub>3</sub> /Ag	0.610	8.7	68.30	3.54	[241]
Al:ZnO	–	ITO/AZO/PBDTPD:PC <sub>70</sub> BM/MoO <sub>3</sub> /Ag	0.870	12.5	62.00	6.7	[241]
Li:ZnO	Precursor	ITO/AZO/PBDTTT-C-T:PC <sub>70</sub> BM/MoO <sub>x</sub> /Ag	0.760	16.0	66.00	7.6	[241]
Li:ZnO	–	ITO/AZO/PBDTTT-C-T-EFT:PC <sub>70</sub> BM/MoO <sub>x</sub> /Ag	0.800	17.7	70.70	9.94	[241]
Li:ZnO	–	ITO/AZO/PTB7:PC <sub>70</sub> BM/MoO <sub>x</sub> /Ag	0.740	17.1	70.60	8.86	[241]
Li:ZnO	–	ITO/AZO/PTB7:PC <sub>71</sub> BM/MoO <sub>x</sub> /Ag	0.725	17.04	72.60	8.98	[242]
Li:ZnO	–	ITO/AZO/P3HT:PCBM/WO <sub>3</sub> /Ag	0.620	11.12	54.00	3.79	[243]
Li:ZnO	Precursor	ITO/AZO/PTB7-Th:PC <sub>71</sub> BM/MoO <sub>3</sub> /Al	0.780	18.31	66.80	9.54	[244]
Li:ZnO	Precursor	ITO/PEDOT:PSS/PTB7-Th:PC <sub>71</sub> BM/AZO/Al	0.801	16.94	74.80	10.14	[245]
Li:ZnO	Precursor	ITO/Li-ZnO/P3HT:PC <sub>61</sub> BM/MoO <sub>3</sub> /Ag	0.620	9.46	67.00	3.9	[170]
Mg:ZnO	Nanoparticles	ITO/Li-ZnO/PTB7:PC <sub>71</sub> BM/MoO <sub>3</sub> /Ag	0.750	16.54	68.00	8.4	[170]
Mg:ZnO	Nanoparticles	FTO/ZnO:Li/PTB7-Th:PC <sub>71</sub> BM/MoO <sub>x</sub> /Al	0.800	17.94	70.00	10.05	[171]
Mg:ZnO	–	FTO/ZnO:Li/PTB7-Th:IT-4 F/MoO <sub>x</sub> /Al	0.830	16.12	67.00	8.71	[171]
Mg:ZnO	Nanoparticles	ITO/ZnO:Li/P3HT:PCBM/MoO <sub>x</sub> /Al	0.610	9.93	68.00	4.07	[246]
Mg:ZnO	Precursor	ITO/ZnO:Li/PM6:Y6:PC <sub>71</sub> BM/MoO <sub>x</sub> /Ag	0.846	24.02	67.20	13.66	[172]
Mg:ZnO	Precursor	ITO/MgZnO/P3HT:PCBM/MoO <sub>3</sub> /Ag	0.577	9.70	56.80	3.17	[247]
Mg:ZnO	–	ITO/MgZnO/P3HT:ICBA/MoO <sub>3</sub> /Ag	0.828	9.90	67.00	5.48	[247]
Mg:ZnO	Precursor	ITO/Zn <sub>1-x</sub> Mg <sub>x</sub> O/PTB7:P <sub>71</sub> CBM/MoO <sub>3</sub> /Ag	0.740	16.78	66.99	8.31	[248]
Mg:ZnO	Precursor	ITO/ZMO/PTB7-Th:PC <sub>71</sub> BM/MoO <sub>3</sub> /Al	0.800	18.40	63.52	9.39	[249]
Ga:ZnO	Precursor	ITO/GZO/P3HT:PCBM/MoO <sub>3</sub> /Au	0.420	11.7	39.70	1.95	[157]
Ga:ZnO	Precursor	ITO/GZO/PCDTBT:PC <sub>71</sub> BM/MoO <sub>3</sub> /Al	0.900	10.46	59.03	5.56	[250]
Ga:ZnO	–	ITO/GZO/PTB7:PC <sub>71</sub> BM/MoO <sub>3</sub> /Al	0.750	14.96	64.95	7.34	[250]
Ga:ZnO	Precursor	ITO/ZnO:Ga/PBDTTT-CFPCBM/MoO <sub>3</sub> /Ag	0.764	15.9	63.70	7.74	[251]
Ga:ZnO	Precursor	ITO/GZO/PffBT4T-2OD:PC <sub>70</sub> BM/MoO <sub>x</sub> /Al	0.771	18.65	67.68	9.74	[252]
Ga:ZnO	Nanoparticles	ITO/PEDOT:PSS/PTB7-Th:PC <sub>71</sub> BM/GZO/Al	0.770	18.99	67.23	9.83	[253]
Cs:ZnO	Precursor	ITO/ZnO:Cs/P3HT:CdSe/MoO <sub>3</sub> /Ag	0.633	4.7	38.40	1.14	[254]
Cs:ZnO	Precursor	ITO/CZO/P3HT:PCBM/PEDOT:PSS/Ag	0.590	9	66.00	3.46	[255]
Cs:ZnO	–	ITO/ZnO:Cs/P3HT:PC <sub>61</sub> BM/MoO <sub>3</sub> /Ag	0.620	9.53	65.00	3.84	[256]
Cs:ZnO	–	ITO/ZnO:Cs/P3HT:IC <sub>60</sub> BA/MoO <sub>3</sub> /Ag	0.810	11.41	68.00	6.42	[256]
Cs:ZnO	Precursor	ITO/ZnO:Cs/PTB7:PC <sub>71</sub> BM/MoO <sub>3</sub> /Ag	0.730	14.88	73.00	7.89	[256]
Cs:ZnO	–	ITO/ZnO:Cs/P3HT:ICBA/PEDOT:PSS/ZnO/PFN/PTB7:PC <sub>71</sub> BM/MoO <sub>3</sub> /Ag	1.520	8.16	69.00	8.56	[256]
Zr:ZnO	Precursor	ITO/ZnO:Zr/PM6:Y6:PC <sub>71</sub> BM/MoO <sub>x</sub> /Ag	0.860	25.8	77.40	17.2	[257]
La:ZnO	Precursor	FTO/La-ZnO/P3HT:PCBM/V <sub>2</sub> O <sub>5</sub> /Ag	0.630	11.65	59.00	4.34	[258]
S:ZnO	Precursor	FTO/S-ZnO/P3HT:PCBM/V <sub>2</sub> O <sub>5</sub> /Ag	0.590	11.72	59.37	4.01	[259]
Yb:ZnO	Precursor	ITO/YZO/PBDB-T:IT-M/MoO <sub>3</sub> /Al	0.940	16.58	70.70	11.04	[260]
Cd:ZnO	Nanoparticles	ITO/CZO/PTB7-Th:PC <sub>71</sub> BM/MoO <sub>3</sub> /Ag	0.780	17.15	69.38	9.28	[261]

**Table 6.** Summary of the ion-doped ZnO as buffer layer of the PVSCs.

Doping ions	Precursor or nanoparticles	Device structures	$V_{oc}$ [V]	$J_{sc}$ [ $\text{mA cm}^{-2}$ ]	FF [%]	PCE [%]	References
Al:ZnO	Nanoparticles	ITO/AZO/PCBM/Perovskite/Spiro-MeOTAD/MoO <sub>x</sub> /Al	1.12	20.1	75.00	16.9	[167]
Al:ZnO	Nanoparticles	ITO/PEDOT:PSS/Perovskite/PC <sub>61</sub> BM/AZO/Ag	0.99	22.82	71.68	16.19	[168]
Al:ZnO	Nanoparticles	ITO/AZO:PDA/Perovskite/Spiro-OMeTAD/Ag	1.107	24.78	77.85	21.36	[169]
Al:ZnO	Precursor	FTO/ZnO/AZO/Perovskite/Carbon	0.72	16.0	71.00	8.23	[262]
Al:ZnO	Precursor	ITO/ZnO/AZO/Perovskite/P3HT/Au	0.84	21.93	57.00	10.45	[256]
Li:ZnO	Precursor	ITO/ZnO:Li/Perovskite/Spiro-OMeTAD/Ag	0.9975	22.22	70.77	16.14	[173]
Li:ZnO	Precursor	ITO/ZnO-Li/Perovskite/Spiro-OMeTAD/Au	1.10	22.00	73.30	17.8	[174]
Mg:ZnO	Nanoparticles	ITO/PEDOT:PSS/Perovskite/PCBM/ZnMgO/Al	0.91	22.71	75.00	15.61	[263]
Mg:ZnO	Nanoparticles	TCO/MgZnO/Perovskite/P3HT/Au	1.271	15.68	77.87	15.52	[264]
Mg:ZnO	Precursor	TO/ZMO/Perovskite/Spiro-OMeTD/Ag	1.064	18.7	68.30	13.7	[265]
Mg:ZnO	Precursor	ITO/ZMO/TiO <sub>2</sub> //Perovskite/Spiro-OMeTD/Ag/Graphene	1.120	23.86	78.91	21.08	[136]
Ni:ZnO	Precursor	ITO/ZnO:Ni/PCBM/Perovskite/P3HT/Au	0.83	23.73	70.00	13.79	[175]
N:ZnO	Precursor	FTO/N-ZnO/Perovskite/Spiro-OMeTD-Ag	1.0	21.8	73.00	15.91	[176]
I:ZnO	Precursor	ITO/ZnO:ZnO:I/Perovskite/Spiro-OMeTAD/Ag	1.13	22.42	71.99	18.24	[76]
K:ZnO	Precursor	ITO/ZnO-K/Perovskite/Spiro-OMeTAD/Au	1.13	23.00	77.10	19.90	[174]
Na:ZnO	Precursor	ITO/ZnO-Na/Perovskite/Spiro-OMeTAD/Au	1.11	22.50	75.40	18.9	[174]
Sn:ZnO	Nanoparticles	ITO/ZSO/Perovskite/PTAA/Au	1.05	21.60	67.00	15.30	[177]

The Al-doped ZnO (Al:ZnO) is the most widely studied and used as the substitute of ZnO in OSCs, both for the single<sup>[160]</sup> and tandem cells.<sup>[161]</sup> The Al:ZnO buffer layer could be prepared through both the sol-gel route and the nanoparticles route. The sol-gel Al:ZnO buffer layer was fabricated with 2-methoxyethanol as the solvent and aluminum acetate (AlAc) or aluminum nitrate (AlNi) as the dopant. Aprilla et al. investigated the influence of the doping concentration of Al on the device performance, and the result indicated that the concentration of Al majorly influenced the grain size and minorly influenced the crystallite size.<sup>[162]</sup>

The Al:ZnO nanoparticles were synthesized through a chemical reaction of Zn (Ac)<sub>2</sub>·2H<sub>2</sub>O, Al (NO<sub>3</sub>)<sub>3</sub>·9H<sub>2</sub>O, and ethanolamine (EA)<sup>[163]</sup> or isopropyl amine<sup>[164]</sup> in ethanol or the mixed solvent of methanol and ethanol at room temperature. Though the nanoparticles were synthesized at low temperatures, the Al ions were still successfully doped in the ZnO nanoparticles, which was proved by SEM mapping.<sup>[164]</sup> Because the electron mobility increased through doping Al<sup>3+</sup>, the working thicknesses of Al:ZnO is larger than that of ZnO, showing highly compatible with roll-to-roll printing of OSCs.<sup>[163]</sup> Using this buffer layer, a prominent PCE approaching 9% was achieved using a 120 nm-thick Al:ZnO buffer layer for the PTB7-Th:PC<sub>71</sub>BM inverted solar cells. Later, Fang et al. replaced EA with KOH, and the synthesized Al:ZnO nanoparticles could be dissolved in TFE solvent and used to deposit on the organic active layer in the conventional structure OSCs. For the PTB7-Th:PC<sub>71</sub>BM solar cells, the highest performance was achieved at 10.14% with a rather high FF of 74.8%.<sup>[165,166]</sup> The commercial AZO nanoparticles combined with PCBM as the composite ETL was developed in the PVSCs with a PCE 16.9% of 16.19% by Franky et al.<sup>[167]</sup> and Zhang et al.,<sup>[168]</sup> respectively. Chen et al.<sup>[169]</sup> fabricated PVSCs with an efficiency of 21.36% based

on the AZO:PDA ETL. At the same time, the flexible devices showed a PCE of 18.51%, which is the highest performance record among ZnO-based flexible PVSCs.

Hao et al. fabricated the Li-ZnO ETL through nanoparticles method by solving ZnO nanopowders and lithium hydroxide into the ammonia solution.<sup>[170]</sup> The performance of 8.4% for the PTB7-PC<sub>71</sub>BM solar cells was achieved, which was higher than the devices of 7.5% performance with pristine ZnO as the ETL. Li-doped ZnO ETL was prepared by the sol-gel method via spin coating the precursor solution of zinc acetate dihydrate and lithium chloride in ethanolamine and 2-methoxyethanol.<sup>[171]</sup> The maximum performance of PTB7-Th:PC<sub>71</sub>BM-based fullerene devices improved from 8.59% to 10.05%, and PTB7-Th:IT-4F-based nonfullerene devices showed excellent stability, maintaining higher than 80% of the initial PCE after 1000 h. After the UV treatment of ZnO, the conductivity of ZnO would increase, which leads to the increase of the photoactive layer area. Ma et al.<sup>[172]</sup> employed the Li-doped ZnO ETL, which addressed the problem. In the perovskite solar cells, the Li-ZnO ETLs were fabricated through spin coating the bis(trifluoromethane)sulfonimide lithium (Li-TFSI) salt in acetonitrile solvent over the ZnO film under low-temperature condition.<sup>[173]</sup> The device hysteresis phenomena were suppressed and the efficiency of PVSC was improved. Alkali-metal-doped ZnO films were reported by dipping ZnO films into various alkali-metal hydroxide solutions.<sup>[174]</sup> The efficiency of PVSCs reached 19.90%, 18.90%, and 17.80% for the ZnO-K, ZnO-Na, and ZnO-Li ETL, respectively, which was superior to the pristine ZnO devices of a PCE of 16.10%.

Mg-doped ZnO ETL was also frequently used in OSCs and PVSCs. Zheng et al.<sup>[156]</sup> developed the Mg-doped ZnO buffer layer for high-efficiency OSCs. The Mg-doped ZnO films were fabricated through the sol-gel route with a precursor solution of mixing zinc acetate dihydrate with magnesium acetate

tetrahydrate dissolved in a mixture of 2-methoxyethanol and ethanolamine. The doping of Mg in the ZnO buffer layer was proved by the XPS spectra. Using the Mg-doped ZnO (ZnMgO) as the ETL of the OSCs, the device showed an increased performance of 9.39% with PTB7-Th:PC<sub>71</sub>BM as the active layer relative to the ZnO ETL-based devices. Moreover, the ZnMgO ETL-based solar cells showed significantly improved long-term stability relative to the control cells. The device kept an efficiency of 8.06%, which was around 85% of the initial value after 1 year of storage in the air. Similarly, Zheng et al.<sup>[136]</sup> used ZnMgO as ETL of the PVSCs. The ZnMgO films were fabricated by spin coating the precursor solution of magnesium acetate tetrahydrate and ethanolamine in 2-methoxyethanol on the compact ZnO layer. The PVSCs exhibited an efficiency of 21.1% and excellent air stability with the ZnMgO films as ETL.

Ni-, N-, I-, and Sn-doped ZnO ETLs have been developed in PVSCs. Yang et al. prepared a Ni-doped ZnO ETL by immersing the ZnO seed layer into the precursor solution consisting of zinc sulfate heptahydrate, nickel acetate hydrate, and ammonium chloride in deionized water at the solution pH of 7, and an efficiency of 13.79% was obtained in PVSCs.<sup>[175]</sup> Mahmood et al. introduced N-ZnO ETL by electrospraying the precursor of Zinc acetate dihydrate and ammonium acetate in isopropyl alcohol:water solution. The maximum efficiency of PVSCs of 15.91% was achieved.<sup>[176]</sup> The ZnO:I ETL was prepared in PVSCs by a two-step hydrothermal process.<sup>[76]</sup> First, the ZnO seed layer was fabricated by the traditional sol-gel method. Afterward, the ZnO:I film grew by dipping the ZnO seed layer into the mixture solution of zinc nitrate hexahydrate and hexamethylenetetramine in a neutral solution of iodic acid for 3 h at 91.5 °C. Sn-doped ZnO nanoparticles were fabricated via dissolving the mixture of N<sub>2</sub>H<sub>4</sub>·H<sub>2</sub>O, ZnCl<sub>2</sub>, and SnCl<sub>4</sub>·H<sub>2</sub>O in the water, and reacting at 90 °C for 12 h. The flexible PVSCs reached a steady-state efficiency of 14.85%.<sup>[177]</sup>

Another problem of ZnO-involved PVSCs is the serious surface recombination, which was caused by intrinsic defects, like Zn vacancies, oxygen vacancies, zinc interstitials, oxygen interstitials, zinc antistites, and oxygen antistites.

## 7. Solution-Processable ZnO in Printed Photovoltaics

### 7.1. Ink Engineering

#### 7.1.1. Aggregate of the ZnO Nanoinks and Solution

For the ZnO ETL from the colloidal route, another big problem is its high trend to agglomerate due to the high surface energy of the nanoparticles through polycondensation of surface hydroxyl groups.<sup>[19,178,179]</sup> This extensive aggregation leads to the formation of an unfavorable interface between the buffer layer and the photoactive layer,<sup>[35,121]</sup> and results in poor device performance and performance uniformity, especially for printed photovoltaics. Thus, the thermodynamic instability of the ZnO ink is a major barrier to the large-area industrial and commercialization application of this material as a buffer layer in organic photoelectronic devices. To understand the influence of the ZnO NPs stability, solubility, and aggregation properties, Cao et al.<sup>[180]</sup> studied the

impact of pH, reaction time, and growth temperature, and found growth of ZnO nanocrystals by oriented attachment (OA) (Figure 34). Figure 34a shows the dislocation of A-B and C-D. They also reported that the OA process highly depended on the type of alcohol, water content in the solution, and pressure. Such a process was better controlled in ethanol compared to methanol. Reaction time, temperature, and pH also impacted a lot. In addition, the growth of nanoparticles into nanorods was controlled by time and temperature. Figure 34c,d shows the large particles formed by the merging of adjacent particles. Areas A-B and C-D “aligned” with each other and maintained their perfect relative crystallographic orientation. Recently, Luo et al.<sup>[181]</sup> studied the detailed dependence of ZnO nanoparticles ink aggregation and attachment process under different solvent and acid–base pH conditions. First, the dispersibility of ZnO NPs in different alcohols including methanol (MeOH), ethanol (EtOH), isopropyl alcohol (IPA), *n*-butanol (BuOH), and ethylene glycol monomethyl ether (EGME) was investigated. The aggregation size of ZnO NPs in different solvents varied due to the reason of interaction force intensity between ZnO NPs surface charge with solvents. Then, the effect of acid/base pH condition on the dispersibility of ZnO inks was investigated through adding the MAE and TMAH as the acid and base into the ZnO ink, respectively. Based on the XPS results, they found the change of OH peaks due to the addition of TMAH was the main reason for the more serious aggregation of NPs under the base pH condition, indicating the strong interaction formation between ZnO nanoparticles was attributed to the surface hydroxyl groups. In contrast, the addition of MEA acid could react with surface hydroxyl groups and break the aggregation process through the Lewis acid–base reaction. Finally, with the use of MEA acid, the hydroxyl groups were removed. The ZnO NPs could be dispersed in different alcohol solvents and the ZnO inks could keep long-term stability during storage in a closed and an open vessel.

The distribution properties, as well as the long-term stability of the nanoinks, were mainly influenced by the surface potential. The nanoinks were composited of nanoparticles, surfactant, and solvent. Therefore, the distribution properties were influenced by the interaction of nanoparticles, surfactants, and the solvent. For the ZnO nanoparticles obtained from the chemical reaction of KOH and ZnOAC<sub>2</sub>, it was found such ZnO nanoparticles could keep stable in the mixed solvent of chloroform and methanol with a mixing ratio of 1:1. Interestingly, the inks with a high amount of chloroform or methanol are both cloudy, implying the formation of ZnO aggregation.<sup>[182]</sup> To suppress aggregation, several alternative approaches have been developed, such as modification with polyvinylpyrrolidone (PVP) surfactant,<sup>[183]</sup> *n*-propylamine,<sup>[184]</sup> 2-aminoethanol,<sup>[25]</sup> and coupling agents,<sup>[178,185]</sup> and cosolvent engineering.<sup>[182,186]</sup> Fang et al. demonstrated adjusting the solvents ratios (chloroform vs methanol) (as shown in Figure 35a,b) could control the dispersion and aggregation properties. Using a mixed solvent of methanol and chloroform with a ratio of 1:1 could enable stable ZnO inks and compact ZnO films, which helped to achieve a good device performance.<sup>[182]</sup>

Adding a stabilizer is an effective method to improve the dispersion. Yi et al.<sup>[187]</sup> and Krebs et al.<sup>[19]</sup> found the modification of ZnO surfaces with 2-(2-methoxyethoxy) acetic acid (MEA) to stabilize colloidal and prevented aggregation of ZnO particles,

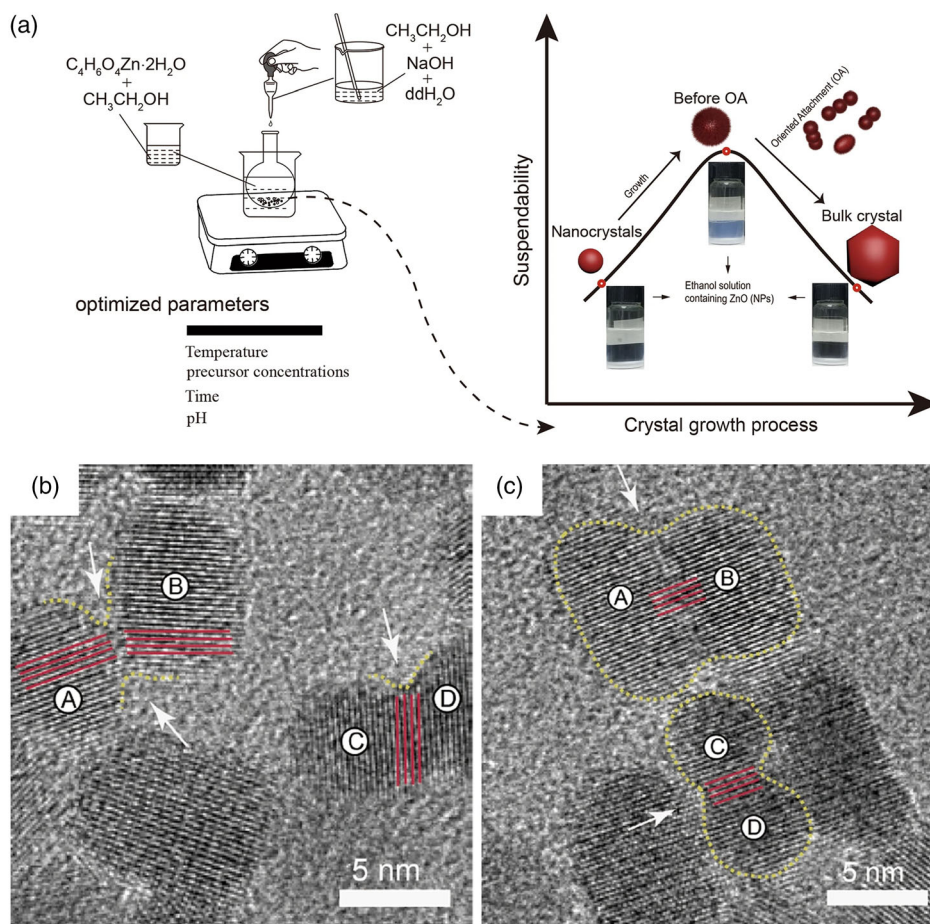


**Figure 34.** a) Schematic illustration of ZnO NPs synthesis and growth. b) Dislocations resulted from the oriented attachment (OA) process. c) Nanoparticles formed layer-by-layer either parallel or perpendicular to the  $c$ -axis of ZnO. Reproduced with permission.<sup>[180]</sup> Copyright 2019, Springer Nature.

and they also modified these ZnO nanoparticles with PEI (as shown in Figure 35c). Kim et al. used titanium diisopropoxide bis(acetylacetonate) ( $Ti(acac)_2$ ) as a stabilizer of ZnO NPs. With such functionalization, ZnO exhibited improved long-term stability and maintained stability for months of aging (Figure 35d–f).<sup>[188]</sup> The photographs showed the ZnO nanoinks had milky suspension 2 weeks later after synthesis. The ZnO inks containing ( $Ti(acac)_2$ ) with different concentrations (f-ZnO-L, M, and H) were low, mid, and high concentrations of  $Ti(acac)_2$  and kept high transparency. It was ascribed to the functionalization of ZnO by acetylacetonate, which effectively reduced the aggregations of NPs. Meanwhile, tetravalent Ti atoms in the ZnO lattice passivated deep-level traps of the NPs and led to significant reduction of green luminescence (Figure 35f).

In addition, surface ligand modification through chemical reactions can also improve ink stability. Modification with silane coupling agents involving a chemical reaction between the surface hydroxyl groups of the metal oxides and the alkoxy groups of the coupling agent is a popular approach in the field of biomaterials for improving the stability of the dispersions,<sup>[178,189]</sup> and the hydrophily,<sup>[178,190]</sup> modulating the luminescence properties.<sup>[191]</sup> Wei et al. synthesized APTMS-capped ZnO (ZnO@APTMS) inks (Figure 35g) to solve this problem.

Figure 35h shows the dynamic light scattering of the nanoparticles and the device performance of the solar cells using the inks that were stored for different time. The ZnO@APTMS showed quite long-term inks stability, with negligible increase in the average diameter even after 12 months of storage in air. Specifically, the diameters of the pristine ZnO NPs grew dramatically from around 5 nm to approximately 250 nm. The diameter of the ZnO@APTMS NPs only increased slightly from 7 nm to 10 nm during 12 months of storage in air. Additionally, the OSCs using the ZnO@APTMS ETLs that were stored for 12 months gave a nearly comparable performance as the device with ETLs fabricated using fresh inks (Figure 35i).<sup>[105]</sup> The working thickness of the roll-to-roll printed ZnO@APTMS could reach as high as 90 nm.

### 7.1.2. Low-Temperature Processable ZnO Nanoinks

Besides, a postthermal annealing at a relatively high temperature ( $\approx 200^\circ C$ ) is another disadvantage of the sol-gel ZnO buffer layer, which would limit its application in flexible OSCs and tandem solar cells. Thus, some works have been conducted to develop low-temperature thermal-treated sol-gel metal oxides

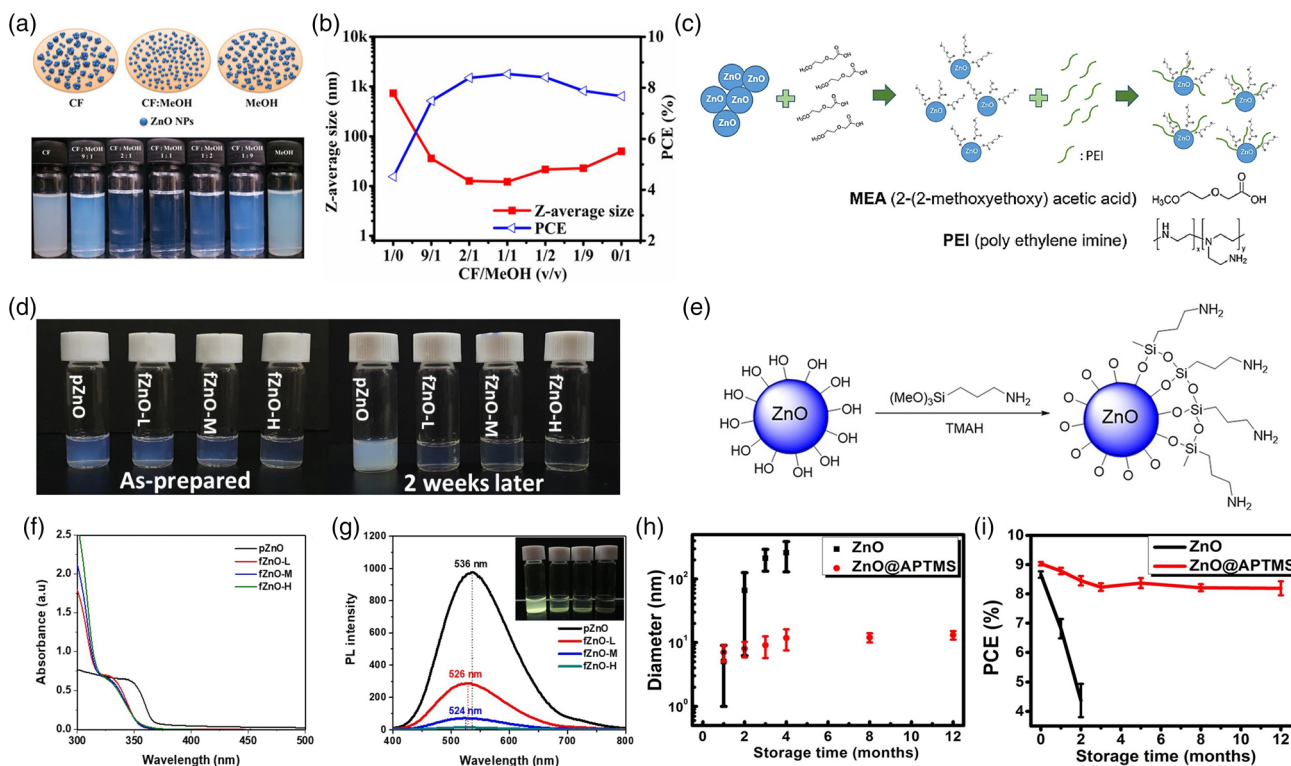


**Figure 35.** a,b) Using methanol and CF cosolvent to achieve stable ZnO inks. Reproduced with permission.<sup>[182]</sup> Copyright 2014, ACS. c) The schematic diagram of MEA improving the dispersibility of the ZnO nanoparticles. Reproduced with permission.<sup>[187]</sup> Copyright 2020, Elsevier. d) Photographs of ZnO NP solutions after the addition of Ti(acac). e) UV-vis absorption and f) photoluminescence spectra of ZnO NP solutions. Reproduced with permission.<sup>[188]</sup> Copyright 2020, Springer Nature. g) Schematic diagram of silane capped ZnO, and h,i) the long-term stability of the silane capped ZnO and the device performance. Reproduced with permission.<sup>[105]</sup> Copyright 2018, ACS.

by regulating the precursor solution. As an improvement, the ZnO films could form at around 125–140 °C through solvent engineering,<sup>[12,192]</sup> or through ion doping.<sup>[193]</sup> In addition, the precursor also decided the annealing temperature required to transform the precursor to ZnO for the sol-gel method. The purified ammine-hydroxy zinc solutions  $Zn(NH_3)_2(OH)_2$  aqueous precursor solution affords ZnO layers by ammine dissociating and hydroxide condensation/dehydration reaction at low temperatures (<100 °C). Similar precursors include  $Zn_5(OH)_8(NO_3)_2 \cdot 2H_2O$ , and  $Zn_5(OH)_8(NO_3)_2 \cdot 2NH_3$ . Cowan et al. replaced the raw material ZnAc with diethylzinc (deZn), and this precursor showed a much lower conversion temperature. The annealing temperature of the deZn precursor film was only 120 °C.<sup>[134]</sup> In addition, the ZnO films from deZn precursor have improved crystallization relative to that of the ZnAc (Figure 36a). Such ZnO films also contained lower nonstoichiometric oxygen amounts (the ratio of oxygen coordinated in the ZnO lattice to nonstoichiometric oxygen amounts to 1.9 in ZnAc and 1.5 in deZn), suggesting less stoichiometric oxygen present in deZn crystallites (Figure 36b). It also showed that the long-term stability (Figure 36c–f) of the poly[*N*-9'-heptadecanyl-2,7-carbazole-alt-5,5-(4',7'-di-2thienyl)-2',1',3'-benzothiadiazole]] PCDTBT:(6,6)-phenyl  $C_{71}$ -butyric acid methyl ester (PC<sub>71</sub>BM) cells are sensitive to the Zn precursor that used to fabricate the ZnO buffer layer as well. The deZn precursor yields devices that are more

stable in  $V_{OC}$  and FF during the continuous illumination for the devices without nonencapsulation.<sup>[194]</sup> As shown in Figure 36c, the ZnAc device gradually developed substantial current leakage in reverse bias and reduce of  $V_{OC}$  under continuous illumination exceeding 600 h. The deZn device showed much better stability in  $V_{OC}$  and  $J_{SC}$ . The evolution of device performance is shown in Figure 36g–j.

## 7.2. Printing Fabrication

Because of the environmentally friendly and cost-effective ZnO inks, ZnO has been used in the roll-to-roll printed OSCs and PVSCs. Martinez-Ferrero estimated the cost of the printed OSCs, and the result showed the printed ZnO only cost 0.33 Euro  $m^{-2}$ , which is much cheaper than the ITO electrode and the organic active materials.<sup>[195]</sup> Krebs has used the ethanol or acetone-dispersed ZnO inks to fabricate the ZnO ETL through the slot-die coating.<sup>[49,196–198]</sup>

Besides slot-die coating, large-area ZnO films have been fabricated through gravure printing. Zhang et al. carefully optimized the morphology and thickness of the printed ZnO films through microgravure printing. However, using the printed ZnO films, the device gave relatively low device performance, which was due to poor film quality.<sup>[36]</sup> To solve this issue, Wei et al.

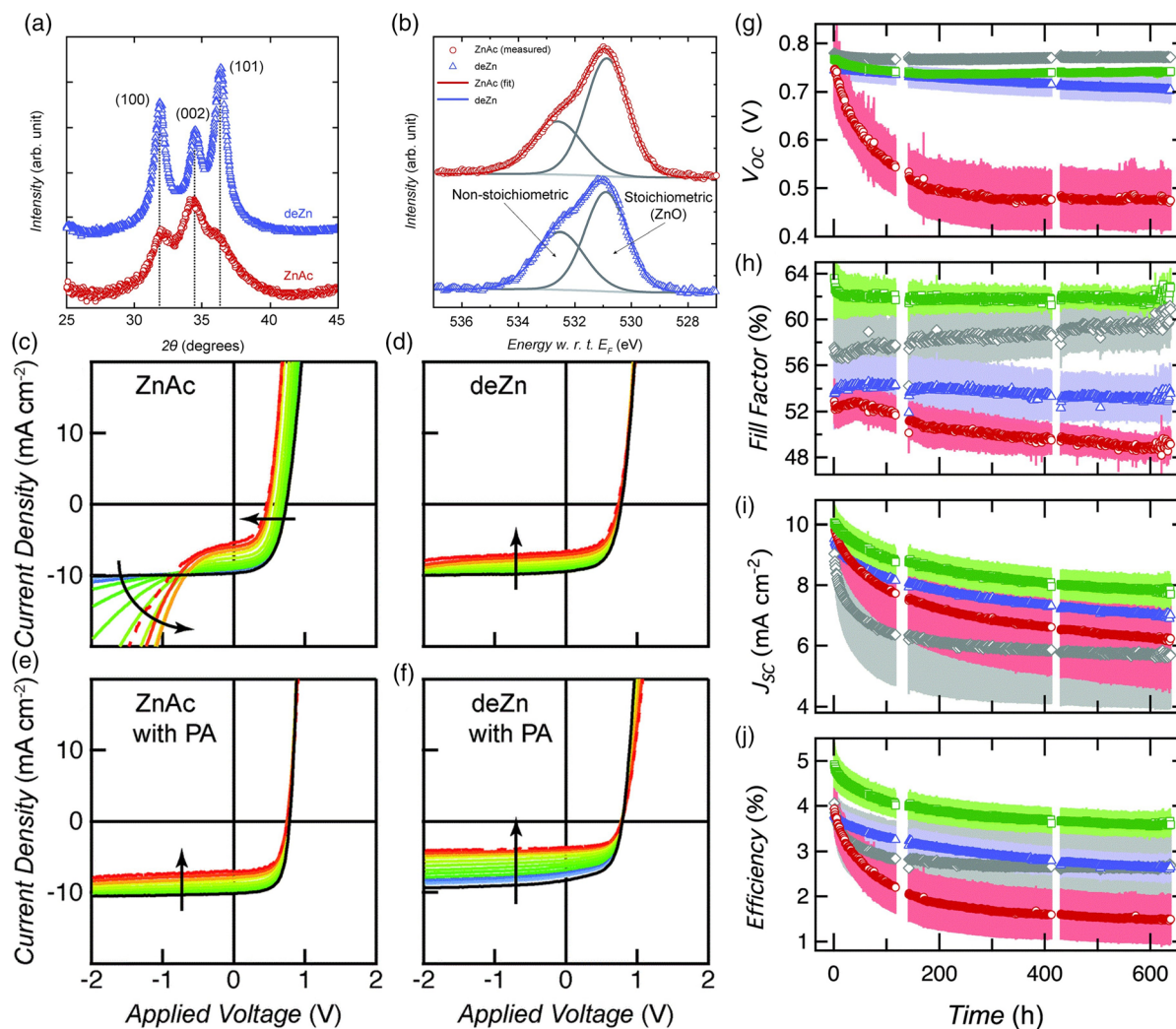


**Figure 36.** a) XRD patterns of the ZnO films with ZnAc and deZn as the sol-gel precursor, and b) XPS spectra of the films fabricated from different precursors. c–f)  $J$ - $V$  characteristics of the devices during aging with ZnAc, deZn, ZnAc with PA, deZn with PA as ETLs. Average performance characteristic parameters of devices with ZnAc (red circles), deZn (blue triangles), PA-modified ZnAc (green squares), and PA-modified deZn (gray diamonds) electrodes: g)  $V_{oc}$ , h) FF, i)  $J_{sc}$ , and j) PCE, all as a function of time exposed to the degradation solar simulator. Bars indicated one standard deviation of the mean. Reproduced with permission.<sup>[194]</sup> Copyright 2015, RSC.

replaced the ZnO with ZnO:PEI composite inks. Figure 37 shows the cross-sectional SEM images of the printed ZnO:PEI films. With the increase of  $R$  ( $R$  = printing roller speed/web speed), the thickness of ZnO films increased. When the  $R$  and  $S$  were 4.8 and 0.7, the thickness of ZnO was around 90 nm. The results demonstrated the working thickness of the microgravure printed ZnO:PEI can reach 90 nm with maintained high performance, demonstrating the great potential of ZnO:PEI for the roll-to-roll printed OSCs.<sup>[199]</sup> Similarly, the working thickness of the silane-capped ZnO also reached to around 90 nm fabricated through microgravure printing.<sup>[105]</sup>

For the PVSCs, Dak et al.<sup>[64]</sup> reported the fabrication of PVSCs through the slot-die coating. In that work, besides the perovskite layer, the ZnO ETL and P3HT HTL were deposited through slot-die coating as well. A 25 nm-thick ZnO layer was deposited from ZnO NPs inks.

## 8. Summary and Perspective

To conclude, we have overviewed the development of the solution-processed ZnO buffer layer in OSCs and PVSCs. We have shown ZnO has been widely used as the buffer layer in OSCs and PVSCs with different structures, such as conventional, inverted, and tandem OSCs. Besides, the previous works showed that ZnO has great potential for the large-scale manufacture of OSCs. However, there are still several problems as it was utilized in both the spin-coated and roll-to-roll (R2R) printed solar cells that stand for academic research and industrial manufacturing, respectively. For the application of a small-area coating, the light-soaking issue and low charge collection efficiency caused by surface defects always occurred. And for the application of R2R printing, more concerns might be focused on the reliability of the nanoinks. Long-term stable ZnO nanoink

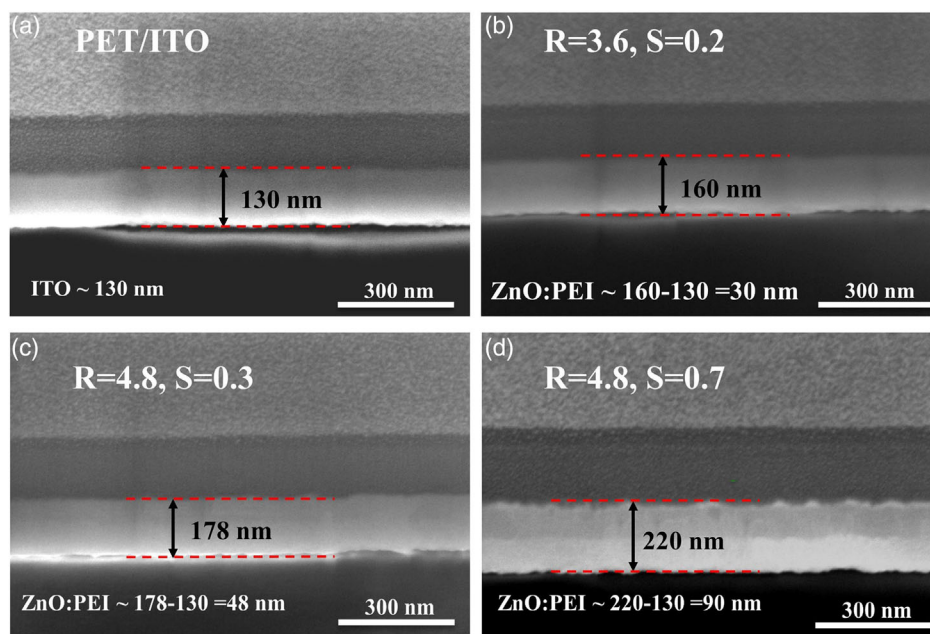


**Figure 37.** The cross-sectional SEM images of the roll-to-roll microgravure printed ZnO:PEI ETL with different R and S. Reproduced with permission.<sup>[199]</sup> Copyright 2019, Elsevier.

with suitable rheological property is a basic for printed photovoltaics.

Besides, the ZnO electron buffer layer from the sol-gel route has another issue that should be fabricated under controlled humidity in both the deposition and annealing process; otherwise, the nonfully conversion from the zinc precursor to ZnO occurred and caused poor device performance. The XPS spectra displayed that as the humidity increased, the intensity of the non-stoichiometric peaks ( $O_{ii}$ ) decreased relative to the stoichiometric peak ( $O_i$ ). The humidity also influenced the extinction coefficient of the ZnO film. The films formed under lower humidity exhibit lower work function and resulted in higher  $V_{OC}$  for the devices. It was found that the highest performance was achieved with ZnO ETLs deposited at 13% room humidity (RH) and annealing at 0% RH, while the poorest device was fabricated with ZnO coated at 75% RH and annealed at 75% RH.<sup>[200]</sup> Such a high sensitivity of performance to the fabrication humidity would be a big challenge for high-performance roll-to-roll printed photovoltaic cells.

Third, with the development of high-efficiency nonfullerene OSCs, the stability issue matters more in the future. Unfortunately, the use of a solution-processed ZnO buffer layer seems to be unfavorable to the device long-term stability. But all these problems of the ZnO buffer layer have been attributed to the surface defects, and modification of the ZnO surface with proper approaches could solve these problems. On this basis, surface chemical control is important for the solution-processed ZnO buffer layer to promote its future industrial application.

## Acknowledgements

The authors acknowledge the support of the Youth Innovation Promotion Association, CAS (grant no. 2019317) and Young Cross Team Project of

CAS (grant no. JCTD-2021-14) for their work on solution-processable ZnO for organic and PVSCs.

## Conflict of Interest

The authors declare no conflict of interest.

## Keywords

nanoinks, organic solar cells, perovskite solar cells, sol-gel, solution-processable ZnO

Received: November 11, 2022

Revised: January 15, 2023

Published online: July 12, 2023

- [1] Q. Liu, Y. Jiang, K. Jin, J. Qin, J. Xu, W. Li, J. Xiong, J. Liu, Z. Xiao, K. Sun, S. Yang, X. Zhang, L. Ding, *Sci. Bull.* **2020**, *65*, 272.
- [2] M. Zhang, L. Zhu, G. Zhou, T. Hao, C. Qiu, Z. Zhao, Q. Hu, B. W. Larson, H. Zhu, Z. Ma, Z. Tang, W. Feng, Y. Zhang, T. P. Russell, F. Liu, *Nat. Commun.* **2021**, *12*, 309.
- [3] L. L. Zhan, S. X. Li, X. X. Xia, Y. K. Li, X. H. Lu, L. J. Zuo, M. M. Shi, H. Z. Chen, *Adv. Mater.* **2021**, *33*, 2007231.
- [4] M. A. Green, E. D. Dunlop, J. Hohl-Ebinger, M. Yoshita, N. Kopidakis, A. W. Y. Ho-Baillie, *Prog. Photovolt.* **2019**, *28*, 3.
- [5] D. Damberga, R. Viter, V. Fedorenko, I. Iatsunskyi, E. Coy, O. Graniel, S. Balme, P. Miele, M. Bechelany, *J. Phys. Chem. C* **2020**, *124*, 9434.
- [6] H. Cheun, C. Fuentes-Hernandez, Y. H. Zhou, W. J. Potscavage, S. J. Kim, J. Shim, A. Dindar, B. Kippelen, *J. Phys. Chem. C* **2010**, *114*, 20713.
- [7] I. Jeon, Y. Qian, S. Nakao, D. Ogawa, R. Xiang, T. Inoue, S. Chiashi, T. Hasegawa, S. Maruyama, Y. Matsuo, *J. Mater. Chem. A* **2016**, *4*, 18763.

- [8] Y. Jouane, S. Colis, G. Schmerber, A. Dinia, P. Bazylewski, G. S. Chang, Y. A. Chapuis, *Thin Solid Films* **2015**, 576, 23.
- [9] M. S. White, *Appl. Phys. Lett.* **2006**, 89, 143517.
- [10] A. K. K. Kyaw, X. W. Sun, C. Y. Jiang, G. Q. Lo, D. W. Zhao, D. L. Kwong, *Appl. Phys. Lett.* **2008**, 93, 221107.
- [11] Y. M. Sun, J. H. Seo, C. J. Takacs, J. Seifert, A. J. Heeger, *Adv. Mater.* **2011**, 23, 1679.
- [12] G. Iannaccone, A. Bernardi, R. Suriano, C. L. Bianchi, M. Levi, S. Turri, G. Griffini, *RSC Adv.* **2016**, 6, 46915.
- [13] P. Jiang, J. Chen, F. Qin, T. Liu, S. Xiong, W. Wang, C. Xie, X. Lu, Y. Jiang, H. Han, Y. Zhou, *Angew. Chem. Int. Ed.* **2022**, 61, 202208815.
- [14] X. Y. Liu, Z. Zheng, J. Q. Wang, Y. F. Wang, B. W. Xu, S. Q. Zhang, J. H. Hou, *Adv. Mater.* **2022**, 34, 2106453.
- [15] L. Spanhel, M. A. Anderson, *J. Am. Chem. Soc.* **1991**, 113, 2826.
- [16] E. A. Meulenkaamp, *J. Phys. Chem. B* **1998**, 102, 5566.
- [17] C. Pacholski, A. Kornowski, H. Weller, *J. Am. Chem. Soc.* **2002**, 124, U351.
- [18] S. K. Hau, H. L. Yip, N. S. Baek, J. Y. Zou, K. O'Malley, A. K. Y. Jen, *Appl. Phys. Lett.* **2008**, 92, 253301.
- [19] F. C. Krebs, Y. Thomann, R. Thomann, J. W. Andreasen, *Nanotechnology* **2008**, 19, 424013.
- [20] L. Qian, Y. Zheng, K. R. Choudhury, D. Bera, F. So, J. G. Xue, P. H. Holloway, *Nano Today* **2010**, 5, 384.
- [21] L. Qian, Y. Zheng, J. G. Xue, P. H. Holloway, *Nat. Photonics* **2011**, 5, 543.
- [22] Y. V. Panasiuk, O. E. Raevskaya, O. L. Stroyuk, S. Y. Kuchmiy, V. M. Dzhagan, M. Hietschold, D. R. T. Zahn, *Nanotechnology* **2014**, 25, 075601.
- [23] Y. X. Yang, Y. Zheng, W. R. Cao, A. Titov, J. Hyvonen, J. R. Manders, J. G. Xue, P. H. Holloway, L. Qian, *Nat. Photonics* **2015**, 9, 259.
- [24] J. Wang, Y. J. Lee, J. W. P. Hsu, *J. Phys. Chem. C* **2014**, 118, 18417.
- [25] I. Jeon, J. W. Ryan, T. Nakazaki, K. S. Yeo, Y. Negishi, Y. Matsuo, *J. Mater. Chem. A* **2014**, 2, 18754.
- [26] S. Bai, Z. W. Wu, X. L. Xu, Y. Z. Jin, B. Q. Sun, X. J. Guo, S. S. He, X. Wang, Z. Z. Ye, H. X. Wei, X. Y. Han, W. L. Ma, *Appl. Phys. Lett.* **2012**, 100, 203906.
- [27] H. L. You, J. C. Zhang, Z. Y. L. Zhang, C. F. Zhang, Z. H. Lin, J. J. Chang, G. Q. Han, J. C. Zhang, G. Lu, Y. Hao, *Energies* **2017**, 10, 494.
- [28] H. C. Huang, T. E. Hsieh, *Nanotechnology* **2010**, 21, 295707.
- [29] F. C. Krebs, *Sol. Energy Mater. Sol. Cells* **2009**, 93, 465.
- [30] J. B. Guo, Y. F. Han, Z. H. Xu, W. S. Zha, J. Fang, Q. Luo, L. Q. Liu, C. Q. Ma, *Flex. Print. Electron.* **2022**, 7, 025013.
- [31] M. A. Ibrahim, H. Y. Wei, M. H. Tsai, K. C. Ho, J. J. Shyue, C. W. Chu, *Sol. Energy Mater. Sol. Cells* **2013**, 108, 156.
- [32] Z. S. Hu, G. Oskam, R. L. Penn, N. Pesika, R. C. Searson, *J. Phys. Chem. B* **2003**, 107, 3124.
- [33] C. M. Pelicano, H. Yanagi, *Appl. Surf. Sci.* **2019**, 467–468, 932.
- [34] Y. J. Kang, K. Lim, S. Jung, D. G. Kim, J. K. Kim, C. S. Kim, S. H. Kim, J. W. Kang, *Sol. Energy Mater. Sol. Cells* **2012**, 96, 137.
- [35] G. Q. Ji, Y. L. Wang, Q. Luo, K. Han, M. L. Xie, L. P. Zhang, N. Wu, J. Lin, S. G. Xiao, Y. Q. Li, L. Q. Luo, C. Q. Ma, *ACS Appl. Mater. Interfaces* **2018**, 10, 943.
- [36] C. J. Zhang, Q. Luo, H. Wu, H. Y. Li, J. Q. Lai, G. Q. Ji, L. P. Yan, X. F. Wang, D. Zhang, J. Lin, L. W. Chen, J. L. Yang, C. Q. Ma, *Org. Electron.* **2017**, 45, 190.
- [37] P. Cheng, H. T. Bai, N. K. Zawacka, T. R. Andersen, W. Q. Liu, E. Bundgaard, M. Jorgensen, H. Chen, F. C. Krebs, X. W. Zhan, *Adv. Sci.* **2015**, 2, 1500096.
- [38] A. K. K. Kyaw, D. H. Wang, D. Wynands, J. Zhang, T. Q. Nguyen, G. C. Bazan, A. J. Heeger, *Nano. Lett.* **2013**, 13, 3796.
- [39] W. Vervisch, G. Rivie, S. Vedraïne, S. Biondo, P. Torchio, D. Duché, J.-J. Simon, L. Escoubas, *J. Appl. Phys.* **2012**, 111, 094506.
- [40] W. W. Li, A. Furlan, K. H. Hendriks, M. M. Wienk, R. A. J. Janssen, *J. Am. Chem. Soc.* **2013**, 135, 5529.
- [41] J. Yang, R. Zhu, Z. R. Hong, Y. J. He, A. Kumar, Y. F. Li, Y. Yang, *Adv. Mater.* **2011**, 23, 3465.
- [42] J. Y. Kim, K. Lee, N. E. Coates, D. Moses, T. Q. Nguyen, M. Dante, A. J. Heeger, *Science* **2007**, 317, 222.
- [43] D. Lee, W. K. Bae, I. Park, D. Y. Yoon, S. Lee, C. Lee, *Sol. Energy Mater. Sol. Cells* **2011**, 95, 365.
- [44] S. Kouijzer, S. Esiner, C. H. Frijters, M. Turbiez, M. M. Wienk, R. A. J. Janssen, *Adv. Energy Mater.* **2012**, 2, 945.
- [45] N. Li, T. Stubhan, J. Krantz, F. Machui, M. Turbiez, T. Ameri, C. J. Brabec, *J. Mater. Chem. A* **2014**, 2, 14896.
- [46] N. Li, T. Stubhan, D. Baran, J. Min, H. Q. Wang, T. Ameri, C. J. Brabec, *Adv. Energy Mater.* **2013**, 3, 301.
- [47] C.-H. Chou, W. L. Kwan, Z. R. Hong, L. M. Chen, Y. Yang, *Adv. Mater.* **2011**, 23, 1282.
- [48] C.-H. Chou, W. L. Kwan, Z. Hong, L.-M. Chen, Y. Yang, *Adv. Mater.* **2011**, 23, 1282.
- [49] T. R. Andersen, H. F. Dam, M. Hösel, M. Helgesen, J. E. Carlé, T. T. Larsen-Olsen, S. A. Gevorgyan, J. W. Andreasen, J. Adams, N. Li, F. Machui, G. D. Spyropoulos, T. Ameri, N. Lemaître, M. Legros, A. Scheel, D. Gaiser, K. Kreul, S. Berny, O. R. Lozman, S. Nordman, M. Välimäki, M. Vilkmann, R. R. Søndergaard, M. Jørgensen, C. J. Brabec, F. C. Krebs, *Energy Environ. Sci.* **2014**, 7, 2925.
- [50] W. Q. Liu, S. Y. Liu, N. K. Zawacka, T. R. Andersen, P. Cheng, L. Fu, M. R. Chen, W. F. Fu, E. Bundgaard, M. Jorgensen, X. W. Zhan, F. C. Krebs, H. Z. Chen, *J. Mater. Chem. A* **2014**, 2, 19809.
- [51] L. Mao, Q. Chen, Y. W. Li, Y. Li, J. H. Cai, W. M. Su, S. Bai, Y. Z. Jin, C. Q. Ma, Z. Cui, L. W. Chen, *Nano Energy* **2014**, 10, 259.
- [52] Y. Han, X. Chen, J. Wei, G. Ji, C. Wang, W. Zhao, J. Lai, W. Zha, Z. Li, L. Yan, H. Gu, Q. Luo, Q. Chen, L. Chen, J. Hou, W. Su, C. Q. Ma, *Adv. Sci.* **2019**, 6, 1901490.
- [53] Z. Wang, Y. Han, L. Yan, C. Gong, J. Kang, H. Zhang, X. Sun, L. Zhang, J. Lin, Q. Luo, C. Q. Ma, *Adv. Funct. Mater.* **2021**, 31, 2007276.
- [54] M. S. White, D. C. Olson, S. E. Shaheen, N. Kopidakis, D. S. Ginley, *Appl. Phys. Lett.* **2006**, 89, 143517.
- [55] J. Gilot, I. Barbu, M. M. Wienk, R. A. J. Janssen, *Appl. Phys. Lett.* **2007**, 91, 113520.
- [56] J. B. You, L. T. Dou, K. Yoshimura, T. Kato, K. Ohya, T. Moriarty, K. Emery, C. C. Chen, J. Gao, G. Li, Y. Yang, *Nat. Commun.* **2013**, 4, 1446.
- [57] S. H. Liao, H. J. Jhuo, Y. S. Cheng, S. A. Chen, *Adv. Mater.* **2013**, 25, 4766.
- [58] Y. Liu, J. Zhao, Z. Li, C. Mu, W. Ma, H. Hu, K. Jiang, H. Lin, H. Ade, H. Yan, *Nat. Commun.* **2014**, 5, 5293.
- [59] L. Meng, Y. Zhang, X. Wan, C. Li, X. Zhang, Y. Wang, X. Ke, Z. Xiao, L. Ding, R. Xia, H. L. Yip, Y. Cao, Y. Chen, *Science* **2018**, 361, 1094.
- [60] J. Yuan, Y. Zhang, L. Zhou, G. Zhang, H.-L. Yip, T.-K. Lau, X. Lu, C. Zhu, H. Peng, P. A. Johnson, M. Leclerc, Y. Cao, J. Ulanski, Y. Li, Y. Zou, *Joule* **2019**, 3, 1140.
- [61] X. Song, G. Liu, W. Gao, Y. Di, Y. Yang, F. Li, S. Zhou, J. Zhang, *Small* **2021**, 17, 2006387.
- [62] Y. Wang, Z. Zheng, J. Wang, X. Liu, J. Ren, C. An, S. Zhang, J. Hou, *Adv. Mater.* **2022**, 4, 1645.
- [63] Z. H. Liu, A. L. Zhu, F. S. Cai, L. M. Tao, Y. H. Zhou, Z. X. Zhao, Q. Chen, Y. B. Cheng, H. P. Zhou, *J. Mater. Chem. A* **2017**, 5, 6597.
- [64] K. Hwang, Y. S. Jung, Y. J. Heo, F. H. Scholes, S. E. Watkins, J. Subbiah, D. J. Jones, D. Y. Kim, D. Vak, *Adv. Mater.* **2015**, 27, 1241.
- [65] X. Jia, L. Zhang, Q. Luo, H. Lu, X. Li, Z. Xie, Y. Yang, Y. Q. Li, X. Liu, C. Q. Ma, *ACS Appl. Mater. Interfaces* **2016**, 8, 18410.

- [66] S. Bai, Y. Z. Jin, X. Y. Liang, Z. Z. Ye, Z. W. Wu, B. Q. Sun, Z. F. Ma, Z. Tang, J. P. Wang, U. Wurfel, F. Gao, F. L. Zhang, *Adv. Energy Mater.* **2015**, *5*, 1401606.
- [67] W. Qiu, M. Buffière, G. Brammert, U. W. Paetzold, L. Froyen, P. Heremans, D. Cheyens, *Org. Electron.* **2015**, *26*, 30.
- [68] J. You, L. Meng, T. B. Song, T. F. Guo, Y. M. Yang, W. H. Chang, Z. Hong, H. Chen, H. Zhou, Q. Chen, Y. Liu, N. De Marco, Y. Yang, *Nat. Nanotechnol.* **2016**, *11*, 75.
- [69] D. Y. Son, J. H. Im, H. S. Kim, N. G. Park, *J. Phys. Chem. C* **2014**, *118*, 16567.
- [70] K. Mahmood, B. S. Swain, A. Amassian, *Adv. Energy Mater.* **2015**, *5*, 1500568.
- [71] K. Mahmood, B. S. Swain, A. Amassian, *Nanoscale* **2015**, *7*, 12812.
- [72] J. F. Tang, Z. L. Tseng, L. C. Chen, S. Y. Chu, *Sol. Energy Mater. Sol. Cells* **2016**, *154*, 18.
- [73] Y. F. Gong, J. H. Hou, *J. Am. Soc. Nephrology* **2014**, *25*, 745.
- [74] R. Viswanatha, H. Amenitsch, D. D. Sarma, *J. Am. Chem. Soc.* **2007**, *129*, 4470.
- [75] S. Y. Son, J. M. Yun, Y. J. Noh, S. Lee, H. N. Jo, S. I. Na, H. I. Joh, *Carbon* **2015**, *81*, 546.
- [76] Y.-Z. Zheng, E.-F. Zhao, F.-L. Meng, X.-S. Lai, X.-M. Dong, J.-J. Wu, X. Tao, *J. Mater. Chem. A* **2017**, *5*, 12416.
- [77] A. Kumar, A. K. Goyal, U. Gupta, Tanya, N. Gupta, R. Chaujar, *Mater. Today: Proc.* **2020**, *28*, 361.
- [78] T. Kato, J. L. Wu, Y. Hirai, H. Sugimoto, V. Bermudez, *IEEE J. Photovolt.* **2019**, *9*, 325.
- [79] Y. Gong, Q. Zhu, B. Li, S. Wang, B. Duan, L. Lou, C. Xiang, E. Jedlicka, R. Giridharagopal, *Nat. Energy* **2022**, *7*, 966.
- [80] Y. C. Gu, H. P. Shen, C. Ye, X. Z. Dai, Q. Cui, J. B. Li, F. Hao, X. J. Hao, H. Lin, *Adv. Funct. Mater.* **2018**, *28*, 1703369.
- [81] M. Baid, A. Hashmi, B. Jain, A. K. Singh, M. A. Susan, M. Aleksandrova, *Opt. Quant. Electron.* **2021**, *53*.
- [82] C. Ding, D. Wang, D. Liu, H. Li, Y. Li, S. Hayase, T. Sogabe, T. Masuda, Y. Zhou, Y. Yao, Z. Zou, R. Wang, Q. Shen, *Adv. Energy Mater.* **2022**, *12*, 2201676.
- [83] K. S. Leschkies, T. J. Beatty, M. S. Kang, D. J. Norris, E. S. Aydil, *ACS Nano* **2009**, *3*, 3638.
- [84] K. Han, M. L. Xie, L. P. Zhang, L. P. Yan, J. F. Wei, G. Q. Ji, Q. Luo, J. Lin, Y. Y. Hao, C. Q. Ma, *Sol. Energy Mater. Sol. Cells* **2018**, *185*, 399.
- [85] X. B. Chen, G. Y. Xu, G. Zeng, H. W. Gu, H. Y. Chen, H. T. Xu, H. F. Yao, Y. W. Li, J. H. Hou, Y. F. Li, *Adv. Mater.* **2020**, *32*, 198478.
- [86] Y. Sun, L. Meng, X. Wan, Z. Guo, X. Ke, Z. Sun, K. Zhao, H. Zhang, C. Li, Y. Chen, *Adv. Funct. Mater.* **2021**, *31*, 2010000.
- [87] Y. X. Zhang, J. Fang, W. Li, Y. Shen, J. D. Chen, Y. Q. Li, H. W. Gu, S. Pelivani, M. J. Zhang, Y. F. Li, J. X. Tang, *ACS Nano* **2019**, *13*, 4686.
- [88] J. C. Kang, K. Han, X. Sun, L. P. Zhang, R. Huang, I. Ismail, Z. G. Wang, C. Z. Ding, W. S. Zha, F. S. Li, Q. Luo, Y. J. Li, C.-Q. Ma, *Org. Electron.* **2020**, *82*, 105714.
- [89] Y. Y. Gong, T. Andelman, G. F. Neumark, S. O'Brien, I. L. Kuskovsky, *Nanoscale Res. Lett.* **2007**, *2*, 297.
- [90] V. Ischenko, S. Polarz, D. Grote, V. Stavarache, K. Fink, M. Driess, *Adv. Funct. Mater.* **2005**, *15*, 1945.
- [91] H. B. Zeng, G. T. Duan, Y. Li, S. K. Yang, X. X. Xu, W. P. Cai, *Adv. Funct. Mater.* **2010**, *20*, 561.
- [92] M. A. Reshchikov, H. Morkoc, B. Nemeth, J. Nause, J. Xie, B. Hertog, A. Osinsky, *Phys. B-Condens. Matter* **2007**, *401*, 358.
- [93] K. Yang, J. H. Fu, L. J. Hu, Z. Xiong, M. Li, X. Z. Wei, Z. Y. Xiao, S. R. Lu, K. Sun, *ACS Appl. Mater. Interfaces* **2018**, *10*, 39962.
- [94] J. Kim, G. Kim, Y. Choi, J. Lee, S. H. Park, K. Lee, *J. Appl. Phys.* **2012**, *111*, 114511.
- [95] S. Trost, A. Behrendt, T. Becker, A. Polywka, P. Gorrn, T. Riedl, *Adv. Energy Mater.* **2015**, *5*, 1500277.
- [96] Y. Yan, F. L. Cai, L. Y. Yang, J. H. Li, Y. W. Zhang, F. Qin, C. X. Xiong, Y. H. Zhou, D. G. Lidsey, T. Wang, *Adv. Energy Mater.* **2017**, *27*, 1604044.
- [97] G. Lakhwani, R. F. H. Roijmans, A. J. Kronemeijer, J. Gilot, R. A. J. Janssen, S. C. J. Meskers, *J. Phys. Chem. C* **2010**, *114*, 14804.
- [98] D. Son, T. Kuwabara, K. Takahashi, K. Marumoto, *Appl. Phys. Lett.* **2016**, *109*, 133301.
- [99] T. Kuwabara, K. Yano, T. Yamaguchi, T. Taima, K. Takahashi, D. Son, K. Marumoto, *J. Phys. Chem. C* **2015**, *119*, 5274.
- [100] S. Wilken, J. Parisi, H. Borchert, *J. Phys. Chem. C* **2014**, *118*, 19672.
- [101] Z. H. Lin, C. Y. Jiang, C. X. Zhu, J. Zhang, *ACS Appl. Mater. Interfaces* **2013**, *5*, 713.
- [102] S. Trost, K. Zilberberg, A. Behrendt, A. Polywka, P. Gorrn, P. Reckers, J. Maibach, T. Mayer, T. Riedl, *Adv. Energy Mater.* **2013**, *3*, 1437.
- [103] F. J. Lim, A. Krishnamoorthy, G. W. Ho, *ACS Appl. Mater. Interfaces* **2015**, *7*, 12119.
- [104] M. Thambidurai, J. Y. Kim, H. J. Song, Y. Ko, N. Muthukumarasamy, D. Velauthapillai, V. W. Bergmann, S. A. L. Weber, C. Lee, *J. Mater. Chem. A* **2014**, *2*, 11426.
- [105] J. F. Wei, G. Q. Ji, C. J. Zhang, L. P. Yan, Q. Luo, C. Wang, Q. Chen, J. L. Yang, L. W. Chen, C. Q. Ma, *ACS Nano* **2018**, *12*, 5518.
- [106] Y. Yan, F. L. Cai, L. Y. Yang, J. H. Li, Y. W. Zhang, F. Qin, C. X. Xiong, Y. H. Zhou, D. G. Lidzey, T. Wang, *Adv. Mater.* **2017**, *29*, 1604044.
- [107] Y. L. Wang, L. P. Yan, G. Q. Ji, C. Wang, H. M. Gu, Q. Luo, Q. Chen, L. W. Chen, Y. Z. Yang, C. Q. Ma, X. G. Liu, *ACS Appl. Mater. Interfaces* **2019**, *11*, 2243.
- [108] Y. Jiang, L. Sun, F. Jiang, C. Xie, L. Hu, X. Dong, F. Qin, T. Liu, L. Hu, X. Jiang, Y. Zhou, *Mater. Horiz.* **2019**, *6*, 1438.
- [109] B. Liu, Y. Han, Z. Li, H. Gu, L. Yan, Y. Lin, Q. Luo, S. Yang, C.-Q. Ma, *Sol. RRL* **2021**, *5*, 2000638.
- [110] Y. Han, H. Dong, W. Pan, B. Liu, X. Chen, R. Huang, Z. Li, F. Li, Q. Luo, J. Zhang, Z. Wei, C. Q. Ma, *ACS Appl. Mater. Interfaces* **2021**, *13*, 17869.
- [111] O. O. R. A. Liu, Z. X. Liu, S. X. Wang, J. Huang, H. X. Ju, Q. Chen, J. S. Yu, H. Z. Chen, C. Z. Li, *Adv. Energy Mater.* **2019**, *9*, 1900887.
- [112] X. Xu, J. Y. Xiao, G. C. Zhang, L. Wei, X. C. Jiao, H.-L. Yip, Y. Cao, *Sci. Bull.* **2020**, *65*, 208.
- [113] Y. Dkhissi, S. Meyer, D. H. Chen, H. C. Weerasinghe, L. Spiccia, Y. B. Cheng, R. A. Caruso, *ChemSusChem* **2016**, *9*, 687.
- [114] D. Yang, R. X. Yang, J. Zhang, Z. Yang, S. Z. Liu, C. Li, *Energy Environ. Sci.* **2015**, *8*, 3208.
- [115] P. Zhang, J. Wu, Y. F. Wang, H. Sarvari, D. T. Liu, Z. D. Chen, S. B. Li, *J. Mater. Chem. A* **2017**, *5*, 17368.
- [116] F. Qin, W. Meng, J. Fan, C. Ge, B. Luo, R. Ge, L. Hu, F. Jiang, T. Liu, Y. Jiang, Y. Zhou, *ACS Appl. Mater. Interfaces* **2017**, *9*, 26045.
- [117] F. Yang, D. W. Kang, Y. S. Kim, *RSC Adv.* **2017**, *7*, 19030.
- [118] D. Zheng, G. Wang, W. Huang, B. Wang, W. Ke, J. L. Logsdon, H. Wang, Z. Wang, W. Zhu, J. Yu, M. R. Wasielewski, M. G. Kanatzidis, T. J. Marks, A. Facchetti, *Adv. Funct. Mater.* **2019**, *29*, 1900265.
- [119] K. Schutt, P. K. Nayak, A. J. Ramadan, B. Wenger, Y. H. Lin, H. J. Snaith, *Adv. Fun. Mater.* **2019**, *29*, 1900466.
- [120] Z. Yuan, S. Bai, Z. Yan, J. M. Liu, F. Gao, *Chem. Commun.* **2018**, *54*, 6887.
- [121] Z. F. Ma, Z. Tang, E. G. Wang, M. R. Andersson, O. Inganas, F. L. Zhang, *J. Phys. Chem. C* **2012**, *116*, 24462.
- [122] S. Oh, I. Jang, S. G. Oh, S. S. Im, *Sol. Energy* **2015**, *114*, 32.
- [123] G. Q. Ji, W. C. Zhao, J. F. Wei, L. P. Yan, Y. F. Han, Q. Luo, S. F. Yang, J. H. Hou, C. Q. Ma, *J. Mater. Chem. A* **2019**, *7*, 212.
- [124] L. Nian, Z. H. Chen, S. Herbst, Q. Y. Li, C. Z. Yu, X. F. Jiang, H. L. Dong, F. H. Li, L. L. Liu, F. Wurthner, J. W. Chen, Z. Q. Xie, Y. G. Ma, *Adv. Mater.* **2016**, *28*, 7521.

- [125] S. K. Gupta, A. Sharma, S. Banerjee, R. Gahlot, N. Aggarwal, D. A. Garg, *Sol. Energy Mater. Sol. Cells* **2013**, *116*, 135.
- [126] P. C. Du, X. W. Hu, C. Y. Yi, H. C. Liu, P. Liu, H. L. Zhang, X. Gong, *Adv. Funct. Mater.* **2015**, *25*, 2420.
- [127] Y. M. Chang, C. Y. Leu, *J. Mater. Chem. A* **2013**, *1*, 6446.
- [128] J. L. Braid, U. Koldemir, A. Sellinger, R. T. Collins, T. E. Furtak, D. C. Olson, *ACS Appl. Mater. Interfaces* **2014**, *6*, 19229.
- [129] K. D. Kim, D. C. Lim, J. Hu, J. D. Kwon, M. G. Jeong, H. O. Seo, J. Y. Lee, K. Y. Jang, J. H. Lim, K. H. Lee, Y. Jeong, Y. D. Kim, S. Cho, *ACS Appl. Mater. Interfaces* **2013**, *5*, 8718.
- [130] T. Stubhan, M. Salinas, A. Ebel, F. C. Krebs, A. Hirsch, M. Halik, C. J. Brabec, *Adv. Energy Mater.* **2012**, *2*, 532.
- [131] Y. J. Cheng, C. H. Hsieh, Y. J. He, C. S. Hsu, Y. F. Li, *J. Am. Chem. Soc.* **2010**, *132*, 17381.
- [132] P. Fu, X. Guo, S. Y. Wang, Y. Ye, C. Li, *ACS Appl. Mater. Interfaces* **2017**, *9*, 13390.
- [133] Y. E. Ha, M. Y. Jo, J. Park, Y.-C. Kang, S. I. Yoo, J. H. Kim, *J. Phys. Chem. C* **2013**, *117*, 2646.
- [134] S. R. Cowan, P. Schulz, A. J. Giordano, A. Garcia, B. A. MacLeod, S. R. Marder, A. Kahn, D. S. Ginley, E. L. Ratcliff, D. C. Olson, *Adv. Funct. Mater.* **2014**, *24*, 4671.
- [135] X. Gao, J. Li, J. Baker, Y. Hou, D. Guan, J. Chen, C. Yuan, *Chem. Commun.* **2014**, *50*, 6368.
- [136] J. Cao, B. H. Wu, R. H. Chen, Y. Y. Q. Wu, Y. Hui, B. W. Mao, N. F. Zheng, *Adv. Mater.* **2018**, *30*, 1705596.
- [137] Q. Wang, C. C. Chueh, T. Zhao, J. Q. Cheng, M. Eslamian, W. C. H. Choy, A. K. Y. Jen, *ChemSusChem* **2017**, *10*, 3794.
- [138] X. Y. Zhao, H. P. Shen, Y. Zhang, X. Li, X. C. Zhao, M. Q. Tai, J. F. Li, J. B. Li, X. Li, H. Lin, *ACS Appl. Mater. Interfaces* **2016**, *8*, 7826.
- [139] K. Yao, F. Li, Q. Q. He, X. F. Wang, Y. H. Jiang, H. T. Huang, A. K. Y. Jen, *Nano Energy* **2017**, *40*, 155.
- [140] I. Ismail, J. F. Wei, X. Sun, W. S. Zha, M. Khalil, L. P. Zhang, R. Huang, Z. J. Chen, Y. B. Shen, F. S. Li, Q. Luo, C. Q. Ma, *Sol. RRL* **2020**, *4*, 2000289.
- [141] S. Y. Shao, J. Liu, J. Bergqvist, S. W. Shi, C. Veit, U. Wurfel, Z. Y. Xie, F. L. Zhang, *Adv. Energy Mater.* **2013**, *3*, 349.
- [142] J. Liu, J. Wu, S. Y. Shao, Y. F. Deng, B. Meng, Z. Y. Xie, Y. H. Geng, L. X. Wang, F. L. Zhang, *ACS Appl. Mater. Interfaces* **2014**, *6*, 8237.
- [143] X. Jia, N. Wu, J. Wei, L. Zhang, Q. Luo, Z. Bao, Y.-Q. Li, Y. Yang, X. Liu, C.-Q. Ma, *Org. Electron.* **2016**, *38*, 150.
- [144] L. Nian, W. Q. Zhang, S. P. Wu, L. Q. Qin, L. L. Liu, Z. Q. Xie, H. B. Wu, Y. G. Ma, *ACS Appl. Mater. Interfaces* **2015**, *7*, 25821.
- [145] L. Nian, W. Zhang, N. Zhu, L. Liu, Z. Xie, H. Wu, F. Wurthner, Y. Ma, *J. Am. Chem. Soc.* **2015**, *137*, 6995.
- [146] Z. Q. Xie, W. Frank, *Adv. Energy Mater.* **2017**, *7*, 1602573.
- [147] L. Nian, K. Gao, F. Liu, Y. Y. Kan, X. F. Jiang, L. L. Liu, Z. Q. Xie, X. B. Peng, T. P. Russell, Y. G. Ma, *Adv. Mater.* **2016**, *28*, 8184.
- [148] H. J. Yang, T. Wu, T. Hu, X. T. Hu, L. Chen, Y. W. Chen, *J. Mater. Chem. C* **2016**, *4*, 8738.
- [149] C. K. Wu, K. Sivashanmugan, T. F. Guo, T. C. Wen, *Materials* **2018**, *11*, 1602573.
- [150] T. J. Aldrich, M. Matta, W. Zhu, S. M. Swick, C. L. Stern, G. C. Schatz, A. Facchetti, F. S. Melkonyan, T. J. Marks, *J. Am. Chem. Soc.* **2019**, *141*, 3274.
- [151] F. Qin, W. Wang, L. Sun, X. Jiang, L. Hu, S. Xiong, T. Liu, X. Dong, J. Li, Y. Jiang, J. Hou, K. Fukuda, T. Someya, Y. Zhou, *Nat. Commun.* **2020**, *11*, 4508.
- [152] S. H. Liao, H. J. Jhuo, P. N. Yeh, Y. S. Cheng, Y. L. Li, Y. H. Lee, S. Sharma, S. A. Chen, *Sci. Rep.* **2014**, *4*, 6813.
- [153] X. F. Lin, Y. Z. Yang, L. Nian, H. Su, J. M. Ou, Z. K. Yuan, F. Y. Xie, W. Hong, D. S. Yu, M. Q. Zhang, Y. G. Ma, X. D. Chen, *Nano Energy* **2016**, *26*, 216.
- [154] Z. X. Li, R. Wang, J. J. Xue, X. F. Xing, C. C. Yu, T. Y. Huang, J. M. Chu, K. L. Wang, C. Dong, Z. T. Wei, Y. P. Zhao, Z. K. Wang, Y. Yang, *J. Am. Chem. Soc.* **2019**, *141*, 17610.
- [155] Z. H. Lin, J. J. Chang, C. F. Zhang, J. C. Zhang, J. S. Wu, Y. Hao, *J. Mater. Chem. C* **2016**, *4*, 6169.
- [156] Z. G. Yin, Q. D. Zheng, S. C. Chen, D. D. Cai, Y. L. Ma, *Adv. Energy Mater.* **2016**, *6*, 1501493.
- [157] K. S. Shin, K. H. Lee, H. H. Lee, D. Choi, S. W. Kim, *J. Phys. Chem. C* **2010**, *114*, 15782.
- [158] J. J. Wei, Z. G. Yin, S. C. Chen, Q. D. Zheng, *ACS Appl. Mater. Interfaces* **2017**, *9*, 6186.
- [159] H. Peng, W. P. Xu, F. Zhou, J. Zhang, C. N. Li, *Synth. Met.* **2015**, *205*, 164.
- [160] T. Stubhan, I. Litzov, N. Li, M. Salinas, M. Steidl, G. Sauer, K. Forberich, G. J. Matt, M. Halik, C. J. Brabec, *J. Mater. Chem. A* **2013**, *1*, 6004.
- [161] A. Bauer, J. Hanisch, T. Wahl, E. Ahlswede, *Org. Electron.* **2011**, *12*, 2071.
- [162] A. Aprilia, P. Wulandari, V. Suendo, Herman, R. Hidayat, A. Fujii, M. Ozaki, *Sol. Energy Mater. Sol. Cells* **2013**, *111*, 181.
- [163] X. H. Liu, X. D. Li, Y. R. Li, C. J. Song, L. P. Zhu, W. J. Zhang, H. Q. Wang, J. F. Fang, *Adv. Mater.* **2016**, *28*, 7405.
- [164] H. Kaneko, T. Togashi, T. Naka, M. Ishizaki, K. Kanaizuka, M. Sakamoto, M. Kurihara, *Crystengcomm* **2014**, *16*, 10539.
- [165] X. H. Liu, H. Q. Wang, Y. R. Li, Z. Z. Gui, S. Q. Ming, K. Usman, W. J. Zhang, J. F. Fang, *Adv. Sci.* **2017**, *4*, 1700053.
- [166] L. K. Jagadamma, M. Al-Senani, A. El-Labban, I. Gereige, G. O. N. Ndjawa, J. C. D. Faria, T. Kim, K. Zhao, F. Cruciani, D. H. Anjum, M. A. McLachlan, P. M. Beaujuge, A. Amassian, *Adv. Energy Mater.* **2015**, *5*, 1500204.
- [167] Q. Dong, C. H. Y. Ho, H. Yu, A. Salehi, F. So, *Chem. Mater.* **2019**, *31*, 6833.
- [168] H. Dong, S. Pang, Y. Zhang, D. Chen, W. Zhu, H. Xi, J. Chang, J. Zhang, C. Zhang, Y. Hao, *Nanomaterials* **2018**, *8*, 720.
- [169] G. Liu, Y. Zhong, H. Mao, J. Yang, R. Dai, X. Hu, Z. Xing, W. Sheng, L. Tan, Y. Chen, *Chem. Eng. J.* **2022**, *431*, 134235.
- [170] Z. Lin, J. Chang, C. Zhang, J. Zhang, J. Wu, Y. Hao, *J. Mater. Chem. C* **2016**, *4*, 6169.
- [171] A. Soultati, A. Fakharuddin, E. Polydorou, C. Drivas, A. Kaltzoglou, M. I. Haider, F. Kournoutas, M. Fakis, L. C. Palilis, S. Kennou, D. Davazoglou, P. Falaras, P. Argitis, S. Gardelis, A. Kordatos, A. Chronoes, L. Schmidt-Mende, M. Vasilopoulou, *ACS Appl. Energy Mater.* **2019**, *2*, 1663.
- [172] J. Wang, H. Pan, X. Xu, H. Jin, W. Ma, S. Xiong, Q. Bao, Z. Tang, Z. Ma, *ACS Appl. Mater. Interfaces* **2022**, *14*, 12450.
- [173] M. A. Mahmud, N. K. Elumalai, M. B. Upama, D. Wang, A. M. Soufiani, M. Wright, C. Xu, F. Haque, A. Uddin, *ACS Appl. Mater. Interfaces* **2017**, *9*, 33841.
- [174] R. Azmi, S. Hwang, W. Yin, T.-W. Kim, T. K. Ahn, S.-Y. Jang, *ACS Energy Lett.* **2018**, *3*, 1241.
- [175] P.-Y. Chen, S.-H. Yang, *Opt. Mater. Express* **2016**, *6*, 3651.
- [176] K. Mahmood, A. Khalid, *Mater. Lett.* **2018**, *224*, 78.
- [177] S. S. Shin, W. S. Yang, J. H. Noh, J. H. Suk, N. J. Jeon, J. H. Park, J. S. Kim, W. M. Seong, S. I. Seok, *Nat. Commun.* **2015**, *6*, 7410.
- [178] H. Q. Shi, W. N. Li, L. W. Sun, Y. Liu, H. M. Xiao, S. Y. Fu, *Chem. Commun.* **2011**, *47*, 11921.
- [179] A. Abdolmaleki, S. Mallakpour, S. Borandeh, *Polym. Bull.* **2012**, *69*, 15.
- [180] D. D. Cao, S. Gong, X. G. Shu, D. D. Zhu, S. L. Liang, *Nanoscale Res. Lett.* **2019**, *14*, 210.
- [181] J. Guo, Y. Han, Z. Xu, W. Zha, J. Fang, Q. Luo, L. Liu, C.-Q. Ma, *Flex. Print. Electron.* **2022**, *7*.

- [182] P. D. Li, T. G. Jiu, G. Tang, G. J. Wang, J. Li, X. F. Li, J. F. Fang, *ACS Appl. Mater. Interfaces* **2014**, *6*, 18172.
- [183] C. E. Small, S. Chen, J. Subbiah, C. M. Amb, S. W. Tsang, T. H. Lai, J. R. Reynolds, F. So, *Nat. Photonics* **2012**, *6*, 115.
- [184] F. Verbakel, S. C. J. Meskers, R. A. J. Janssen, *J. Phys. Chem. C* **2007**, *111*, 10150.
- [185] S. Suresh, P. Saravanan, K. Jayamoorthy, S. A. Kumar, S. Karthikeyan, *Mater. Sci. & Eng. C-Mater. Bio. Appl.* **2016**, *64*, 286.
- [186] Y. C. Choi, Y. H. Lee, S. H. Im, J. H. Noh, T. N. Mandal, W. S. Yang, S. I. Seok, *Adv. Energy Mater.* **2014**, *4*, 1301680.
- [187] M. B. Yi, J. R. Ku, J. S. Yoon, J. Kal, W. Lee, S. G. Oh, *J. Phys. Chem. Solids* **2020**, *145*, 109538.
- [188] W. Lee, J. Yeop, J. Heo, Y. J. Yoon, S. Y. Park, J. Jeong, Y. S. Shin, J. W. Kim, N. G. An, D. S. Kim, J. Park, J. Kim, *Sci. Rep.* **2020**, *10*, 18055.
- [189] E. Moghaddam, A. A. Youzbashi, A. Kazemzadeh, M. J. Eshraghi, *J. Lumin.* **2015**, *168*, 158.
- [190] Y. Zhang, F. Fang, C. Wang, L. D. Wang, X. J. Wang, X. Y. Chu, J. H. Li, X. Fang, Z. P. Wei, X. H. Wang, *Polym. Compos.* **2014**, *35*, 1204.
- [191] X. S. Tang, E. S. G. Choo, L. Li, J. Ding, J. M. Xue, *Chem. Mater.* **2010**, *22*, 3383.
- [192] E. Lopez-Mena, S. Jimenez-Sandoval, O. Jimenez-Sandoval, *J. Sol-Gel Sci. Technol* **2015**, *74*, 419.
- [193] J. J. Wei, Z. G. Yin, S.-C. Chen, Q. G. Zheng, *ACS Appl. Mater. Interfaces* **2017**, *9*, 6186.
- [194] B. A. MacLeod, B. J. T. de Villers, P. Schulz, P. F. Ndione, H. Kim, A. J. Giordano, K. Zhu, S. R. Marder, S. Graham, J. J. Berry, A. Kahn, D. C. Olson, *Energy Environ. Sci.* **2015**, *8*, 592.
- [195] I. Burgues-Ceballos, M. Stella, P. Lacharmonie, E. Martinez-Ferrero, *J. Mater. Chem. A* **2014**, *2*, 17711.
- [196] P. Cheng, H. Bai, N. K. Zawacka, T. R. Andersen, W. Liu, E. Bundgaard, M. Jorgensen, H. Chen, F. C. Krebs, X. Zhan, *Adv. Sci.* **2015**, *2*, 1500096.
- [197] W. Liu, S. Liu, N. K. Zawacka, T. R. Andersen, P. Cheng, L. Fu, M. Chen, W. Fu, E. Bundgaard, M. Jørgensen, X. Zhan, F. C. Krebs, H. Chen, *J. Mater. Chem. A* **2014**, *2*, 19809.
- [198] Y. Lin, H. F. Dam, T. R. Andersen, E. Bundgaard, W. Fu, H. Chen, F. C. Krebs, X. Zhan, *J. Mater. Chem. C* **2013**, *1*, 8007.
- [199] J. F. Wei, C. J. Zhang, G. Q. Ji, Y. F. Han, I. Ismail, H. Y. Li, Q. Luo, J. Y. Yang, C.-Q. Ma, *Sol. Energy* **2019**, *193*, 102.
- [200] S. A. Mauger, K. X. Steirer, J. Boe, D. P. Ostrowski, D. C. Olson, S. R. Hammond, *Org. Electron.* **2016**, *31*, 63.
- [201] A. Janotti, C. G. Van de Walle, *Rep. Prog. Phys.* **2009**, *72*, 126501.
- [202] S. K. Hau, H.-L. Yip, N. S. Baek, J. Zou, K. O'Malley, A. K. Y. Jen, *Appl. Phys. Lett.* **2008**, *92*, 253301.
- [203] Y. J. Cheng, C. H. Hsieh, Y. He, C. S. Hsu, Y. Li, *J. Am. Chem. Soc.* **2010**, *132*, 17381.
- [204] C. E. Small, S. Chen, J. Subbiah, C. M. Amb, S.-W. Tsang, T.-H. Lai, J. R. Reynolds, F. So, *Nat. Photonics* **2011**, *6*, 115.
- [205] S. M. Yoon, S. J. Lou, S. Loser, J. Smith, L. X. Chen, A. Facchetti, T. J. Marks, *Nano Lett* **2012**, *12*, 6315.
- [206] S. H. Liao, H. J. Jhuo, Y. S. Cheng, S. A. Chen, *Adv. Mater.* **2013**, *25*, 4766.
- [207] L. Nian, W. Zhang, N. Zhu, L. Liu, Z. Xie, H. Wu, F. Wurthner, Y. Ma, *J. Am. Chem. Soc.* **2015**, *137*, 6995.
- [208] S. Li, L. Ye, W. Zhao, S. Zhang, S. Mukherjee, H. Ade, J. Hou, *Adv. Mater.* **2016**, *28*, 9423.
- [209] W. Zhao, S. Li, H. Yao, S. Zhang, Y. Zhang, B. Yang, J. Hou, *J. Am. Chem. Soc.* **2017**, *139*, 7148.
- [210] J. Gilot, M. M. Wienk, R. A. J. Janssen, *Appl. Phys. Lett.* **2007**, *90*, 143512.
- [211] J. Gilot, M. M. Wienk, R. A. Janssen, *Adv. Mater.* **2010**, *22*, E67.
- [212] C. H. Chou, W. L. Kwan, Z. Hong, L. M. Chen, Y. Yang, *Adv. Mater.* **2011**, *23*, 1282.
- [213] L. Dou, J. You, J. Yang, C.-C. Chen, Y. He, S. Murase, T. Moriarty, K. Emery, G. Li, Y. Yang, *Nat. Photonics* **2012**, *6*, 180.
- [214] J. You, L. Dou, K. Yoshimura, T. Kato, K. Ohya, T. Moriarty, K. Emery, C. C. Chen, J. Gao, G. Li, Y. Yang, *Nat. Commun.* **2013**, *4*, 1446.
- [215] C. C. Chen, W. H. Chang, K. Yoshimura, K. Ohya, J. You, J. Gao, Z. Hong, Y. Yang, *Adv. Mater.* **2014**, *26*, 5670.
- [216] H. Zhou, Y. Zhang, C. K. Mai, S. D. Collins, G. C. Bazan, T. Q. Nguyen, A. J. Heeger, *Adv. Mater.* **2015**, *27*, 1767.
- [217] M. Li, K. Gao, X. Wan, Q. Zhang, B. Kan, R. Xia, F. Liu, X. Yang, H. Feng, W. Ni, Y. Wang, J. Peng, H. Zhang, Z. Liang, H.-L. Yip, X. Peng, Y. Cao, Y. Chen, *Nat. Photonics* **2016**, *11*, 85.
- [218] Y. Cui, H. Yao, B. Gao, Y. Qin, S. Zhang, B. Yang, C. He, B. Xu, J. Hou, *J. Am. Chem. Soc.* **2017**, *139*, 7302.
- [219] S. K. Hau, H.-L. Yip, H. Ma, A. K. Y. Jen, *Appl. Phys. Lett.* **2008**, *93*, 23304.
- [220] S. Chen, C. E. Small, C. M. Amb, J. Subbiah, T.-H. Lai, S.-W. Tsang, J. R. Manders, J. R. Reynolds, F. So, *Adv. Energy Mater.* **2012**, *2*, 1333.
- [221] A. K. Kyaw, D. H. Wang, D. Wynands, J. Zhang, T. Q. Nguyen, G. C. Bazan, A. J. Heeger, *Nano Lett.* **2013**, *13*, 3796.
- [222] J. Subbiah, B. Purushothaman, M. Chen, T. Qin, M. Gao, D. Vak, F. H. Scholes, X. Chen, S. E. Watkins, G. J. Wilson, A. B. Holmes, W. W. Wong, D. J. Jones, *Adv. Mater.* **2015**, *27*, 702.
- [223] J. Liu, X. Li, S. Zhang, X. Ren, J. Cheng, L. Zhu, D. Zhang, L. Huo, J. Hou, W. C. H. Choy, *Adv. Mater. Interfaces* **2015**, *2*, 1500324.
- [224] Q. Fan, Q. Zhu, Z. Xu, W. Su, J. Chen, J. Wu, X. Guo, W. Ma, M. Zhang, Y. Li, *Nano Energy* **2018**, *48*, 413.
- [225] Y. Cui, H. Yao, L. Hong, T. Zhang, Y. Xu, K. Xian, B. Gao, J. Qin, J. Zhang, Z. Wei, J. Hou, *Adv. Mater.* **2019**, *31*, 1808356.
- [226] H. N. Tran, S. Park, F. T. A. Wibowo, N. V. Krishna, J. H. Kang, J. H. Seo, H. Nguyen-Phu, S. Y. Jang, S. Cho, *Adv. Sci.* **2020**, *7*, 2002395.
- [227] Z. Q. Liang, Q. F. Zhang, O. Wiranwetchayan, J. T. Xi, Z. Yang, K. Park, C. D. Li, G. Z. Cao, *Adv. Funct. Mater.* **2012**, *22*, 2194.
- [228] L. Zuo, Z. Gu, T. Ye, W. Fu, G. Wu, H. Li, H. Chen, *J. Am. Chem. Soc.* **2015**, *137*, 2674.
- [229] W. Zhao, D. Qian, S. Zhang, S. Li, O. Inganas, F. Gao, J. Hou, *Adv. Mater.* **2016**, *28*, 4734.
- [230] S. Zhang, Y. Qin, J. Zhu, J. Hou, *Adv. Mater.* **2018**, *30*, e1800868.
- [231] L. J. A. Koster, W. J. van Strien, W. J. E. Beek, P. W. M. Blom, *Adv. Funct. Mater.* **2007**, *17*, 1297.
- [232] G. Liu, R. Xia, Q. Huang, K. Zhang, Z. Hu, T. Jia, X. Liu, H. L. Yip, F. Huang, *Adv. Funct. Mater.* **2021**, *31*, 2103283.
- [233] J. Dong, Y. H. Zhao, J. J. Shi, H. Y. Wei, J. Y. Xiao, X. Xu, J. H. Luo, J. Xu, D. M. Li, Y. H. Luo, Q. B. Meng, *Chem. Commun.* **2014**, *50*, 13381.
- [234] D. Li, W. Y. Lai, Y. Z. Zhang, W. Huang, *Adv. Mater.* **2018**, *30*.
- [235] Y. Z. Zheng, E. F. Zhao, F. L. Meng, X. S. Lai, X. M. Dong, J. J. Wu, X. Tao, *J. Mater. Chem. A* **2017**, *5*, 12416.
- [236] S. S. He, L. B. Qiu, X. Fang, G. Z. Guan, P. N. Chen, Z. T. Zhang, H. S. Peng, *J. Mater. Chem. A* **2015**, *3*, 9406.
- [237] S. H. Tsai, S. T. Ho, H. J. Jhuo, C. R. Ho, S. A. Chen, J.-H. He, *Appl. Phys. Lett.* **2013**, *102*, 253111.
- [238] T. Stubhan, H. Oh, L. Pinna, J. Krantz, I. Litzov, C. J. Brabec, *Org. Electron.* **2011**, *12*, 1539.
- [239] A. Aprilia, P. Wulandari, V. Suendo, Herman, R. Hidayat, A. Fujii, M. Ozaki, *Sol. Energy Mater. Sol. Cells* **2013**, *111*, 181.
- [240] Q. Zhang, R. Peng, C. Zhang, D. Chen, Z. Lin, J. Chang, J. Zhang, Y. Hao, *Polymers* **2018**, *10*, 127.
- [241] L. K. Jagadamma, M. Al-Senani, A. El-Labban, I. Gereige, G. O. N. Ndjawa, J. C. D. Faria, T. Kim, K. Zhao, F. Cruciani, D. H. Anjum, M. A. McLachlan, P. M. Beaujuge, A. Amassian, *Adv. Energy Mater.* **2015**, *5*, 1500204.
- [242] S. Park, R. Kang, S. Cho, *Current Appl. Phys.* **2020**, *20*, 172.

- [243] X. Yu, X. Yu, J. Zhang, D. Zhang, L. Chen, Y. Long, *Sol. Energy* **2017**, 153, 96.
- [244] S. Zhou, J. Zhao, L. Nian, Q. Zhang, P. Wang, D. Zheng, X. Gao, Q. Rong, L. Shui, G. Zhou, N. Li, *Opt. Mater.* **2020**, 109, 110243.
- [245] X. Liu, H. Q. Wang, Y. Li, Z. Gui, S. Ming, K. Usman, W. Zhang, J. Fang, *Adv. Sci.* **2017**, 4, 1700053.
- [246] G. Chen, T. Wang, C. Li, L. Yang, T. Xu, W. Zhu, Y. Gao, B. Wei, *Org. Electron.* **2016**, 36, 50.
- [247] B. A. MacLeod, P. Schulz, S. R. Cowan, A. Garcia, D. S. Ginley, A. Kahn, D. C. Olson, *Adv. Energy Mater.* **2014**, 4, 1400073.
- [248] Z. Yin, Q. Zheng, S.-C. Chen, D. Cai, L. Zhou, J. Zhang, *Adv. Energy Mater.* **2014**, 4, 1301404.
- [249] Z. G. Yin, Q. D. Zheng, S. C. Chen, D. D. Cai, Y. L. Ma, *Adv. Energy Mater.* **2016**, 6, 1501493.
- [250] M. Thambidurai, J. Y. Kim, J. Song, Y. Ko, H.-J. Song, C.-M. Kang, N. Muthukumarasamy, D. Velauthapillai, C. Lee, *J. Mater. Chem. C* **2013**, 1, 8161.
- [251] R. Diana, *Int. J. Electrochem. Sci.* **2019**, <https://doi.org/10.20964/2019.11.1310281>.
- [252] R. Sharma, H. Lee, K. Borse, V. Gupta, A. G. Joshi, S. Yoo, D. Gupta, *Org. Electron.* **2017**, 43, 207.
- [253] J. Wang, C. Yan, X. Zhang, X. Zhao, Y. Fu, B. Zhang, Z. Xie, *J. Mater. Chem. C* **2016**, 4, 10820.
- [254] S. Kwon, K.-G. Lim, M. Shim, H. C. Moon, J. Park, G. Jeon, J. Shin, K. Cho, T.-W. Lee, J. K. Kim, *J. Mater. Chem. A* **2013**, 1, 11802.
- [255] A. Savva, S. A. Choulis, *Appl. Phys. Lett.* **2013**, 102, 233301.
- [256] L. Zuo, S. Zhang, S. Dai, H. Chen, *RSC Adv.* **2015**, 5, 49369.
- [257] X. Song, G. Liu, W. Gao, Y. Di, Y. Yang, F. Li, S. Zhou, J. Zhang, *Small* **2021**, 17, 2006378.
- [258] M. Zafar, B. Kim, D.-H. Kim, *Mater. Chem. Phys.* **2020**, 240, 122076.
- [259] M. Zafar, J.-Y. Yun, D.-H. Kim, *Mater. Sci. Semicond Process* **2019**, 96, 66.
- [260] Z.-Z. Gui, X. Liu, S. Ming, J.-Y. Zhang, Q. Xie, T. Chen, H.-Q. Wang, *Org. Electron.* **2018**, 53, 296.
- [261] J. Li, M. Ren, J. Qing, Y. Wang, Z. Liang, N. Wang, J. Tong, C. Yang, Y. Xia, *Mol. Cryst. Liq. Cryst.* **2020**, 692, 74.
- [262] M. Shirazi, R. Sabet Dariani, M. R. Toroghinejad, *J. Alloys Compd.* **2017**, 692, 492.
- [263] Z. Wang, Y. Xia, L. Chao, Y. Pan, M. Li, R. Li, B. Du, Y. Chen, W. Huang, *J. Energy Chem.* **2019**, 28, 107.
- [264] S. S. Mali, J. V. Patil, C. K. Hong, *Adv. Energy Mater.* **2019**, 10, 1902708.
- [265] J. Song, E. Zheng, L. Liu, X. F. Wang, G. Chen, W. Tian, T. Miyasaka, *ChemSusChem* **2016**, 9, 2640.



**Yunfei Han** received his Ph.D. from Suzhou Institute of Nano-Tech and Nano-Bionics, CAS. Currently, he is a postdoctoral researcher at Suzhou Institute of Nano-Tech and Nano-Bionics. His research interest includes flexible large-area organic photovoltaics.



**Jingbo Guo** is a master's student of Suzhou Institute of Nano-Tech and Nano-Bionics, CAS. His research interest includes solution-processable metal oxides for printed photovoltaics.



**Qun Luo** received her Ph.D. from Zhejiang University in 2011. Then, she worked as a postdoc at Suzhou Institute of Nano-Tech and Nano-Bionics, CAS. Currently, she is a professor at Suzhou Institute of Nano-Tech and Nano-Bionics. Her research interests include inks for printed photovoltaics and interface engineering in flexible/large-area printed solar cells.



**Chang-Qi Ma** received his Ph.D. at the Technical Institute of Physics and Chemistry (CAS) with Professor Bao-Wen Zhang. After that, he worked as a postdoc at Heriot-Watt University (UK) with Dr. Graeme Cooke, and then he joined Peter Bäuerle group at University of Ulm in 2004 as a Humboldt fellow. From January 2007 to May 2011, he did his habilitation at the Institute of Organic Chemistry II and Advanced Materials, Ulm University. In June 2011, he joined Suzhou Institute of Nano-Tech and Nano-Bionics as a professor. His research focuses on the printing processing and stability of OSCs.